

# FINAL REPORT

Effects of Soot Structure on Soot Oxidation Kinetics

SERDP Project WP-1576

JUNE 2011

JoAnn Lighty  
Adel Sarofim  
C.A. Echavarria  
I.C. Jaramillo  
J. Levinthal  
V. Romano  
**Department of Chemical Engineering  
University of Utah**

*This document has been cleared for public release*



This report was prepared under contract to the Department of Defense Strategic Environmental Research and Development Program (SERDP). The publication of this report does not indicate endorsement by the Department of Defense, nor should the contents be construed as reflecting the official policy or position of the Department of Defense. Reference herein to any specific commercial product, process, or service by trade name, trademark, manufacturer, or otherwise, does not necessarily constitute or imply its endorsement, recommendation, or favoring by the Department of Defense.

**REPORT DOCUMENTATION PAGE**

*Form Approved  
OMB No. 0704-0188*

The public reporting burden for this collection of information is estimated to average 1 hour per response, including the time for reviewing instructions, searching existing data sources, gathering and maintaining the data needed, and completing and reviewing the collection of information. Send comments regarding this burden estimate or any other aspect of this collection of information, including suggestions for reducing the burden, to the Department of Defense, Executive Services and Communications Directorate (0704-0188). Respondents should be aware that notwithstanding any other provision of law, no person shall be subject to any penalty for failing to comply with a collection of information if it does not display a currently valid OMB control number.

**PLEASE DO NOT RETURN YOUR FORM TO THE ABOVE ORGANIZATION.**

<b>1. REPORT DATE (DD-MM-YYYY)</b> 16-06-2011	<b>2. REPORT TYPE</b> Final	<b>3. DATES COVERED (From - To)</b> March 2007 - June2011
--	--------------------------------	--

<b>4. TITLE AND SUBTITLE</b> Effects of Soot Structure on Soot Oxidation Kinetics	<b>5a. CONTRACT NUMBER</b> W912HQ-07-C-0021
	<b>5b. GRANT NUMBER</b>
	<b>5c. PROGRAM ELEMENT NUMBER</b>

<b>6. AUTHOR(S)</b> Lighty, J. S.	<b>5d. PROJECT NUMBER</b> WP- 1576
	<b>5e. TASK NUMBER</b>
	<b>5f. WORK UNIT NUMBER</b>

<b>7. PERFORMING ORGANIZATION NAME(S) AND ADDRESS(ES)</b> University of Utah, Dept. of Chemical Engineering 50 South Central Campus Drive Salt Lake City UT 84112	<b>8. PERFORMING ORGANIZATION REPORT NUMBER</b>
--	---

<b>9. SPONSORING/MONITORING AGENCY NAME(S) AND ADDRESS(ES)</b> SERDP 901 North Stuart Street, Suite 303 Arlington, VA 22203	<b>10. SPONSOR/MONITOR'S ACRONYM(S)</b> SERDP
	<b>11. SPONSOR/MONITOR'S REPORT NUMBER(S)</b>

**12. DISTRIBUTION/AVAILABILITY STATEMENT**  
Approved for public release; distribution is unlimited

**13. SUPPLEMENTARY NOTES**

**14. ABSTRACT**  
This project focused on the mechanisms of soot oxidation by O2. A two-stage burner was used. Soot was generated for ethylene, JP-8 surrogate (n-dodecane/m-xylene), m-xylene, and n-dodecane air premixed flames. Downstream, the soot-laden gases were passed through a secondary flat-flame burner where soot was burned out under fuel-lean or -rich conditions. The process was followed by the evolution of particle size distribution, flame temperature, gas-phase composition, soot morphology and nanostructure. Measurements of soot size distribution and number concentration as a function of the HAB showed particle fragmentation, evidenced by the decrease in particle mean diameter and a significant increase in number concentration in the region where O2 concentration decreased. Higher in the burner, soot was burned as a result of the increase in OH\* concentration which produced higher soot oxidation rates. Experimental information from PSDs, temperature, gas-phase composition was used to develop an oxidation kinetic expression that accounts for the effects of temperature, O2, and OH\* on the rate of oxidation.

**15. SUBJECT TERMS**  
soot oxidation, particle size distribution

<b>16. SECURITY CLASSIFICATION OF:</b>			<b>17. LIMITATION OF ABSTRACT</b> UU	<b>18. NUMBER OF PAGES</b> 77	<b>19a. NAME OF RESPONSIBLE PERSON</b> JoAnn S. Lighty
<b>a. REPORT</b> UU	<b>b. ABSTRACT</b> UU	<b>c. THIS PAGE</b> UU			<b>19b. TELEPHONE NUMBER (Include area code)</b> (801) 581-5763

Reset



## Table of Contents

<b>ABSTRACT</b> .....	<b>1</b>
<b>OBJECTIVES</b> .....	<b>2</b>
SERDP Relevance.....	2
Technical Objectives.....	2
<b>BACKGROUND</b> .....	<b>3</b>
<b>MATERIALS and METHODS</b> .....	<b>9</b>
Burner System.....	9
Flame Temperature Measurements.....	12
Particle Size and Concentration .....	14
Dilution During the Sampling of Nanoparticles from Flames .....	15
Dilution Ratio Calculation .....	16
Corrections to PSDs .....	18
Chemical Analysis.....	21
Soot Surface Area Measurements .....	22
Soot Morphology and Nanostructure .....	25
HR-TEM Image Processing .....	27
Methodology to predict OH* & gas-phase species (H <sub>2</sub> , O <sub>2</sub> , CO, CO <sub>2</sub> ) .....	36
Methodology to Obtain Soot oxidation Rates from Experimental Data.....	36
<b>RESULTS AND DISCUSSION</b> .....	<b>37</b>
Ethylene/air Flames.....	37
Surrogate/Air, m-Xylene/Air and n-Dodecane/Air Flames .....	47
Development of kinetics for soot oxidation and comparisons .....	54
Comprehensive Soot Oxidation Expression.....	56
Changes in Soot Morphology and Nanostructure During Soot Oxidation.....	57
Feasibility of Soot Fragmentation due to Internal Burning.....	64
<b>CONCLUSIONS AND IMPLICATIONS</b> .....	<b>70</b>
<b>LITERATURE CITED</b> .....	<b>73</b>
<b>LIST OF PUBLICATIONS AND PRESENTATIONS</b> .....	<b>76</b>

## List of Tables

Table 1. OH* collision efficiencies for various studies.....	4
Table 2. Empirical parameters for Nagle and Strickland-Constable Model, $k = Ae^{-E/RT}$ .....	5
Table 3. Studies used to generate rates in Figure 4.....	8
Table 4. Summary of Experimental Conditions .....	10
Table 5. Kinetic parameters that produced best fitting for the experimental data.....	56
Table 6. Summary of samples collected .....	61
Table 7. Effectiveness factor calculation for the ethylene/air system with $\Phi_{\text{overall}} = 0.8$ .....	68
Table 8. Effectiveness factor calculation for the surrogate mixture/air system with $\Phi_{\text{overall}} = 0.8$ .....	68

## List of Figures

Figure 1. Distribution of activation energies for oxygen adsorbed on soot determined by temperature programmed desorption (Du et al., 1990). .....	6
Figure 2. Illustration of how the ordering of carbons varies with combustion conditions, in this case increasing with carbon conversion (Kandas, 1997).....	7
Figure 3. Internal surface areas of two soots (ST1 ethylene soot, ST2 ethylene soot with 2% Ca catalyst) as a function of fractional oxidation. ....	7
Figure 4. Selected rates of oxidation of carbon by O <sub>2</sub> reported in the literature. ....	8
Figure 5. Two-Stage Burner .....	10
Figure 6. Schematic representation of the bottom burner showing injection system for liquid fuels.....	11
Figure 7. Chromatograms of the surrogate mixture before vaporization and after vaporization-condensation.....	12
Figure 8. Fast response thermocouple setup. ....	12
Figure 9. Transient response of the thermocouple under: (a) Nonsooting conditions and (b) Sooting conditions. ....	13
Figure 10. SMPS and dilution sampling system indicating probe ID, OD and line lengths. ....	15
Figure 11. Flow Schematic for the Electrostatic Classifier (TSI Inc.).....	15
Figure 12. Schematic representation of the eductor.....	17
Figure 13. Dilution ratio calibration (a) Q <sub>p</sub> as a function of $\Delta P_3$ and (b) DR as a function of Q <sub>p</sub> . ....	18
Figure 14. Penetration efficiencies thorough the turbulent side ( $\eta_T$ ), laminar side ( $\eta_{\text{line}}$ ), sampling orifice ( $\eta_p$ ), SMPS( $\eta_{\text{SMPS}}$ ) and overall sampling efficiency ( $\eta$ ).....	21
Figure 15. Sampling system to measure gas-phase compounds. ....	21
Figure 16. CO <sub>2</sub> adsorption test on commercial coal powder (CA Corp.) at 297 K. ....	23
Figure 17. CO <sub>2</sub> adsorption test carried out on an empty sample holder. Weight changes were due to drag and buoyancy effects. ....	23
Figure 18. CO <sub>2</sub> adsorption capacity as a function of the CO <sub>2</sub> partial pressure on coal powder (CA corp.), and soot samples collected in the two-stage burner under a $\Phi_{\text{overall}} = 0.8$ at 0 and 2.5 mm. ....	24

Figure 19. Dubinin- Polanyi plots showing the experimental data plotted according to Equation (18), and the linear regressions to obtain the monolayer adsorption capacity ( $x_s$ ) for the three sample run. ....	25
Figure 20. Thermophoretic sampling system for transmission electron microscopy analysis. ....	26
Figure 21. The relative error of Equation (31).....	30
Figure 22. The main steps of the new algorithm for the determination of distance deviation parameter. Left: frequency filtered image. Center: binarized image (BW) with the thinned network indicated by blue lines (N). Right: the distance transform of N, $\Delta$ and the extracted distances indicated by blue lines (E). ....	32
Figure 23. Examples of artificially created binary fringe images. Top left: oriented, axially symmetric set. $S_{2;N} \sim 0:99$ . Top right: a shued version of the oriented axial set. $S_{2;N} \sim 0:6$ . Bottom left: oriented, concentrically symmetric set. $S_{2;N} \sim 0:99$ . Bottom right: a shued version of the oriented polar set. $S_{2;P} \sim 0:6$ .....	32
Figure 24. The results of the stochastic simulations. Top: the correlation of $\Omega$ with $S_{2;p}$ . Bottom: the correlation of $\Omega$ with $S_{2;p}$ . ....	34
Figure 25. The calibration of the junction-finding algorithm. Left: a detail of a HR-TEM micrograph taken of an oriented Si single crystal. Right: The detected network (red lines) and branchpoints (green dots). ....	35
Figure 26. The verification of the junction-finding algorithm with Si 110 lattice images .....	36
Figure 27. Schematic representation of the methodology used to predict the evolution of soot oxidizer species.....	37
Figure 28. Top burner temperature profiles as a function of HAB for $\Phi_{\text{overall}} = 0.8$ and 1.14. Thermocouple uncertainty $\pm 50\text{K}$ .....	38
Figure 29. Experimental PSDs measured as a function of the height above the top burner for $\Phi_{\text{overall}} = 0.8$ (left) and $\Phi_{\text{overall}} = 1.14$ (right).....	39
Figure 31. Experimental measurements versus model predictions of $\text{H}_2$ ( $\square$ data, — model), $\text{O}_2$ ( $\Delta$ data, - - - model), $\text{CO}$ ( $\circ$ data, - - - model), $\text{CO}_2$ (x data, ---- model) and $\text{OH}^*$ (.- — model) for (a) $\Phi_{\text{overall}} = 0.8$ and (b) $\Phi_{\text{overall}} = 1.14$ .....	41
Figure 32. Experimental soot oxidation rates (W) calculated from the evolution of PSD for $\Phi_{\text{overall}} = 0.8$ and 1.14.....	42
Figure 33. Top burner temperature profiles as a function of HAB for $\Phi_{\text{overall}} = 0.87, 0.94$ and 1.07. Thermocouple uncertainty $\pm 50\text{K}$ .....	43
Figure 34. Experimental PSDs measured as a function of the height above the top burner for (a) $\Phi_{\text{overall}} = 0.87$ , (b) $\Phi_{\text{overall}} = 0.94$ and (c) $\Phi_{\text{overall}} = 1.07$ .....	44
Figure 35. Integrated number and mass concentrations for fuel lean and fuel rich flames: (a) and (b) number and mass concentration for the ultrafine and fine modes ( $\Phi_{\text{overall}} = 0.87$ ); (c) and (d) number and mass concentration for the ultrafine and fine modes ( $\Phi_{\text{overall}} = 0.94$ ); (e) and (f) number and mass concentration for the ultrafine and fine modes ( $\Phi_{\text{overall}} = 1.07$ ). ....	45
Figure 36. Experimental measurements (open symbols) versus model predictions of $\text{H}_2$ ( $\square$ , data, — model), $\text{O}_2$ ( $\Delta$ data, - - - model), $\text{CO}$ ( $\circ$ data, - - - model), $\text{CO}_2$ (X data, ---- model) and $\text{OH}^*$ (.- — model) for (a) $\Phi_{\text{overall}} = 0.87$ , (b) $\Phi_{\text{overall}} = 0.94$ and (c) $\Phi_{\text{overall}} = 1.07$ . Error bars represent the experimental uncertainty. ....	46
Figure 37. Experimental soot oxidation rates (W) calculated from the evolution of PSD as a function of the HAB for $\Phi_{\text{overall}} = 0.87, 0.94$ and 1.07. ....	47

Figure 38. Top burner temperature profiles as a function of HAB under lean and rich conditions. Soot in the top burner was derived from: (a) m-xylene/air flame, (b) surrogate and (c) n-dodecane/air flames. Error bars represent thermocouple uncertainty ( $\pm 50K$ ) .....	48
Figure 39. Evolution of PSD in the top burner in the surrogate/air flame for (a) $\Phi_{\text{overall}} = 0.8$ and HAB from 0 to 3.5 mm, (b) $\Phi_{\text{overall}} = 0.8$ and HAB from 4 to 7 mm, (c) $\Phi_{\text{overall}} = 1.14$ and HAB from 0 to 4 mm and (d) $\Phi_{\text{overall}} = 1.14$ and HAB from 5 to 7 mm .....	49
Figure 40. Evolution of PSD in the top burner in the systems m-xylene/H <sub>2</sub> /air and n-dodecane/H <sub>2</sub> /air for (a) m-x/H <sub>2</sub> /air, $\Phi_{\text{overall}} = 0.8$ and HAB from 0 to 3 mm, (b) m-x/H <sub>2</sub> /air, $\Phi_{\text{overall}} = 0.8$ and HAB from 4 to 5.5 mm, (c) m-x/H <sub>2</sub> /air, $\Phi_{\text{overall}} = 1.14$ and HAB from 0 to 3 mm, (d) m-x/H <sub>2</sub> /air, $\Phi_{\text{overall}} = 1.14$ and HAB from 3.5 to 6 mm, (e) n-d/H <sub>2</sub> /air, $\Phi_{\text{overall}} = 0.8$ and HAB from 0 to 3 mm, (f) n-d/H <sub>2</sub> /air, $\Phi_{\text{overall}} = 0.8$ and HAB from 3.5 to 6 mm, (g) n-d/H <sub>2</sub> /air, $\Phi_{\text{overall}} = 1.14$ and HAB from 0 to 3 mm, (h) n-d/H <sub>2</sub> /air, $\Phi_{\text{overall}} = 1.14$ and HAB from 4 to 7 mm. ....	50
Figure 41. Number concentration measurements in the ultrafine (3-10nm) and fine (>10nm) modes calculated from the PSD for m-xylene, surrogate, and n-dodecane flames under fuel lean and fuel rich condition. (a) $\Phi_{\text{overall}} = 0.8$ , ultrafine mode, (b) $\Phi_{\text{overall}} = 1.14$ , ultrafine mode, (c) $\Phi_{\text{overall}} = 0.8$ , fine mode and (d) $\Phi_{\text{overall}} = 1.14$ , fine mode. * $\Phi_{\text{overall}}$ under fuel lean conditions for the system with m-xylene/H <sub>2</sub> /air is equal to 0.87.....	51
Figure 42. Evolution of major gas phase species for the surrogate mixture and the surrogate components within the second burner. Symbols correspond to experimental results and solid and dashed lines to model predictions (a) H <sub>2</sub> , O <sub>2</sub> , CO and CO <sub>2</sub> for surrogate, (b) H <sub>2</sub> , O <sub>2</sub> , CO and CO <sub>2</sub> for surrogate, (c) OH* predictions, surrogate, $\Phi_{\text{overall}} = 0.8$ and 1.14; (d) H <sub>2</sub> , O <sub>2</sub> , CO and CO <sub>2</sub> for m-xylene, (e) H <sub>2</sub> , O <sub>2</sub> , CO and CO <sub>2</sub> for m-xylene, (f) OH* predictions, m-xylene, $\Phi_{\text{overall}} = 0.87$ and 1.14; (g) H <sub>2</sub> , O <sub>2</sub> , CO and CO <sub>2</sub> for n-dodecane, (h) H <sub>2</sub> , O <sub>2</sub> , CO and CO <sub>2</sub> for n-dodecane, (i) OH* predictions, n-dodecane, $\Phi_{\text{overall}} = 0.8$ and 1.14. Error bars represent experimental uncertainty .....	53
Figure 43. Experimental soot oxidation rates (W) calculated from the evolution of PSD as a function of the HAB under lean and rich conditions.....	54
Figure 44. Experimental versus model prediction using NSC and Neoh's kinetic oxidation equation for the set of flames under lean and slightly rich conditions. (a) and (b) ethylene/air; (c) and (d) surrogate; (e) and (f) m-xylene/air and (g) and (h) n-dodecane/air.....	55
Figure 45. Predictions of soot oxidation rates using Equation 24 for: (a) ethylene/air; $\Phi_{\text{overall}} = 0.8$ (b) and (c) surrogate/air, $\Phi_{\text{overall}} = 0.8, 1.14$ ; (d) and (e) m-xylene/air, $\Phi_{\text{overall}} = 0.87, 1.14$ and (f) and (g) n-dodecane/air, $\Phi_{\text{overall}} = 0.8, 1.14$ .....	58
Figure 46. TEM pictures for ethylene/air flame with $\Phi_{\text{overall}} = 0.87$ . (a) At HAB = 2 mm and (b) At HAB = 4 mm.....	59
Figure 47. TEM pictures for ethylene/air (left) and surrogate (right) at HAB = 0.5 mm, 2 mm and 4 mm.....	60

Figure 48. Some examples of the analyzed images. A, Ethylene flame 1, HAB=0.5 mm. B, Ethylene flame 1, HAB=4 mm. C, Surrogate flame, HAB=1 mm. D, Surrogate flame, HAB=5 mm. E, Benzene flame, HAB=5 mm. F, Benzene flame, HAB=15 mm. ....	62
Figure 49. Results of a conventional statistical image analysis method applied to our samples. Some HAB values were shifted to improve visibility. For exact values see Table 6. ....	63
Figure 50. The measured values of $\Omega$ and $\upsilon$ for the fuel samples. Lines are guides to the eye. ....	64
Figure 51. Hypothesis regarding the role of fragmentation during soot oxidation at low soot burnout (left) and higher soot burnout (right). ....	66
Figure 52. Change of the diameter in the necks or bridges cementing primary particles with HAB. Analysis was performed for 20 pictures for each height .....	70

## List of Acronyms

BET:	Brunauer-Emmett-Teller
DMA:	Differential Mobility Analyzer
DP	Dubinnin-Polay method
HAB:	Height above the top burner
HP:	High pass
HR-TEM:	High-resolution Transmission Electron Microscopy
LP:	Low pass
NSC:	Nagle-Strickland-Constable
PM:	Particulate matter
PSD:	Particle Size Distribution
SMPS:	Scanning Mobility Particle Sizer
STP:	Standard temperature and pressure
TEM:	Transmission Electron Microscopy
TGA:	Thermogravimetric Analyzer
UCPC:	Ultrafine Condensation Particle Counter

**Keywords:** soot oxidation, SMPS, kinetics, fragmentation, PSD, O<sub>2</sub>, OH\*.

**Acknowledgements:** In addition to our funding agency, SERDP, the investigators thank Carlos Andres Echavarria, Isabel Cristina Jaramillo, Vincenzo Romano, Benjamin Brewster and Tierra Shardey for their assistance. Dana Overacker was also instrumental in his assistance in the laboratory. Dr. Arpad Palotas and Pál Tóth for the development of the methodology to process and analyze HR-TEM images. Dr. Randy Vander Wal for his contribution of HR-TEM through the Department of Energy Basic Energy Sciences program.

## ABSTRACT

Soot emissions from gas-turbine engines are a concern for the military for a variety of reasons including environmental and human health. A better understanding of the process of soot formation and oxidation can lead to different strategies to mitigate the release of soot into the atmosphere. Studies have concentrated on soot formation; however, the oxidation process has not been as well characterized, particularly the reactions that involve the presence of  $O_2$  which apply to gas-turbine engines which are normally operated under excess  $O_2$  concentration. Soot oxidizes by reactions with molecular oxygen ( $O_2$ ), oxygen radicals ( $O^*$ ), and hydroxyl radicals ( $OH^*$ ). The reactions of  $O^*$  and  $OH^*$  with soot are relatively well understood, but the reactions of soot with  $O_2$  are not as well understood. Therefore, this project focused on the mechanisms of soot oxidation by  $O_2$  for jet fuels used in military engines.

To separate the soot oxidation mechanisms from the formation steps, a two-stage burner was used. The two-stage system consists of an initial premixed burner where soot was generated under a variety of conditions for ethylene/air, JP-8 surrogate (n-dodecane/m-xylene)/air, m-xylene/air, and n-dodecane/air premixed flames. Downstream, the soot-laden combustion gases were passed through a secondary flat-flame burner where soot was burned out under fuel lean or slightly fuel rich conditions. The process of soot oxidation in the secondary burner was followed by the evolution of particle size distribution (PSD), flame temperature, gas-phase composition, soot surface area, and soot morphology and nanostructure as a function of the height above the second burner (HAB). Measurements of soot size distribution and number concentration as a function of the HAB under fuel lean ( $\Phi_{\text{overall}} = 0.8$ ) and slightly rich ( $\Phi_{\text{overall}} = 1.14$ ) conditions showed particle fragmentation, evidenced by the decrease in particle mean diameter and a significant increase in number concentration in the region where  $O_2$  concentration decreased. Higher in the burner, soot was burned as a result of the increase in  $OH^*$  concentration which produced higher soot oxidation rates. Analysis of the results, in terms of the changes in soot surface area, soot morphology and nanostructure and the effectiveness factor suggested soot fragmentation at a low burnout percentage with internal burning, which in turn, caused both, the breakup of the bridges cementing primary particles and the rupture of the primary particles.

Experimental information from PSDs, temperature, gas-phase composition was used to develop an oxidation kinetic expression that accounts for the effects of temperature,  $O_2$ , and  $OH^*$  on the rate of oxidation of soots of different structure. The kinetic expression was able to reproduce the major features of the experimental results relative to the other predictions using current models proposed in the literature. Examination of this additional aspect of oxidation kinetics via  $O_2$  will enhance fundamental combustion science and over the long term will enable military gas-turbine engines to continue to meet their performance and operating requirements with reduced PM emissions.

## OBJECTIVES

### SERDP Relevance

This project responded to SERDP's Statement of Need (SON) WPSON-07-01, *Combustion Science to Reduce PM Emissions for Military Platforms*. The objective of this SON was "to advance the fundamental combustion science relevant to non volatile particulate matter (PM) formation in military gas turbine engines." The SON stated that modeling and experimental studies which advance the capability to predict PM formation are of interest. Soot is one of the major components of PM from any combustion system. The formation of soot in a gas-turbine (or other) engine is a complex process, involving soot inception, typically from acetylene or aromatic hydrocarbons such as benzene; soot growth; and, finally soot oxidation. The project focused on the mechanisms of soot oxidation by oxygen for jet fuels used in military engines. The reactions with oxygen are particularly important for gas turbines, which operate at high excess-air rates. The examination of the role of fuel components and internal surface on soot oxidation rates was emphasized in the proposed study since the allowance for these effects on the oxidation rate are not currently well characterized. Examination of this additional aspect of oxidation kinetics enhanced fundamental combustion science and over the long term will enable military gas-turbine engines to continue to meet their performance and operating requirements with reduced PM emissions.

### Technical Objectives

Gas-turbine engines are potentially a significant source of PM for the military, and PM emissions are undergoing increasing scrutiny for their health and regulatory impacts. Soot oxidizes by reactions with molecular oxygen ( $O_2$ ), oxygen radicals ( $O^*$ ), and hydroxyl radicals ( $OH^*$ ). The reactions of  $O^*$  and  $OH^*$  with soot are relatively well understood, but the reactions of soot with  $O_2$  are not as well studied, particularly under the conditions applicable to gas-turbine engines. The proposed project focused on the mechanisms of soot oxidation by  $O_2$  for jet fuels used in military engines.

One method of controlling soot emissions is the enhancement of soot oxidation. The technical innovation of this proposal was its focus on the rate of soot oxidation by  $O_2$ . The investigators hypothesize that soot/ $O_2$  oxidation kinetics are critical to the understanding of soot oxidation in a gas-turbine engine. With the high excess air and the short residence times in gas-turbine engines, the soots may have different reactivities than the soots that are formed in flames with higher residence times.

This project had three objectives:

- To determine the effect of the structure of soot, as influenced by the fuel composition on the rate of soot oxidation by  $O_2$ .
- To quantify the role of internal surface area on the soot reactivity;
- To develop power-law kinetic correlations for soot/ $O_2$  oxidation as a function of temperature,  $O_2$ , and time for soots of different structures and porosity.

## BACKGROUND

PM emissions from aircraft comprise between 2-8% of non-road mobile source emissions in the United States, with military aircraft emissions responsible for 13% of those emissions (EPA 1991, 1997, 2006; Blevins 2003). However, aircraft emissions can be one of the major emission sources on a military base (Radian, 1998). Typically, PM from aircraft is smaller than 0.1  $\mu\text{m}$  in diameter (Champagne, 1971; Hagen et al., 1998; Petzold and Schröder, 1998; Pueschel et al., 1998; Rogers et al. 2005). Small particles, such as those found in aircraft exhaust, are thought to deposit more efficiently in the lungs than larger particles and are potentially more damaging (Lighty et al., 2000). Further, studies have linked PM with an aerodynamic diameter of 2.5  $\mu\text{m}$  or less ( $\text{PM}_{2.5}$ ) to adverse health effects (Dockery et al. 1993; Peters et al. 2001; Tolbert et al. 2000). Furthermore, soot can be one of the major constituents of aircraft emissions (Rogers et al. 2005), and the soot content of PM has been linked to dysrhythmia (Tolbert et al. 2000). In addition to health effects, aircraft PM emissions are a concern for climate forcing and cloud formation (Luther et al. 1979; Penner et al. 1999).

Soot emission is the balance of soot formation and oxidation. There are extensive ongoing studies on the difficult problem of soot formation. The proposed project focused on the important complementary process of soot oxidation for jet fuels used in military engines. In particular, the effect of soot structure, both the ordering of the carbon in the soot as influenced by thermal annealing and the internal surface area, on the rate of soot oxidation was studied. The reported soot oxidation rates by  $\text{O}_2$  vary by orders of magnitude, probably because these variables differed between the various studies. It is well known (e.g. Shim and Hurt [2000]) that reactivity decreases with the ordering of carbons and increases with increased internal surface area; however, there have been no systematic studies of these effects under the temperatures and times of interest to soot oxidation in gas turbine engines.

Studies have shown that soot oxidizes by reactions with molecular oxygen ( $\text{O}_2$ ), oxygen radical ( $\text{O}^*$ ), and hydroxyl radical ( $\text{OH}^*$ ). Fenimore and Jones (1967) investigated the rate of soot oxidation under low oxygen-gas partial pressures and temperatures from 1530 to 1890K and were the first to report the importance of  $\text{OH}^*$  as a major oxidation reactant. Their observations suggested that about 10% of the soot- $\text{OH}^*$  collisions resulted in carbon removal. Neoh et al. (1981) also demonstrated that  $\text{OH}^*$  was the dominant oxidant in near stoichiometric and rich conditions. The rate of  $\text{OH}^*$  oxidation was described by a collision efficiency  $\Gamma_{\text{OH}}$ , representing the fraction of collisions of  $\text{OH}^*$  with soot particles that resulted in the removal of a carbon atom, times the collision frequency, i.e.

$$W = 1.29 \times 10^{13} \Gamma_{\text{OH}} P_{\text{OH}} \sqrt{T} \quad (1)$$

where  $W$  is the rate in  $\text{kg/m}^2\cdot\text{s}$ , and  $P$  is partial pressure in atmospheres. Neoh found the collision efficiency to be 0.13 and relatively independent of equivalence ratio and height within the flame. The literature suggests that  $\text{OH}^*$  oxidation is the predominant reaction mechanism, particularly under fuel-rich conditions. In addition, some oxidation occurs via collisions with  $\text{O}^*$ . For example, Vierbaum and Roth (2003) found a collision efficiency of 10% for  $\text{O}^*$ . Table 1

show a collection of collision efficiencies for various investigators and illustrates that the collision efficiency is relatively constant under various conditions.

Table 1. OH\* collision efficiencies for various studies.

Investigators	Experimental Conditions	OH* Collision Efficiency
Bradley et al. 1984	Premixed flat flame, graphite carbon	0.28
Dai et al. 1997	Laminar diffusion flames	0.14
El-Leathy et al. 2002	Unsaturated-hydrocarbon/air laminar diffusion flames	0.10
El-Leathy et al. 2004	Acetylene/argon-fueled high-temperature laminar diffusion flames	0.13
Faeth et al. 2003	Acetylene diffusion flames at sub-atmospheric and atmospheric pressures	0.10
Fenimore and Jones 1967	Two-stage burner	0.10
Garo et al. 1990	Methane laminar diffusion flame	0.10
Kim et al. 2004	Acetylene laminar diffusion flames at pressures of 0.1-1.0 atm	0.13
Neoh 1981	Two-stage burner	0.13
Page 1978	Two-stage burner	0.25
Puri et al. 1994	Methane/butane flame	0.14
Roth et al. 1990	Diaphragm-type shock tube	0.13-0.31
Xu et al. 2003	Hydrocarbon/air diffusion flames at atmospheric pressure	0.14

The rate of soot reaction with O<sub>2</sub> is not well quantified. Therefore, the focus of this work on oxidation by O<sub>2</sub> was justified because the rates of oxidation by OH\* and O are relatively well understood and because the ratio of O<sub>2</sub>/(OH\* + O\*) is high under the very fuel lean conditions found in the burnout zone of gas turbines. The reaction rate of pyrolytic graphite with O<sub>2</sub> developed by Nagle-Strickland-Constable (NSC) (1962), with parameters fitted to data obtained over a temperature range of 1273 to 2273K, is widely used for soot oxidation by O<sub>2</sub>. The NSC relation was developed on the assumption that the rate of reaction of the graphite that they studied was governed by reactions of oxygen with two sites: a low reactivity site A, covering a fraction, x, of the surface, has a rate governed by a Langmuir-Hinshelwood expression, and a high reactivity site B that covers the remaining fraction (1-x) of the surface. Sites B are

converted to sites A in an activated reaction that is weak function of oxygen concentration. The expression developed by this model is:

$$\frac{W}{12} = x \left( \frac{k_A P_{O_2}}{1 + k_Z P_{O_2}} \right) + (1 - x) k_B P_{O_2} \quad (2)$$

where the first term is the contribution to the oxidation rate of the A sites and the second term that of the B sites. The fraction x of the A sites are given by:

$$x = \left[ 1 + \frac{k_T}{k_B P_{O_2}} \right]^{-1} \quad (3)$$

The parameters were fitted to the experimental data by NSC. These are given in Table 2 to show the relatively high pre-exponential constant and activation energy for site A, which leads to its becoming the dominant rate at high temperatures, and the high activation energy for the transformation of sites B to A that might be expected for intramolecular rearrangements.

Table 2. Empirical parameters for Nagle and Strickland-Constable Model,  $k = Ae^{-E/RT}$ .

Rate Constant	E, kcal/mole	A	Units for A
$k_A$	30	20	$\text{g-atom cm}^{-2}\text{sec}^{-1}\text{atm}^{-1}$
$k_B$	15.2	$4.46 \times 10^{-3}$	$\text{g-atom cm}^{-2}\text{sec}^{-1}\text{atm}^{-1}$
$k_T$	97	$1.51 \times 10^{-5}$	$\text{g-atom cm}^{-2}\text{sec}^{-1}$
$k_Z$	21.3	21.3	$\text{atm}^{-1}$

Although the NSC relationship has been widely used for soot oxidation, it represents a limiting low rate since it applies to nonporous graphitized carbons. Graphitic materials have two types of sites, the reactive edge carbons and the less reactive basal planes. Although NSC is an empirical equation, it is consistent with such a physical model with sites ‘B’ corresponding to the edge sites and sites ‘A’ to the basal plane. It is also known that graphites can be ordered by thermal annealing, which would correspond to the transformation of B to A sites.

Soots have a wide range of structures depending upon their temperature histories. For example, Du et al. (1990) have shown the distribution of the sites through the use of temperature-programmed desorption. The results shown in Figure 1 indicate that the soot desorption has a continuous distribution of energies, rather than a bimodal distribution. Hurt and Haynes (2005) have shown that such a distribution of activation energies is common to many carbons and that they lead correlations for oxidation that show a dominant activation energy and a power law dependence on oxygen.

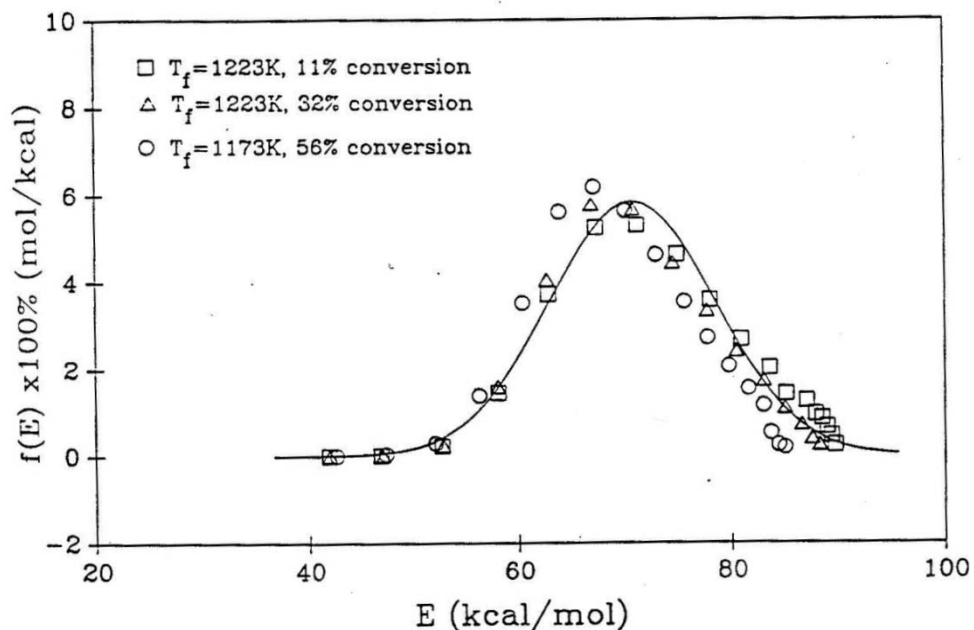


Figure 1. Distribution of activation energies for oxygen adsorbed on soot determined by temperature programmed desorption (Du et al., 1990).

The structures of carbon vary from completely amorphous to complete ordering in planes in graphite; the rate expressions for oxidation will vary with the extent of ordering, with the more disordered structures having higher rate coefficients. The ordering of carbon increases with heat treatment and also with extent of reaction. The ordering can be determined by use of high-resolution transmission electron microscopy (HR-TEM) and image analysis as shown in Figure 2. The figure shows how the ordering of a synthetic char (Spherocharb) increases with extent of burnout.

Another complicating factor is that soots burn internally and develop high surface areas, as shown in Figure 3, which shows a near tenfold increase in soot Brunauer-Emmett-Teller (BET) surface area with increases in the extent of burnout, measured in a thermo gravimetric analyzer (TGA). The internal burning of soot is important for two reasons: the increased area leads to higher reaction rates, and the increased porosity resulting from internal burning can lead to particle fragmentation. The variability of the oxidation rate of carbon with  $O_2$  can be appreciated from the wide range of rates given by the different correlations of soot oxidation summarized in Figure 4, for an assumed surface area of  $120 \text{ m}^2/\text{gram}$  and an oxygen partial pressure of 0.1 atmospheres. Table 3 provides selected information on the experimental methods and carbons used in the studies leading to the rates summarized in Figure 4. Figure 4 shows that the carbon reactivity varies by as much as three orders of magnitude. In general, various investigators have found lower rates when using more ordered carbons for their studies. Clearly rates much higher than those predicted by the NSC correlation have been reported. The investigators hypothesize that these differences are a result of different soot structures and specific surface areas of the soots or carbons used in the different studies.

- Base Sphero carb
  - $L_{a,avg} = 11.1 \text{ \AA}$
- 50 % Conversion
  - $L_{a,avg} = 13.1 \text{ \AA}$
- 75% Conversion
  - $L_{a,avg} = 14.5 \text{ \AA}$



Figure 2. Illustration of how the ordering of carbons varies with combustion conditions, in this case increasing with carbon conversion (Kandas, 1997).

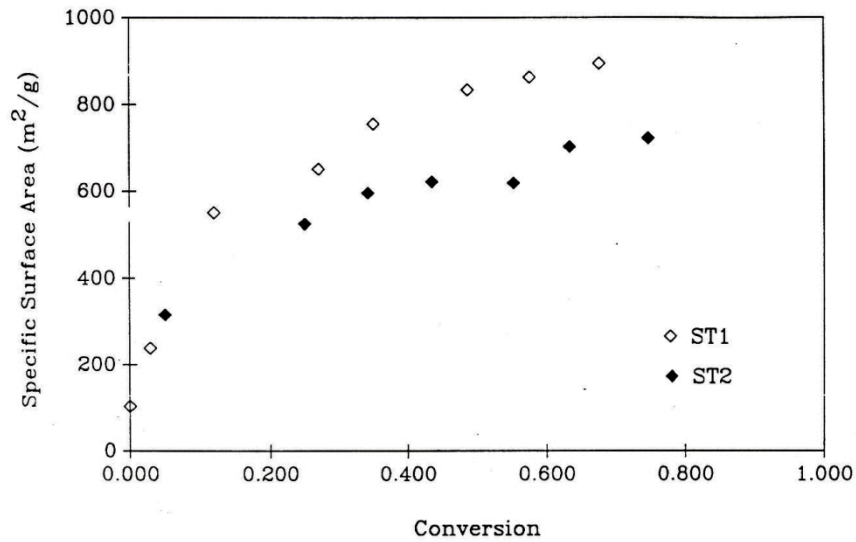


Figure 3. Internal surface areas of two soots (ST1 ethylene soot, ST2 ethylene soot with 2% Ca catalyst) as a function of fractional oxidation.

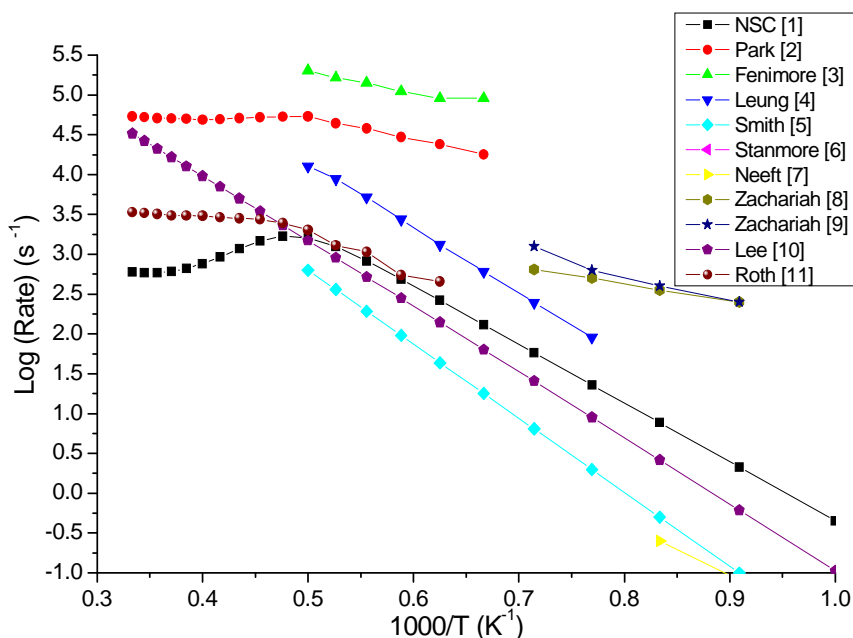


Figure 4. Selected rates of oxidation of carbon by O<sub>2</sub> reported in the literature.

Table 3. Studies used to generate rates in Figure 4.

Number	Investigators	Carbons & experimental conditions
1	Nagle and Strickland-Constable	High velocity oxidant streaming over heated graphitized carbon.
2	Park and Appleton	Channel black and furnace combustion black, in a shock tube over 1700-3000 K and 0.05-0.13 atm of oxygen
3	Fenimore and Jones	Ethylene-flame-produced soot, in a two-stage burner over 1530-1800 K and 0.0001-0.3 atm of oxygen
4	Leung et al.	Ethylene and propane laminar non-premixed flames
5	Smith	Porous and non-porous carbons over 580-2200 K
6	Stanmore et al.	Diesel soot
7	Neeft	Flame soot and diesel soot
8	Higgins	Diesel soot
9	Higgins	Ethylene diffusion Flame soot generated in a Santoro-type burner
10	Lee	Hydrocarbon laminar diffusion flame

In most combustion carried out under fuel-rich or slightly lean conditions, oxidation by OH\* dominates over that by O<sub>2</sub>. Therefore, few have questioned the widespread use of the NSC rate

for O<sub>2</sub> since it was a minor contributor to soot oxidation. But the NSC rate with its two reactive sites is best used for graphitic-like structures that have predominantly two carbon sites and intrinsically lower reactivities. Studies on chars with disordered structures, by contrast, have shown that carbon reactivity can be modeled by sites with a distribution of adsorption and desorption energies (Haynes and Newberry 2000). This approach leads to a rate expression with a fractional order for gaseous oxygen (Hurt and Haynes 2005), rationalizing the power-law correlations, which have been used for decades. It is the objective of the proposed study to investigate the oxidation of soot produced under conditions relevant to gas-turbine combustors and to develop the appropriate kinetic expressions.

## MATERIALS and METHODS

The study, designed to take advantage of the developments in sampling, sizing, and structural characterization of soot, investigated the kinetics of soot oxidation with O<sub>2</sub> and OH\* and examined the role of soot structure, as influenced by fuel, soot surface area and particle size distribution.

### Burner System

The University of Utah's two-stage burner (Figure 5), designed after the apparatus of Neoh (1981), isolates the soot oxidation mechanisms from the formation steps (Neoh, 1981; Merrill 2005; Lighty et al., 2008, Echavarria et al., 2011). In this system, soot was generated in a fuel-rich premixed flame (bottom burner), which serves as the first stage. Soot was then oxidized under lean conditions and slightly rich conditions in the top burner. Soot was derived from different sources to account for the effect of the parent fuel on soot oxidation. In the first experiments soot was produced in an ethylene/air flame ( $\Phi_1 = 2.5$ ). For the jet fuels or surrogate mixtures soot was formed in a surrogate/air flame ( $\Phi_1 = 2.11$ ). The surrogate consists of a mixture m-xylene/n-dodecane with a volume ratio of 10/90 (referred to as "surrogate") which approximates the range of aromatic concentrations in JP-8 (Edwards, 2005). For comparison, soot was also generated using m-xylene/air ( $\Phi_1 = 1.7$ ) and n-dodecane/air flames ( $\Phi_1 = 2.15$ ) that represented the pure components of the surrogate mixture. The soot-laden combustion gases were passed through a secondary flat-flame premixed burner where soot was burned out under fuel lean ( $\Phi_{\text{overall}} = 0.8$ ) and slightly fuel rich ( $\Phi_{\text{overall}} = 1.14$ ) conditions. The overall equivalence ratio is defined by the following equation:

$$\Phi_{\text{overall}} = [\text{Fuel}/(\text{Air}_1 + \text{Air}_2)]_{\text{actual}} / [\text{Fuel}/\text{Air}]_{\text{stoichiometric}}, \quad (4)$$

and the stoichiometry of the secondary burner was controlled by the injection of air and/or H<sub>2</sub> (see Table 4) through the secondary air port. H<sub>2</sub> helped to obtain more stable flames in the top burner for the conditions where soot was generated in m-xylene/air and n-dodecane/air flames. Air and gaseous fuels were fed into the two-stage burner using 5850 E mass flow controllers and liquid fuels (surrogate) were vaporized and mixed with preheated air prior to entering the first burner. Temperature along the feeding line and below the tube bundle in the first burner was controlled at 250 °C to avoid fuel recondensation. An initial vaporization system consisted of a bubbler which was later changed for a commercial (Mesoscopic Devices

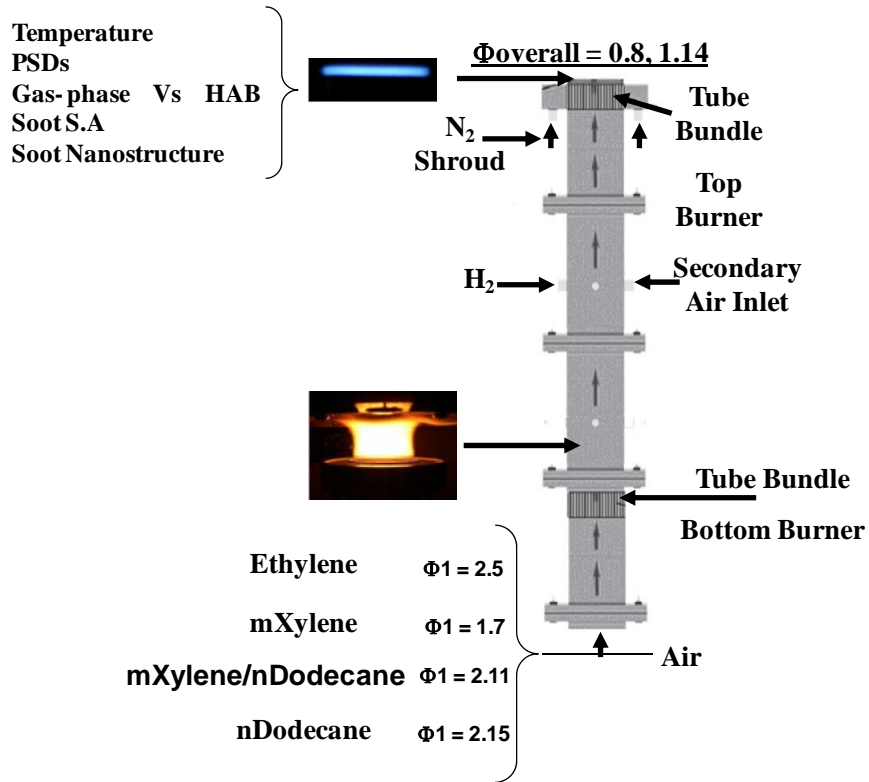


Figure 5. Two-Stage Burner

Table 4. Summary of Experimental Conditions

System	$\Phi_{\text{overall}}$	Bottom Burner		Top Burner (secondary gas inlets)	
		Fuel, g/min	Air, g/min	Air, g/min	H <sub>2</sub> , g/min
Ethylene/ Air	0.8	0.734	4.322	9.220	0
	1.14	0.734	4.322	5.135	0
Surrogate /Air*	0.8	0.835	5.844	9.570	0
	1.14	0.835	5.844	4.960	0
m-Xylene/Air	0.87	0.728	5.797	7.408	0.0466
	1.14	0.728	5.797	4.280	0.0466
n-Dodecane/Air	0.8	0.843	5.852	10.945	0.0254
	1.14	0.843	5.852	5.941	0.0254

\* Surrogate mixture consist of 10 % vol m-Xylene and 90 %vol. n-Dodecane

Inc.) vaporizer coupled to a syringe pump and temperature control system (see Figure 6). Both systems provided a uniform fuel flow to the burner. However, the system with the commercial vaporizer allowed a wider range of flow conditions and ensured that the vaporization process did not alter the fuel through thermal chemical reaction or preferential vaporization. To verify this, the vaporized fuel was captured in a cold solvent (dichloromethane) trap and analyzed using gas chromatography. The concentration of liquid samples before vaporization and after vaporization-condensation was found to be the same (see Figure 7). Experimental measurements of temperature, particle size distribution, gas-phase composition, soot surface area, and soot morphology and nanostructure were mainly performed within the top burner.

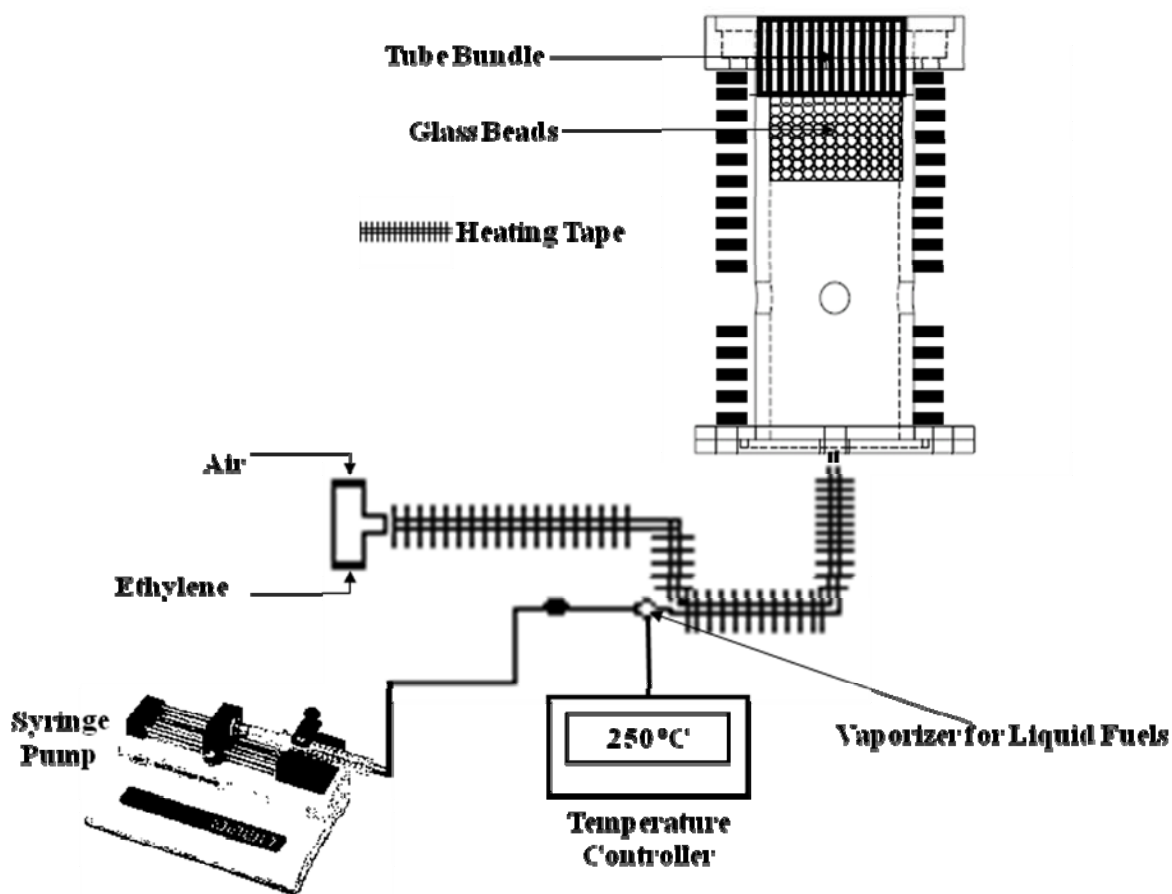


Figure 6. Schematic representation of the bottom burner showing injection system for liquid fuels.

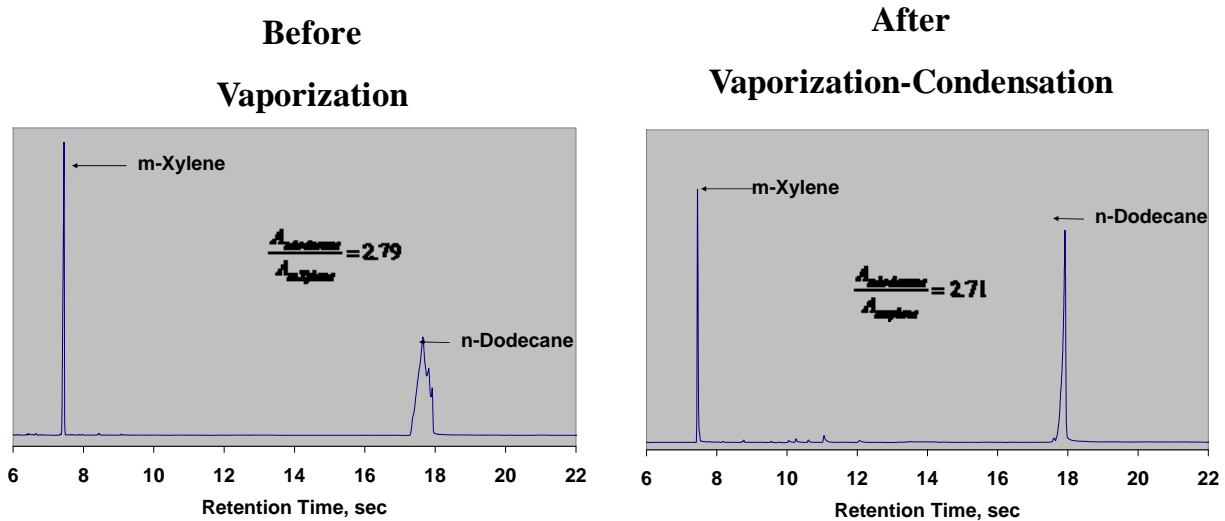


Figure 7. Chromatograms of the surrogate mixture before vaporization and after vaporization-condensation.

### Flame Temperature Measurements

Temperature profiles along the centerline of the top burner were measured using a 0.008” diameter uncoated Type-B thermocouples. Comparisons to uncoated versus coated yielded a difference in temperature of approximately 40°C which is below the typical uncertainty ( $\pm 50$ -100°C) for this thermocouple (McEnally et al., 1997; Shaddix, 1999). The thermocouple was inserted into the flame using a fast insertion mechanism (Figure 8). In this system the transient response of the thermocouple was recorded for 25 seconds at a sample rate of 50 samples per second. According to McEnally, et al. (1997), when a thermocouple is inserted into a sooty flame, particles will deposit on its junction due to the thermal gradient between the gas and the thermocouple. Thus a correlation of the transient response and the soot deposition rate could be used to estimate the local gas temperature and the local soot volume fraction without having to make assumptions about particle size distribution, particle optical properties or gas uniformity.

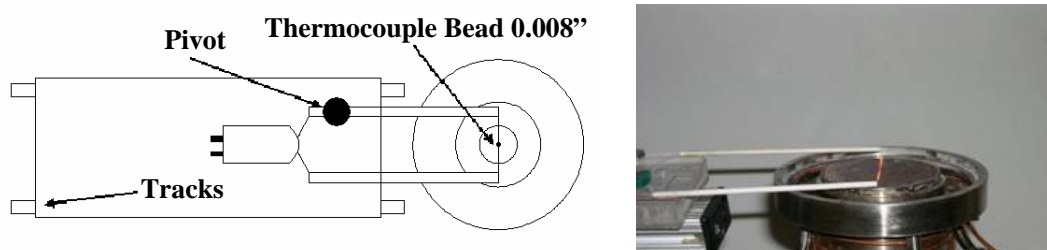


Figure 8. Fast response thermocouple setup.

Figure 9 presents typical profiles of the transient response of the thermocouple for both nonsooting and sooting conditions measured in the bottom burner for ethylene/air flames. Under

nonsooting conditions, the temperature of the bead increased rapidly and leveled off after reaching a maximum (see Figure 9a). By contrast, when soot is in the flame, it was driven to the bead surface because of the thermophoretic gradient between the flame environment and the cold bead surface. As result, temperature dropped continuously as soot deposited on the thermocouple bead, increasing both its diameter and emissivity. Once the bead was sufficiently coated, the emissivity of the bead was equal to the emissivity of the soot, and the temperature kept decreasing but at a different rate. In the top burner, temperature profiles showed similar behavior relative to Figure 9a.

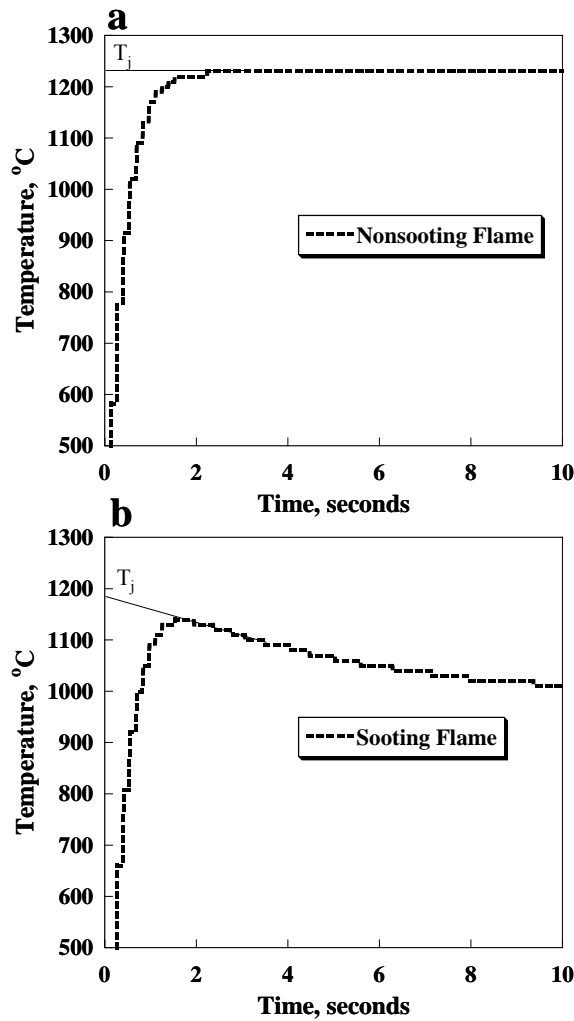


Figure 9. Transient response of the thermocouple under:  
(a) Nonsooting conditions and (b) Sooting conditions.

The temperature of the gases ( $T_g$ ) can be inferred by a quasi-steady energy balance at the junction as follows:

$$\varepsilon_j \sigma T_j^4 = \frac{k_{g0} Nu_j}{2d_j} (T_g^2 - T_j^2) \quad (5)$$

where  $T_j$  is the junction temperature,  $\varepsilon_j$  is the junction/bead emissivity,  $\sigma$  is the Stefan-Boltzmann constant,  $Nu_j$  is the junction Nusselt number,  $d_j$  is the junction diameter, and  $k_{g0}$  is the gas thermal conductivity.  $T_j$  can be estimated from the response curve of the thermocouple (Figure 9) by extrapolating the temperature at  $t = 0$  seconds. For this case, where we used B-type thermocouples, the emissivity can be estimated as a function of the temperature as follows:

$$\varepsilon = 0.1083 \ln(T_j) - 0.5644 \quad (6)$$

The Nusselt number has been evaluated for similar systems in the range from 2.26 to 2.35.  $k_{g0}$  is assumed constant, which is reasonable for combustion gases at high temperature. Radiation correction performed for the data in Figure 9 produced  $T_g$  of 1648 K and 1580 K for the nonsooting and sooting conditions respectively.

### Particle Size and Concentration

Particle size distributions and soot concentration were measured with a scanning mobility particle sizer (SMPS). This system consisted of a TSI 3080 classifier with nano and long differential mobility analyzers (DMA) and a 3025 ultrafine condensation particle counter (UCPC). Nano and long-DMAs and different impactor sizes (0.0457 and 0.071 cm) were used to cover PSDs in the size range from 3 to 660 nm (SMPS User's Manual). A general overview of the SMPS and sampling system is presented in Figure 10. In this system, particles from the flame were drawn into a horizontal sampling probe through a small orifice (0.32 mm diameter) and instantaneously diluted using a  $N_2$  stream at 30 lpm (STP). A small portion (1 lpm) of the exit stream was sent to the SMPS for particle sizing and number concentration measurements. The large portion of the exit was additionally diluted with air in an eductor and vented through a hood. The eductor not only diluted the large stream but also allowed controlling the pressure drop through the pinhole.

In the DMA (Chen et al., 1998; Maricq et al., 2000, 2004, 2005), an electrostatic classifier extracts a particular size fraction of particles from the polydisperse stream. The size-selected particle stream enters a Kr-85 neutralizer where the particles are engaged in frequent collisions with bipolar ions. Equilibrium is quickly reached and the particles carry a bipolar charge distribution. This charged aerosol then travels to the differential mobility analyzer. The DMA consists of two concentric cylinders: a collector rod that is maintained at a set negative voltage and an electrically grounded outer cylinder. This cylinder orientation creates an electric field. This electric field leads to the attraction of positively charged particles to the negatively charged collector rod. Particles within the user-defined range of electrical mobility exit the collector rod through a small slit and travel to an Ultrafine Condensation Particle Counter (UCPC) where the particles pass over a heated pool of alcohol and are saturated with alcohol vapor. Next, the aerosol passes into a condenser and is cooled. The alcohol condenses onto the surface of the

particles and they reach a size that is optically visible. At this point, the particles can be counted. The flow schematic for the electrostatic classifier is shown in Figure 11.

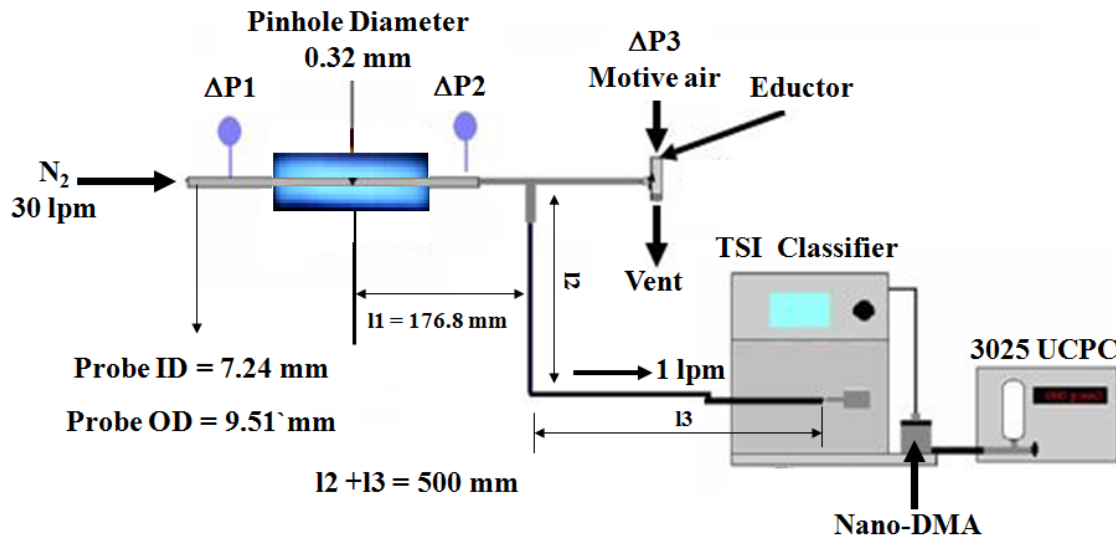


Figure 10. SMPS and dilution sampling system indicating probe ID, OD and line lengths.

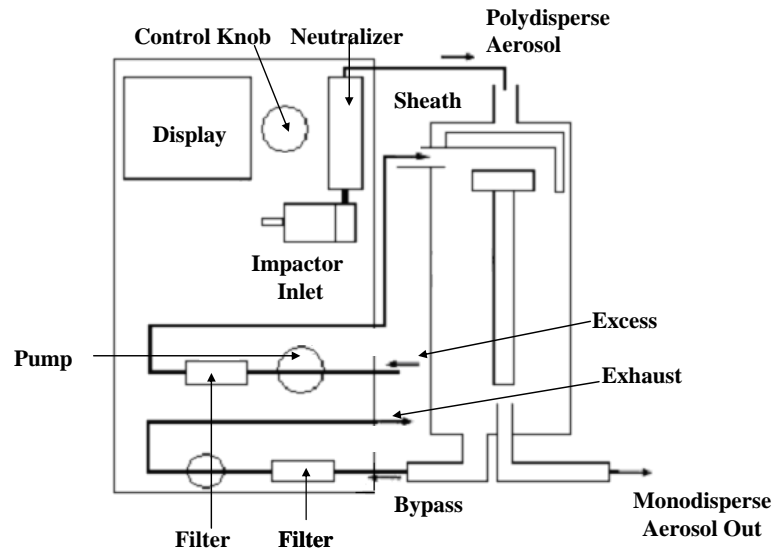


Figure 11. Flow Schematic for the Electrostatic Classifier (TSI Inc.).

### Dilution During the Sampling of Nanoparticles from Flames

An essential part in the study of aerosols is the ability to collect representative samples for analysis. These samples must accurately reflect the aerosol concentration and the particle size distribution. During online analysis by the SMPS in a flame, sampling issues range from particle

coagulation and agglomeration to diffusive losses in the sampling probe and sampling line. The most common method to minimize these problems during sampling from flames is by diluting the soot-laden combustion gases. The use of a cold dilution gas leads to an immediate quench of particle growth chemistry and minimizes the thermophoretic deposition of soot in the sample line that occurs when high-temperature, soot-laden gases come in contact with a cold surface. Zhao et al. (2003) showed that particle diffusion losses and particle coagulation can be minimized by systematically increasing the dilution ratio to a critical value where the particles size distribution function becomes independent of the dilution ratio. Experimentally, this critical dilution ratio was around  $10^4$ . However, other studies have shown that this value can range from  $10^3$  to  $10^4$  depending on equivalence ratio and combustion system utilized (Maricq et al., 2001; Zhao et al., 2003; Manzello et al., 2007; Echavarría et al., 2009; Abid et al., 2009; D'Anna, 2009).

In this study, we used a dilution system, similar to that of Zhao et al. (2003) and Kasper et al. (1997) with changes in probe size (OD = 9.51 mm) and pinhole diameter (0.32 mm), yielding dilution ratios greater than  $10^4$ , which minimized wall losses and quenched reactions or coagulation that would otherwise occur in the sampling system. Although, this system minimized diffusion losses and particle coagulation during sampling, corrections are still necessary to ensure that the final result reflects the actual evolution of the particle size in our flames. Corrections for penetration efficiency, into the probe and probe orifice, and diffusion losses during transport were mainly applied following the procedure presented by Minutolo et al. (2008). Corrections due to diffusion losses in the SMPS were conducted using the AIM software upgrade (TSI, In., 2006).

### **Dilution Ratio Calculation**

As previously mentioned, high dilution in the sampling point was critical to quench and minimize chemical reactions, coagulation and wall particle losses along the sampling system (see Figure 10). The dilution ratio ( $DR$ ) was defined as the volumetric flow of the dilution gas ( $N_2$ , 30 lpm, STP) divided by the sampled flow through the pinhole ( $Q_p$ , STP), or

$$DR = \frac{30}{Q_p(STP)} \quad (7)$$

$Q_p$  was corrected to standard temperature and pressure (STP) conditions from the temperature and pressure condition at the pinhole orifice ( $\sim 1000$  K,  $P_{atm}$ ). With this definition,  $DR$  can be evaluated as a function of the pressure drop ( $\Delta P_p$ ) or flow ( $Q_p$ ) through the pinhole orifice.  $Q_p$  was modified by adjusting the pressure drop ( $\Delta P_1$  and  $\Delta P_2$ ) through the sampling probe, accomplished via an eductor (Fox Valve Mini-eductors, Model 611210-060) installed downstream from the probe.

The eductor (Figure 12) was used similarly to a vacuum pump. However, instead of using electricity, it uses fluid mechanics to create certain amount of suction from the energy that is stored in a motive gas (air). The motive fluid was passed through a precision-machined nozzle. This led to a high velocity jet that induced a vacuum that pulled the diluted sample through the suction port. The inlet differential pressure ( $\Delta P_3$ ) of the motive gas was adjusted to increase or

decrease the suction, which in turn, changed the pressure drop through the probe and pinhole orifice.

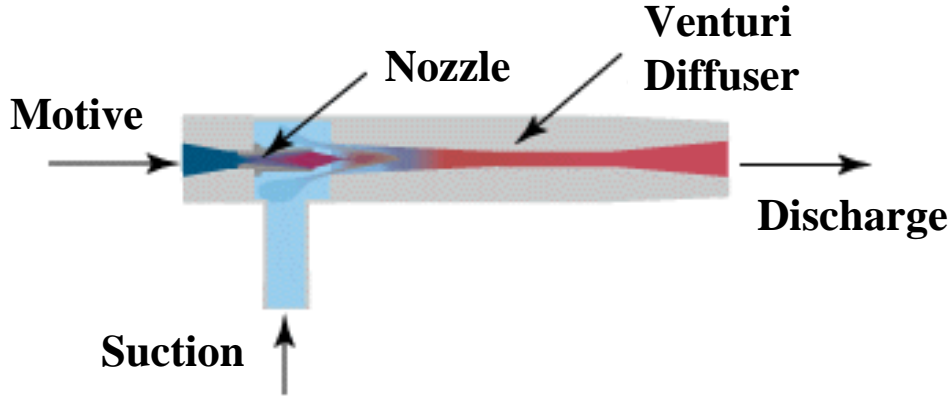


Figure 12. Schematic representation of the eductor.

Zhao et al., (2003) showed that the dependence of  $Q_p$  on the pressure drop ( $\Delta P_p$ ), pinhole diameter ( $dp$ ) and length ( $l$ ) can be described by the hydrodynamic theory for a low Reynolds number as follows:

$$Q_p = c \frac{\pi dp^4}{l \mu} \Delta P_p \quad (8)$$

where  $c = 0.0015$ , and the viscosity ( $\mu$ ) was obtained using the premixed code in CHEMKIN 4.1 for each condition.  $dp$  was equal to 0.24 mm and the length of the orifice was equal to 0.65 mm. These values were the result of a series of preliminary tests using different pinhole orifice sizes in order to minimize particle losses and coagulation in the dilution point. The pinhole diameter ( $dp$ ) was found to be satisfactory in the range from 0.2 to 0.32 mm ID. Below this range, significant particle losses and pinhole clogging was observed, and above 0.32 mm it was not possible to get enough dilution to minimize wall losses and coagulation along the sampling line. The length of the pinhole orifice ( $l$ ) was reduced until the PSD converged to a single result. The pressure drop through the pinhole orifice ( $\Delta P_p$ ) was estimated as the average between  $\Delta P_1$  and  $\Delta P_2$ .  $\Delta P_1$  and  $\Delta P_2$  were measured experimentally using U manometers, since the pressure drop was expected to be very small; an oil-like fluid with a specific gravity equal to 0.856 was utilized. To use Equation (7) and (8) correctly, it was necessary to account for the change in pinhole diameter due to soot deposition.

Figure 13 presents the change  $Q_p$  through the pinhole as a function of  $\Delta P_3$  and the change in dilution ratio with  $Q_p$  for studies on soot oxidation.  $Q_p$  was observed to increase with increasing the inlet pressure through the eductor ( $\Delta P_3$ ), which was a direct result of the increase in suction. On the other hand, the dilution ratio was found to be inversely proportional to  $Q_p$  as expected and as shown in other studies (Zhao et al., 2003, Abid et al., 2008). Experiments during soot oxidation were mainly carried out in the  $DR$  range from  $10^3$  to  $10^4$ . The uncertainty of this

methodology to calculate the dilution ratio has been reported in the literature in the range from 20 to 40 % (Manzello et al., 2007; Echavarria et al., 2009; Abid et al., 2009). The experimental error found in this study fell into that range and it became the main source of uncertainty in the measurements of number and mass concentration obtained from the integration of the PSDs.

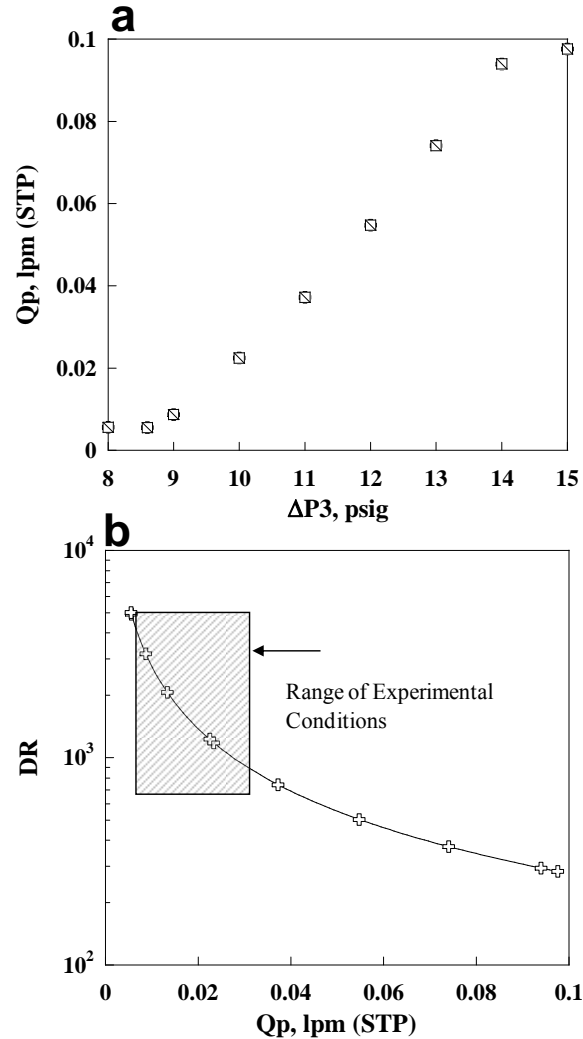


Figure 13. Dilution ratio calibration (a)  $Q_p$  as a function of  $\Delta P_3$  and (b) DR as a function of  $Q_p$ .

### Corrections to PSDs

Corrections to PSDs for penetration efficiency into the probe and probe orifice, diffusion losses during transport and diffusion losses in the SMPS were necessary to ensure that the final result reflected the actual evolution of the particle size in our flames. Besides coagulation, particle diffusion losses along the sampling line and in the SMPS occur when the particles collide with a surface and remained together due to Vander Wal forces, electrostatic forces, and surface tension (Hinds, 1982). Another mechanism that can favor the diffusion of particles to the walls of the probe is the thermophoresis. However, it becomes negligible in this case since the temperature gradient inside the dilution probe was very small. PSDs are usually presented in the form of  $dN/d\log D_p$  versus  $D_p$ . Even though the SMPS can provide results in this form, it does not

account for particle losses and coagulation along the sampling line; therefore, it is necessary and recommended to recalculate  $dN/d\log Dp$  from the raw counts provided by the SMPS as follows:

$$\frac{dN_i}{d \log Dp} = \frac{Ci * DR}{Q * t_{SMPS} * \eta * d \log Dp} \quad (9)$$

where  $Ci$  are the raw counts provided by the SMPS,  $DR$  is the dilution ratio, and  $Q$  and  $t_{SMPS}$  are the sample flow and sample time through the SMPS, respectively. The product  $Q * t_{SMPS}$  represents the total volume of air sampled.  $\eta$  is the total sampling efficiency which is given by the product of the SMPS efficiency, efficiency into the probe, and efficiency through the sampling line.

$$\eta = \eta_{SMPS} * \eta_{probe} * \eta_{line} \quad (10)$$

The SMPS efficiency ( $\eta_{SMPS}$ ) can be estimated as the product of the efficiency for the ionization process ( $\eta_{ion}$ ), and the diffusion losses correction inside the instrument  $\eta_{SMPS-diff}$ . The ionization efficiency for a similar instrument has been reported by Sgro et al. (2008, 2009). It was based on Wiedensohler's equation, which describes the fraction of charged particles with diameters  $1 < Dp < 1000$  nm. The penetration efficiency through the SMPS ( $\eta_{SMPS-diff}$ ) has been estimated using the diffusion losses correction application of the SMPS software upgrade (TSI, Inc, 2006). This application includes the penetration efficiencies along the SMPS system.

The penetration efficiency into the sampling probe ( $\eta_{probe}$ ) accounts for the sampling efficiency into the line  $l_l$  where the flow is turbulent and in the sampling orifice where the Reynolds number may be approximated as laminar or creeping flow. The turbulent sampling efficiency ( $\eta_T$ ) can be estimated by:

$$\eta_T = \exp\left(\frac{-\pi * D * l_l * Sh}{Q_{N_2}}\right) \quad (11)$$

$$Sh = 0.0118 * Re^{7/8} * Sc^{1/3} \quad (12)$$

where  $D$  is the diffusion coefficient of particles,  $l_l$  is the length of the sampling probe,  $Q_{N_2}$  is the volumetric flow rate of the dilution gas corrected for the temperature and pressure conditions inside probe,  $Sh$  is the Sherwood number and is given by Equation (12). The diffusion coefficient can be estimated using the Stokes-Einstein equation for aerosols in terms of the particle mobility as follows (Hinds, 1982):

$$D = \frac{k * T * Cc}{3\pi * \mu * Dp} \quad (13)$$

where  $k$  is the Boltzmann constant,  $T$  is the temperature inside the probe which was found to be approximately 373 K,  $\mu$  is the dynamic viscosity,  $Dp$  is the particle diameter and  $C$  is the Cunningham slip correction factor calculated by (Kim et al., 2004):

$$C(Kn) = 1 + A * Kn \quad (14)$$

$$A = \alpha + \beta * \exp\left(\frac{-\gamma}{Kn}\right) \quad (15)$$

with parameters  $\alpha = 1.165$ ,  $\beta = 0.483$ , and  $\gamma = 0.997$  fitted for particle sizes up to 270 nm and for a Knudsen number from 0.5 to 83.

To calculate the penetration efficiency through the pinhole orifice ( $\eta_p$ ) two different approaches were used. First, flow through the pinhole orifice was assumed to be laminar and the penetration under this condition is given by (Minutolo et al., 2008):

$$\begin{aligned} Q_p &= 0.8191 * \exp(-3.657 * \delta) + 0.0975 * \exp(-22.3 * \delta) + 0.03250 * \exp(-57 * \delta) \\ &\quad \text{for } (\geq 0.0312, \\ \& \quad Q_p &= 1 - 2.56\delta^{(2/3)} + 1.2 * (\delta + 0.177\delta^{(4/3)}) \text{ for } (\leq 0.0312 \end{aligned} \quad (16)$$

$$\delta = \frac{\pi * D * l}{Q_p} \quad (17)$$

where  $\delta$  is the deposition parameter and  $l$  is the length of the tube. The particle diffusion coefficient can be calculated using Equation (13) for the temperature of the combustion products entering the pinhole orifice (~1000K). A similar approach for penetration efficiency in a tube under laminar conditions can be found in Hinds (1982).

It is essential to note that there were several uncertainties associated with the method described above to correct for particles losses inside the sampling orifice (Sgro et al., 2009). First, Reynolds numbers were between 0.3 to 25 depending on the dilution ratio, which suggests that the flow should be consider as creeping flow instead of laminar. As result, particle losses may be higher or lower than those estimated from laminar flow theory which assumes fully develop flow. Second, the temperature at the sampling orifice was extrapolated rather than measured experimentally. It has a direct effect on properties such as the particle diffusion coefficient, viscosity, density etc. which can impact the final results considerably. Even though these uncertainties can affect the final result, significant efforts were performed during the experiments to minimize them.

Another approximation to estimate particle losses in the sampling orifice has been discussed by Sgro et al., (2009). In this approach, the particle sticking efficiency ( $\gamma(Dp)$ ) is evaluated as a function of the particle diameter by the interaction potential between the particles and the orifice walls. Additionally, the effect of particle rebound after particles collide with the walls can be accounted for assuming that the number of collisions with the walls producing particle losses is equal to the product of the number of collisions and the particle sticking efficiency. Even though this second approach seems to be more realistic, no significant difference was obtained either by using it or the assumption of laminar flow through the pinhole orifice.

Figure 14 presents a summary of a typical result for  $\eta_{ion}$ ,  $\eta_{SMPS}$ ,  $\eta_T$ ,  $\eta_{line}$ ,  $\eta_p$ , and the overall penetration efficiency ( $\eta$ ). It should be taken into account that the total penetration efficiency can be considerably affected by different factors such as the dilution ratio used to collect the PSD

and the length of the sampling line in the laminar side ( $l_2+l_3$ ). The higher the dilution ratio the lower the flow through the pinhole, which in turn, reduced the sampling efficiency of the smaller particles and increased the experimental error. In addition, shortening the sampling line reduced particle losses, particularly in the laminar side. Using the data provided by Figure 14, the corrected PSDs can be obtained from the raw counts obtained in the SMPS.

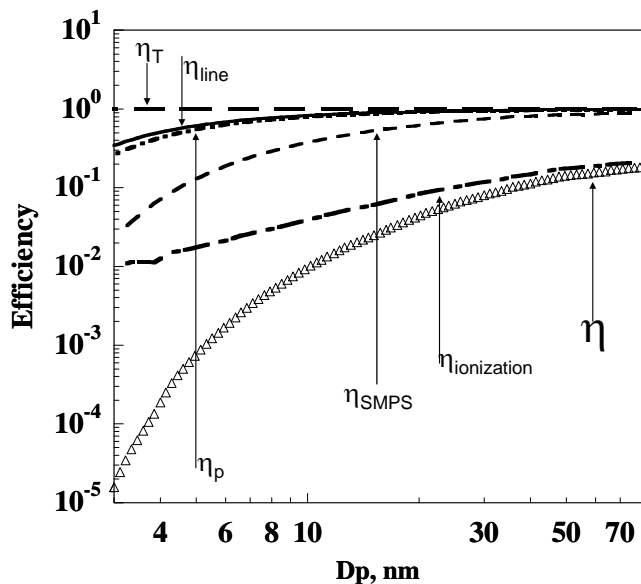


Figure 14. Penetration efficiencies through the turbulent side ( $\eta_T$ ), laminar side ( $\eta_{line}$ ), sampling orifice ( $\eta_p$ ), SMPS ( $\eta_{SMPS}$ ) and overall sampling efficiency ( $\eta$ ).

### Chemical Analysis

$H_2$ ,  $O_2$ ,  $CO$  and  $CO_2$  were isokinetically sampled and analyzed by online gas chromatography (VARIAN, CP-4900 Micro GC). The sampling system (Figure 15) consist of a water-cooled probe (0.2 cm ID) coupled to a filter ( $1\mu m$ ) trap followed by a chiller where water is removed from the gaseous stream. Flow through the system is controlled by a rotameter located in the inlet of the vacuum pump. A small sample of the exit stream is sent to the GC for gas-phase analysis and the other part is diluted with  $N_2$  and vented. The temperature inside the probe and in the filter trap was kept between  $150 - 200\text{ }^\circ C$  to avoid water condensation.

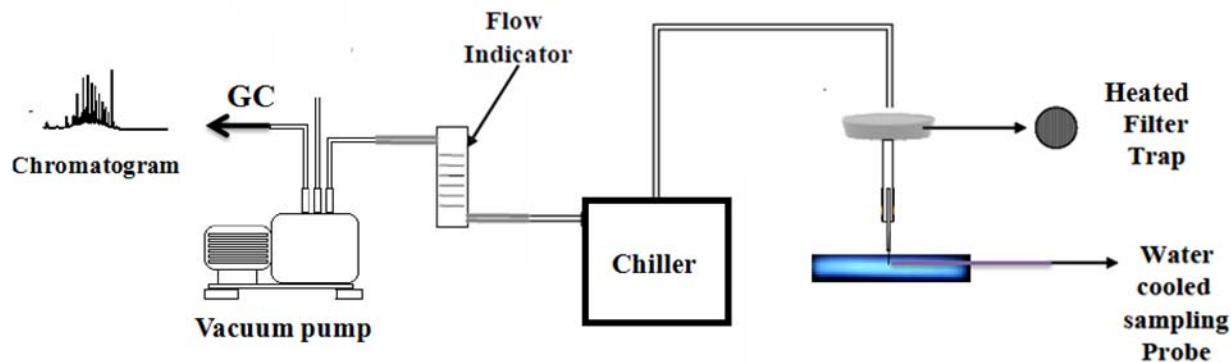


Figure 15. Sampling system to measure gas-phase compounds.

### Soot Surface Area Measurements

The surface area of the soot sample was measured gravimetrically by adsorption of CO<sub>2</sub> at 297K. The method consisted of injecting increasing concentrations of high purity CO<sub>2</sub> in helium (He) (0, 0.1, 0.2, 0.35, 0.5 and 1 mole fractions) into the TGA, and recording the weight change due to CO<sub>2</sub> adsorption. Initially, after the sample has been loaded into the TGA, the system was heated up to 150 °C in He or N<sub>2</sub> to remove adsorbed water. When the system cooled down, He was injected into the system at 1.85 lpm (STP). Between 40 to 60 minutes were allowed for the system to come to equilibrium for each point. Afterwards, CO<sub>2</sub> was fed into the TGA at a molar fraction of 0.1 in He. Four additional He/CO<sub>2</sub> gas mixtures switches were performed while the total flow and the system pressure (P<sub>atm</sub>) were maintained constant.

Buoyancy and drag effects are usually a concern during measurements of weight change in TGAs. To correctly estimate the mass of CO<sub>2</sub> adsorbed in the solid samples these effect must be accounted for. These effects are associated with apparent loss or gain in weight depending on changes of density in the system. A blank, where an experiment was run under the same experimental conditions with either an empty sample holder or the holder with an inert material (like quartz), was carried out to account for the weight changes due to buoyancy and drag effects (Campbell, 2005).

To test this methodology a powder coal sample (CA Corp.) with known BET surface area was used. The BET surface area for this sample was determined using a Tristar II 3020 Surface Area Analyzer (Micromeritics). The value found for this sample using the surface area analyzer was  $660 \pm 10 \text{ m}^2/\text{g}$ . Next the sample was run using the methodology described above. Figure 16 presents a complete CO<sub>2</sub> adsorption experiment. During the two first injections of CO<sub>2</sub> into the system ( $Y_{\text{CO}_2} = 0.1$  and  $Y_{\text{CO}_2} = 0.2$ ), there were slight increases in weight which were associated with CO<sub>2</sub> adsorption on the sample. For the other points ( $Y_{\text{CO}_2} = 0.35, 0.5$  and 1) adsorption is still occurring, however, weight dropped due to the major contribution of buoyancy effects caused by the difference in the densities of He and CO<sub>2</sub>. At the end of the experiment, CO<sub>2</sub> was again replaced by He, and CO<sub>2</sub> desorbed from the sample.

Figure 17 illustrates a test run under the same experimental conditions with an empty sample holder. This result was an indication that all the weight changes can be associated with CO<sub>2</sub> adsorption and to drag and buoyancy effects, which at higher CO<sub>2</sub> concentrations accounted for the major weight changes. These measurements with and without sample allowed establishing a relationship between the amount of CO<sub>2</sub> adsorbed and the CO<sub>2</sub> concentration or the partial pressure in the system. Figure 18 presents adsorption isotherms ( $\Delta W/W_0$  versus  $P_{\text{CO}_2}$ ,  $W_0$  is the initial sample weight) at 297 K for the commercial coal powder, and the soot samples collected in the two-stage burner at 0 and 2.5 mm under  $\Phi_{\text{overall}} = 0.8$ . The methodology to extract the results for the soot samples was the same to that in the coal sample (CA corp.) These results were further analyzed to obtain soot surface area using the Dubinin-Polanyi (DP) method (Du, 1990; Kandas, 1997). The DP method used Equations (18) and (19) to estimate the CO<sub>2</sub> micropore adsorption capacity of the samples:

$$\log x_{\text{CO}_2} = \log x_s - k \left( \frac{RT}{\beta} \right)^2 \log^2 \frac{P_s}{P_{\text{CO}_2}} \quad (18)$$

$$P_s = 10^{-874.34/T+4.7386} \text{ atm} \quad (19)$$

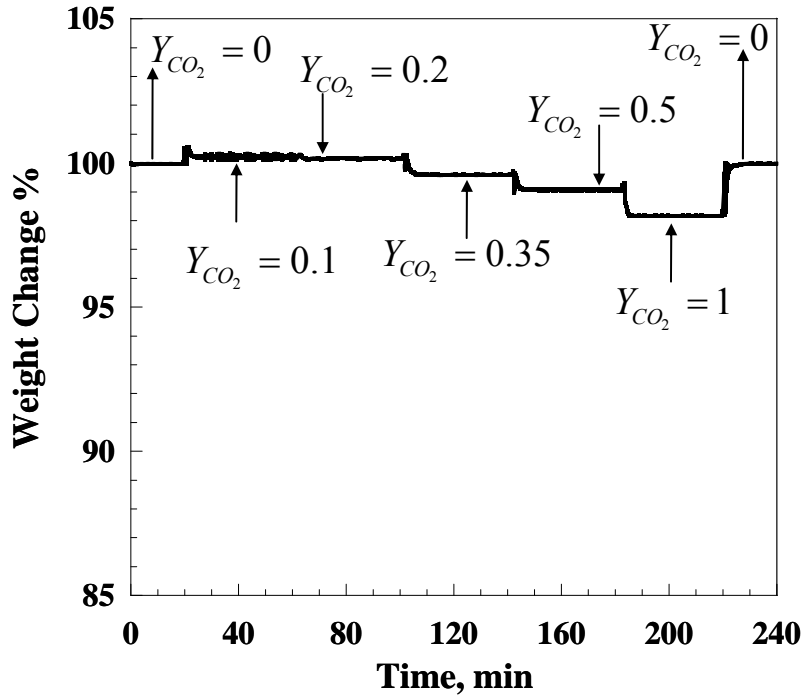


Figure 16. CO<sub>2</sub> adsorption test on commercial coal powder (CA Corp.) at 297 K.

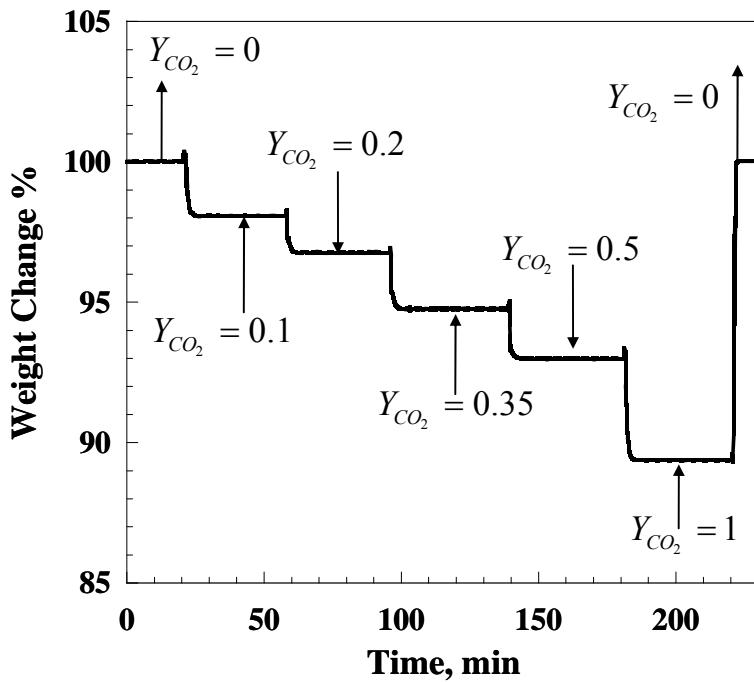
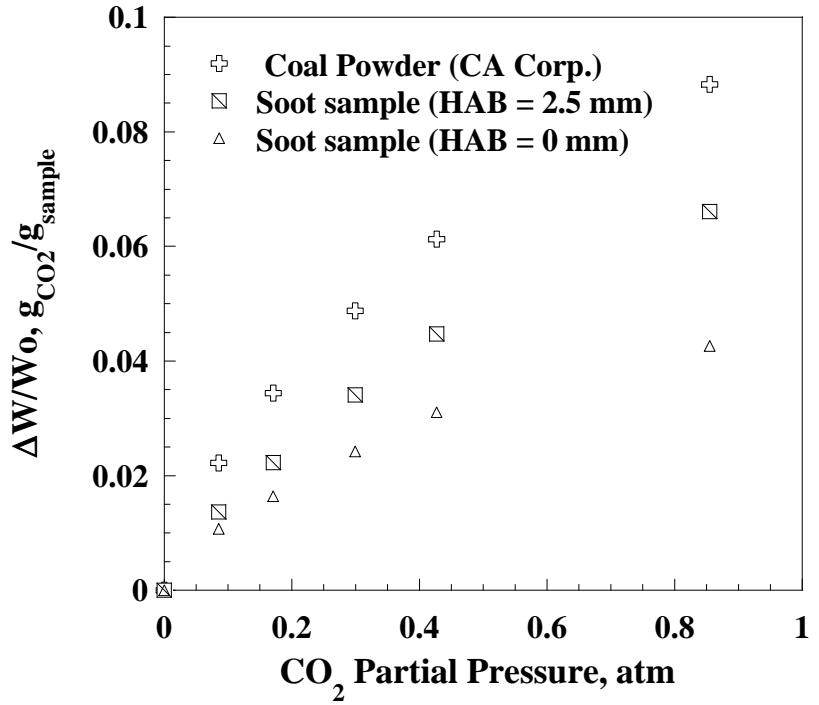


Figure 17. CO<sub>2</sub> adsorption test carried out on an empty sample holder. Weight changes were due to drag and buoyancy effects.

Figure 18. CO<sub>2</sub> adsorption capacity as a function of the CO<sub>2</sub> partial pressure on coal powder (CA corp.), and soot samples collected in the two-stage burner under a  $\Phi_{\text{overall}} = 0.8$  at 0 and 2.5mm.



A plot of  $\log x$  versus  $\log^2 (P_s/P_{CO_2})$  yielded straight lines (see Figure 19) for the coal sample and for the two soot sample collected in the two-stage burner. The monolayer adsorption capacity was obtained from the intercept and the specific micropore surface area was calculated as follows:

$$SA(m^2 / g_{\text{sample}}) = \frac{x_s N_o \sigma_{CO_2}}{M_{CO_2}} \quad (20)$$

$N_o$  is the Avogadro's number,  $\sigma_{CO_2}$  is the cross-sectional area of a CO<sub>2</sub> molecule (0.17 nm<sup>2</sup>) and  $M_{CO_2}$  is the CO<sub>2</sub> molecular weight. Using this approach, surface areas of  $560 \pm 40$  m<sup>2</sup>/g,  $282 \pm 35$  m<sup>2</sup>/g and  $494 \pm 27$  m<sup>2</sup>/g were obtained for the coal powder sample, soot sample at 0 mm (overall = 0.8, ethylene/air flames) and soot sample at 2.5 mm (overall = 0.8, ethylene/air flames) respectively. The coal sample was 15 % lower than the BET value. Two soot samples are also shown. The advantage of this method for our study, as compared to BET, is that it allows for an order of magnitude less sample. Since the system does not generate a lot of soot, this was an important consideration for these experiments.

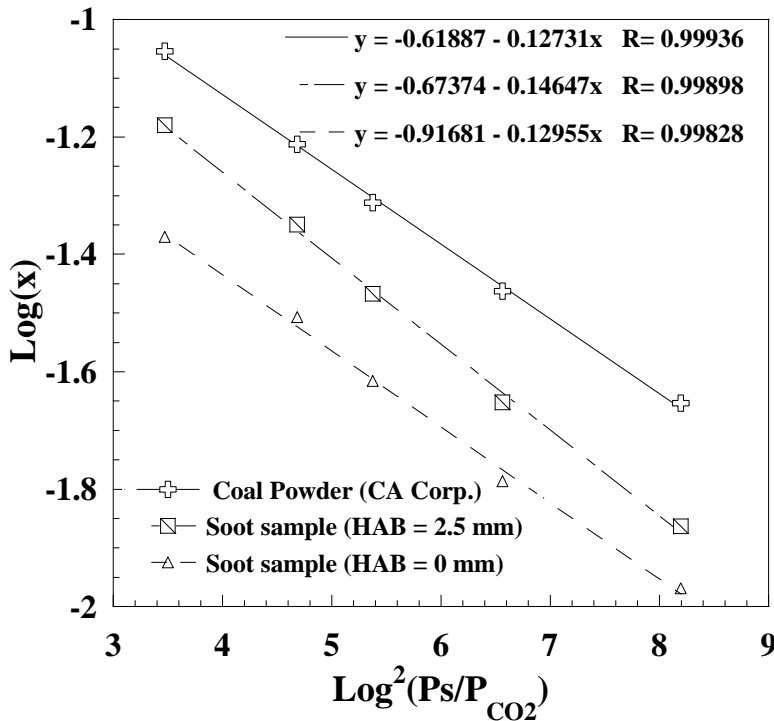


Figure 19. Dubinin- Polanyi plots showing the experimental data plotted according to Equation (18), and the linear regressions to obtain the monolayer adsorption capacity ( $x_s$ ) for the three sample run.

### Soot Morphology and Nanostructure

Samples for transmission electron microscopy (TEM) were taken using a thermophoretic probe commonly referred to as a “frog tongue” (see Figure 20). A TEM grid holder was attached to a piston and compressed air at 60 psig was used to quickly insert the TEM grid (200 mesh) into the flame (Dobbins, et al. 1987). Multiple insertions were necessary to get a representative soot sample on the grid. The grid was oriented with the face perpendicular to the gas flow. This way allowed for sampling at the exact position and the disturbance of the flame was minimal. Soot deposits on the grid because of the thermophoretic gradient between the cold grid and the hot flame. This technique allows “freezing” some heterogeneous reactions, avoiding changes on the soot morphology after the particles have impacted upon the cold surface. HR-TEM micrographs were produced using two FEI TEMs, Models Tecnai F30 and F20 EFTEM operated under 200 keV accelerating potential.

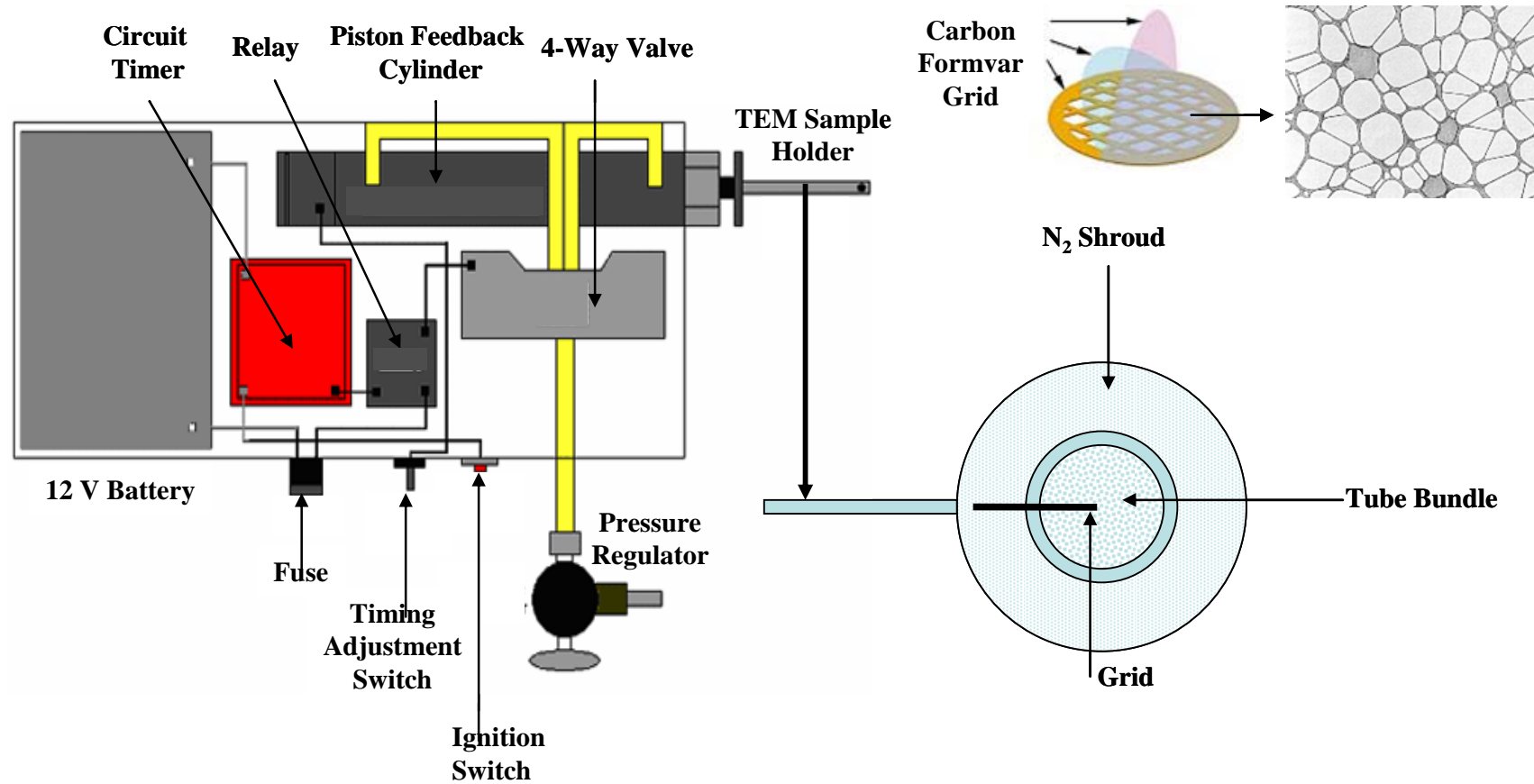


Figure 20. Thermophoretic sampling system for transmission electron microscopy analysis.

## HR-TEM Image Processing

From the structural data obtainable from HR-TEM images, the most commonly measured parameters by recent studies are the interlayer distance,  $d$ , the fringe length,  $L$ , and the fractional coverage of detected objects,  $F$  (Palotas et al., 1996; Sharma et al., 1999; Yang et al., 2006). Except for  $F$ , these are also the most easily verifiable by other techniques, such as X-Ray diffractometry (Aso et al., 2004). For the direct determination of  $d$ , to the best of our knowledge, all authors used the approximation proposed by Palotas et al. (1996), where the interlayer distance of two adjacent carbon fringes is the vector-vector distance of the two parallelized orientation vectors. These vectors are obtained by averaging their orientations and keeping their original centers of mass. Most recent publications place more emphasis on the classification of adjacent and parallel groups of fringes, called “stacks”. Detailed algorithms for deciding an object’s membership to stacks are presented in Sharma et al. (1999) and Yang et al. (2006). When considering data describing the stacking of layers, additional parameters arise such as the diameters of stacks, the number of layers in stacks and other derived indices, e.g. the crystallinity index proposed by Yang et al. (2006). Using whole distribution functions of  $d$  and the fringe orientation  $\theta$  can be expressive, because the amorphity of the texture - the deviation from perfect graphite structure - can be described by the statistical indices of these distributions. Shim and coworkers (2000) introduced several interesting order parameters, such as the 2D nematic order parameter  $S_{2,N}$  and the 2D polar order parameter  $S_{2,P}$ , defined as

$$S_{2,N} = \overline{2\cos^2(\theta_i)} - 1 \quad (21)$$

$$S_{2,P} = 1 - \overline{2\cos^2(\theta_i)} \quad (22)$$

Where  $\theta$  is a vector containing the angles between the orientation vectors of each fringe and a directional vector; the overline symbol means the arithmetic mean value of the elements of its argument. The directional vector is the reference vector for  $S_{2,N}$  and the vector pointing from the concentric center to the center of mass of fringe  $i$ . For a perfectly ordered graphite structure, where all fringes are stacked together and their orientations are the same, the nematic order parameter is 1; for a perfectly concentric, onion-like carbon structure, the polar order parameter is 1.

The approach used in this study is fundamentally different from the previously described ones (Toth et al. 2010). Instead of trying to separate fringes based on hypothesized criteria and extract data from bitmaps, we tried to simplify the images to “frames” that can be topologically characterized. These topological parameters are correlated to already defined properties. For noise filtration, we used bandpass gaussian filters in the frequency domain. Gaussian filters are better than ideal filters if the “ringing” caused by the sharp changes in the transfer function may lead to its unwanted detection, as in our case. Despite the advantages of using a low-pass filter as proposed by Sharma et al. (1999), bandpass filters were used, because of the additional intensity homogenizing properties of bandpass Fourier filtering (inhomogeneous luminance, e.g. large patches of darker or brighter pixels are considered very low frequency noise). The calculated frequency domains were centrally shifted, meaning that the smallest frequency was placed in the center of the map. Therefore, the coordinate system was chosen practically, so that the frequency of a point( $x\theta$ ;  $y\theta$ ) of the frequency map was calculated using the following equation:

$$F(x, y) = \sqrt{x^2 + y^2} \quad (23)$$

where  $x$  and  $y$  are the vertical and horizontal distances of a point from the center of the frequency map. Therefore, a two dimensional gaussian transfer function with a mean value at the central point is defined by the following equation:

$$O(x, y) = \exp\left(-\frac{x^2 + y^2}{2\sigma^2}\right). \quad (24)$$

In the case of a Gaussian distribution function,  $\sigma$  would be the variance. Here we use it as a parameter controlling the suppression of unwanted frequencies. A transfer function for a bandpass Gaussian filter can be generated by superimposing two Gaussian filters, with the high-pass component being complemented. Thus, the complete function can be defined as follows:

$$O(x, y) = \exp\left(-\frac{x^2 + y^2}{2\sigma_{LP}^2}\right) \cdot \left|1 - \exp\left(-\frac{x^2 + y^2}{2\sigma_{HP}^2}\right)\right| \quad (25)$$

where the indices *HP* and *LP* mean high-pass and low-pass, respectively. The idea behind the determination of  $\sigma$  is that the same extent of filtering can be achieved by equal “volume” ideal and Gaussian transfer functions. The ideal bandpass transfer function can be generally pictured as the difference of two cylinders; their radii  $D_{f,LP}$  and  $D_{f,HP}$  are the actual high- and low-pass cut-off frequencies and their height is 1. Hence, to find the functions  $\sigma_{LP} = f(D_{f,LP})$  and  $\sigma_{HP} = f(D_{f,HP})$  for  $I(x; y)$ , an  $m \times n$  size image, one can write

$$\int_{-n/2}^{n/2} \int_{-m/2}^{m/2} \exp\left(-\frac{x^2 + y^2}{2\sigma_{LP}^2}\right) dx dy = \pi D_{f,LP}^2 \quad (26)$$

$$\int_{-n/2}^{n/2} \int_{-m/2}^{m/2} 1 - \exp\left(-\frac{x^2 + y^2}{2\sigma_{HP}^2}\right) dx dy = m \cdot n - \pi D_{f,HP}^2 \quad (27)$$

Considering that most HR-TEM images are digitized in  $m \times m$  sizes, where  $m$  is a power of 2 to ease frequency filtering, so  $m = n$ , the integration of the left sides of (26) and (27) yields

$$2\pi\sigma_{LP}^2 \operatorname{erf}^2\left(\frac{m}{2\sqrt{2}\sigma_{LP}}\right) = \pi D_{f,LP}^2. \quad (28)$$

$$m^2 - 2\pi\sigma_{HP}^2 \operatorname{erf}^2\left(\frac{m}{2\sqrt{2}\sigma_{HP}}\right) = m^2 - \pi D_{f,HP}^2. \quad (29)$$

It is apparent that the two equations are symmetrical, therefore both  $\sigma_{LP}$  and  $\sigma_{HP}$  can be determined with the implicit transcendent equation

$$0 = \frac{D_{f,XP}}{\sqrt{2} \operatorname{erf}\left(\frac{m}{2\sqrt{2}\sigma_{XP}}\right)} - \sigma_{XP} \quad (30)$$

where  $XP$  means either low-pass ( $LP$ ) or high-pass ( $HP$ ). In practical situations, when  $D_{f,k}$  is significantly lower than  $m$ , Equation (30) can be simplified to

$$\sigma_{XP} \approx \frac{1}{\sqrt{2}} D_{f,XP}. \quad (31)$$

The relative error of this assumption is shown in Figure 21. Note that the maximum frequency of a repeating pattern that can occur on an  $m \times m$  size image is  $\sqrt{2}m/2$  and the values of the frequencies that need to be filtered increases as the ratio  $M$  decreases. In our case,  $\sigma_{LP}$  and  $\sigma_{HP}$  were determined at cut-off frequency values so that the low-pass component filtered out patterns repeating in more than 0.4 nanometers and the high-pass component filtered out large patches with relative frequencies lower than 10. After frequency filtering, the inverse Fourier transformed image was re-scaled and saturated to eliminate errors caused by inhomogeneous illumination. This step along with the use of bandpass Gaussian transfer functions instead of ideal ones was necessary because of the characteristics of the binarization method. For the detection process, we used a local, adaptive thresholding technique. Adaptive local threshold methods have been widely used in several image processing areas, e.g. in document binarization and handwriting recognition (Sauvola et al., 2000; Gatos et al., 2006). Local means that the value of  $T$  is not constant for the entire image; instead, the image is divided into smaller subregions, which have specific values of  $T$ . For an input 8 bit grayscale image  $GR$ , the matrix  $T$  was calculated in the following way:

$$\begin{aligned} \xi &\in [x - \mu, x + \mu] \cap [1, m] \\ \eta &\in [y - \nu, y + \nu] \cap [1, n] \\ t_{x,y} &= \operatorname{med}(gr_{\mu,\eta}) \end{aligned} \quad (32)$$

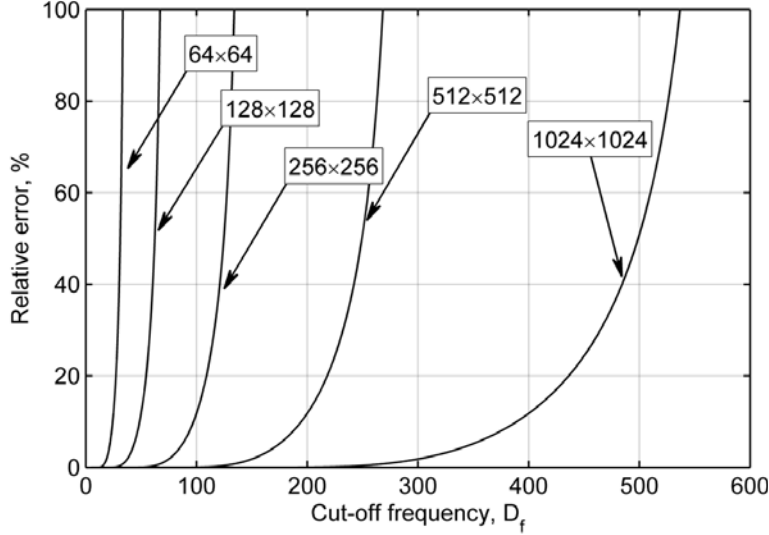


Figure 21. The relative error of Equation (31)

Meaning that for the point  $(x; y)$ ,  $t_{x,y}$  is the median of the intensities in the  $\mu \times \nu$  neighborhood on GR. As our images were digitized with an aspect ratio of 1, square-shaped median filters were used ( $\mu = \nu$ ). From our point of view, this binarization filter that produces the output binary image BW, defined in the following way:

$$bw_{x,y} = \begin{cases} 0 & \Rightarrow gr_{x,y} > t_{x,y}; \\ 1 & \Rightarrow gr_{x,y} \leq t_{x,y}. \end{cases} \quad (33)$$

There are several advantages to this method. First, median filtering has noise-removal effects, making the edges of the detected objects smoother, i.e. it tends to remove spur pixels, which is beneficial in the next step. Second, this method considers regional changes in intensity rather than absolute values, thus less focused or less intense fringes can be detected as well. Because of this feature, Gaussian frequency filtering and re-saturation are crucial steps to take prior to detection. In the next step, the detected pattern is skeletonized using the algorithm presented by Zhang et al, (1984). This iterative algorithm removes edge pixels and leaves only the backbone of the structure, but does not tend to leave spurs and diagonal arms (here we denote this operator as “net”). The remaining lines make a binary network of fringes  $N = \text{net}(\text{BW})$ , which is the input for topological analysis.

Two new structural parameters are proposed that can be measured on these connected networks. The distance deviation parameter,  $\Omega$  [nm], is the standard deviation of the Euclidean distance set  $E$ , while the junction parameter,  $\nu$  [1/nm], is the average number of branchpoints per network length unit. The calculation of  $\Omega$  can be achieved in a number of steps. First, the Euclidean distance transform of the binary network  $\Delta = \text{dist}(N)$  is computed. The Euclidean distance transformed value of a point  $b_{x,y}$  in a binary set  $B$  is its Euclidean distance to the nearest point with the value  $\sim b_{x,y}$ . Because the operator ‘net’ produces binary discrete networks without blocks of adjacent 1 values, for coordinates  $(x_0, y_0)$ , where  $n_{x_0, y_0} = 1$ ,  $\delta_{x_0, y_0}$  is always a regional minimum of  $\Delta$ . The points in the discrete regional maxima in  $\Delta$  correspond to half of the shortest

distances between the nearest two objects; the connected lines formed by the adjacent points of the regional maxima of  $\Delta$  are always positioned halfway between objects. In the second step, values belonging to the subset of regional maxima are extracted from  $\Delta$ . Generally, there are two obvious ways of doing this: one could either use numerical gradient operators to find regional maxima or apply the same thinning operator 'net' on an inverted network image. The use of numerical gradient operators was found to provide less reliable results, as it tends to detect pixels that do not belong to the above mentioned half distances, due to the edge-enhancing properties of the Laplacian operator. Instead, the coordinates of the half-distances were found by the thinning of  $\neg N$ . The Euclidean distance vector  $\vec{E}$  is defined by the following:

$$J = \{(\kappa, \lambda) : \text{net}(\neg N) = 1\} \quad (34)$$

let  $\vec{J}^*$  be a vector produced by reordering the elements of  $J$  so that

$$\vec{j}_i^* = (\phi, \chi), e_i = \delta_{\phi, \chi}, i \in [1, p] \quad (35)$$

The distance deviation parameter is defined as the standard deviation of the elements of  $\vec{E}$ :

$$\Omega = \sqrt{\frac{\sum_{i=1}^p (e_i - \bar{E})^2}{p}} \quad (36)$$

where  $\bar{E}$  means the mean value of the elements of  $\vec{E}$ . As can be seen,  $\Omega$  characterizes the texture in a complex way, as it is a parameter describing the uniformity of the lattice spacing distribution, the parallelism of the fringes and the order of their orientation as well. A presentation of the main steps of the algorithm can be seen in Figure 22.

To present the correlation of  $\Omega$  with  $S_{2,P}$  and  $S_{2,N}$ , we have conducted several stochastic simulations with artificially created fringe images. For the analysis of  $\Omega = f(S_{2,N})$ , the images were constructed to contain short fringes with randomly positioned centers of mass, but not allowing their contact. Their orientations were also randomized, by using a random generator yielding uniformly distributed numbers between  $[-q; q]$ . For the simulation of concentrically ordered structures, a large number of fringes were rendered around a concentric center, equally spaced from each other, with orientation vectors perpendicular rotated with these random values. Examples of these artificial images are presented in Figure 23.

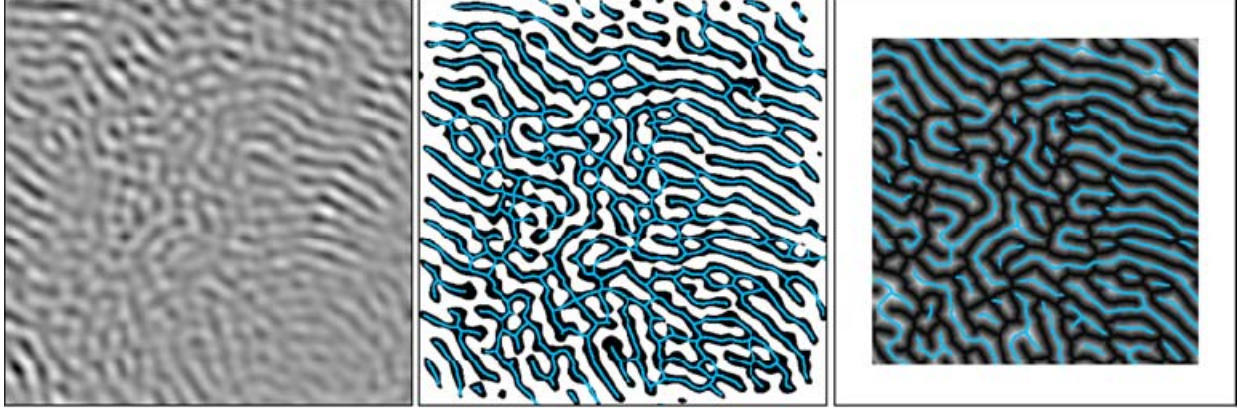


Figure 22. The main steps of the new algorithm for the determination of distance deviation parameter. Left: frequency filtered image. Center: binarized image (BW) with the thinned network indicated by blue lines (N). Right: the distance transform of N,  $\Delta$  and the extracted distances indicated by blue lines (E). The padding is necessary to eliminate errors caused by the median filter at image edges.

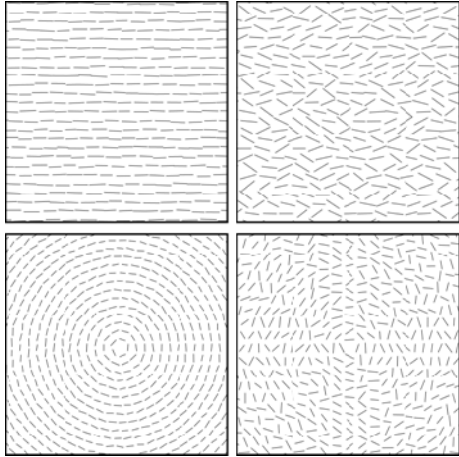


Figure 23. Examples of artificially created binary fringe images. Top left: oriented, axially symmetric set.  $S_{2,N} \sim 0:99$ . Top right: a shued version of the oriented axial set.  $S_{2,N} \sim 0:6$ . Bottom left: oriented, concentrically symmetric set.  $S_{2,P} \sim 0:99$ . Bottom right: a shued version of the oriented polar set.  $S_{2,P} \sim 0:6$ .

If we simplify Equation (22) to only consider concentric symmetry and the number of fringes on each image is large, both  $S_{2,N}$  and  $S_{2,P}$  can be estimated by

$$S_{2,X} \approx E(2 \cos^2(\Theta) - 1) \quad (37)$$

where  $\Theta$  is a random variable of uniform distribution with values of  $[-q; q]$  and E is the expected value of its argument. Solving Equation (37) yields

$$S_{2,X} = \frac{\sin(2q)}{2q} \quad (38)$$

Figure 24 presents the results of the stochastic simulations. For each parameter, a total of 10 tests were evaluated, with images containing 400 fringes. It is apparent, that the decrease in the order parameters resulted in an increase in  $\Omega$ , but the correlation is not linear. The measured values of  $\Omega$  increased monotonically in both cases, exhibiting steeply increasing periods at both ends of the curves. With our sets, changing the polar order parameter of the concentrically symmetric images induced less predictable changes in the values of the distance deviation parameter and the experimental data was more scattered. Seemingly,  $\Omega$  responded more sensitively to the changes of the axial order parameter. The monotony that can be observed in Figure 24, along with the fact that  $\Omega$  responds to many conditions – including these two order parameters - ensures that even slight changes in structure can be representatively monitored. The downside is that it is impossible to gain information about specific structural parameters solely by observing changes in the value of  $\Omega$ , it should rather be used as an intuitive empirical parameter of orderliness.

The calculation of the junction parameter is obtained by counting the branchpoints on the thinned networks and dividing this value by the measured length of the network. The detected branchpoints are filtered so that forks with an arm of length not exceeding a certain threshold are not considered branches. This way spur pixels and arms that are the results of the binarization of jagged contours are left neglected. The filtering algorithm works by checking each branchpoints' distance to the nearest endpoint of an arm, and pixels connecting too close branch-end pairs are deleted from the network. Branchpoints too close to each other are merged by binary dilations.

For the verification of the junction finding algorithm, we used HR-TEM images of Si 110 lattices. At certain magnifications, Si 110 single crystals look like perfect grids, where intense spots are believed to be Si atoms. For such arrangements and for infinitely large fields of view, the ideal value of  $\nu$  can be calculated as follows:

$$\nu = \lim_{m,n \rightarrow \infty} \left[ \frac{m \cdot n}{n(m-1)L + m(n-1)L} \right], \quad (39)$$

where  $m$  and  $n$  are the number of atoms that can be counted on the image horizontally and vertically and  $L \approx 0.2715$  nm (O'mara, 1990) (see Figure 25).

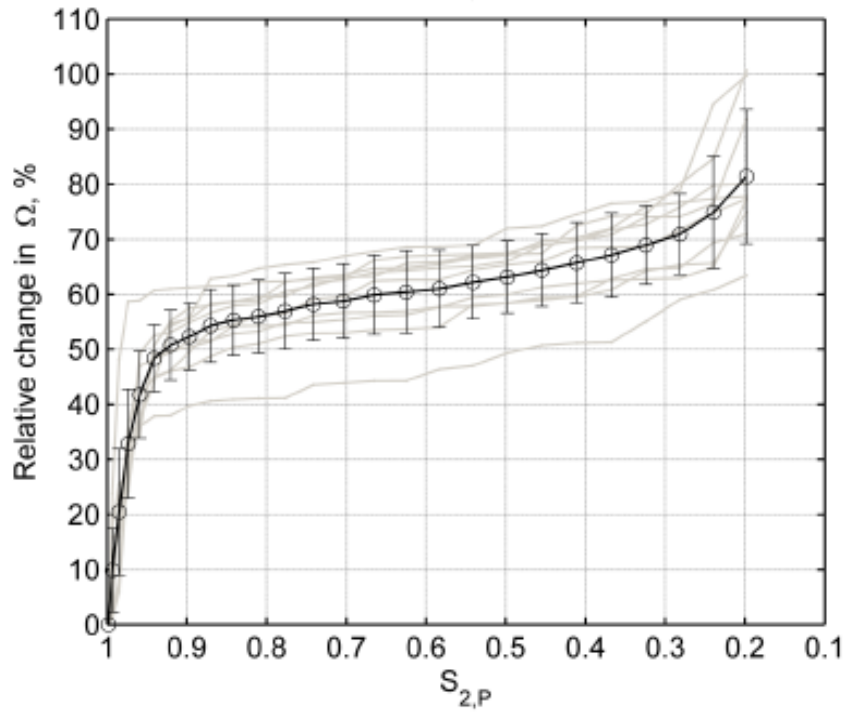
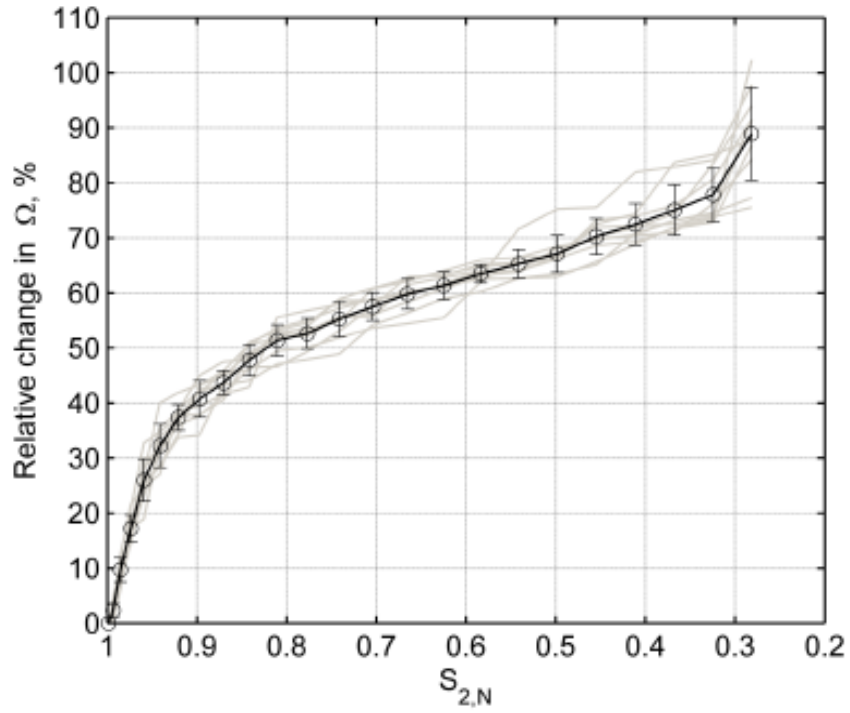


Figure 24. The results of the stochastic simulations. Top: the correlation of  $\Omega$  with  $S_{2,N}$ . Bottom: the correlation of  $\Omega$  with  $S_{2,P}$ .

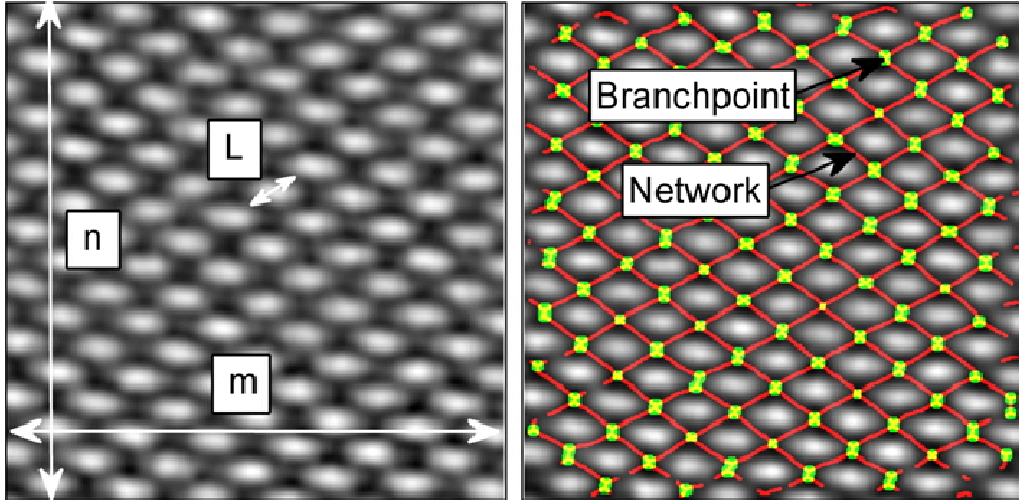


Figure 25. The calibration of the junction-finding algorithm. Left: a detail of a HR-TEM micrograph taken of an oriented Si single crystal. Right: The detected network (red lines) and branchpoints (green dots).

The horizontal axis illustrates the size of the detail that has been cut from a large lattice image. Since the horizontal and vertical dimensions of these details were not the same, an average size of

$$m^* = \sqrt{m \cdot n} \quad (40)$$

is shown.

Figure 26 shows the results of the verification. The continuous line represents the ideal, calculated value of  $v$ , while the dots mark the measured results; the trend can be easily seen. The errors of the algorithm are most commonly caused by duplicate branchpoints, crystal imperfections, inaccurate network extraction and image noise, however the magnitude of errors is in an acceptable range.

Similar to distance deviation,  $v$  is an empirical parameter of the orderliness of carbon texture as well: higher values indicate a more entangled structure, as the number of branchpoints increase with decreasing fringe lengths and overlapping layers. Its value is 0 for an ideal graphitic crystal with parallel fringes and no overlapping.

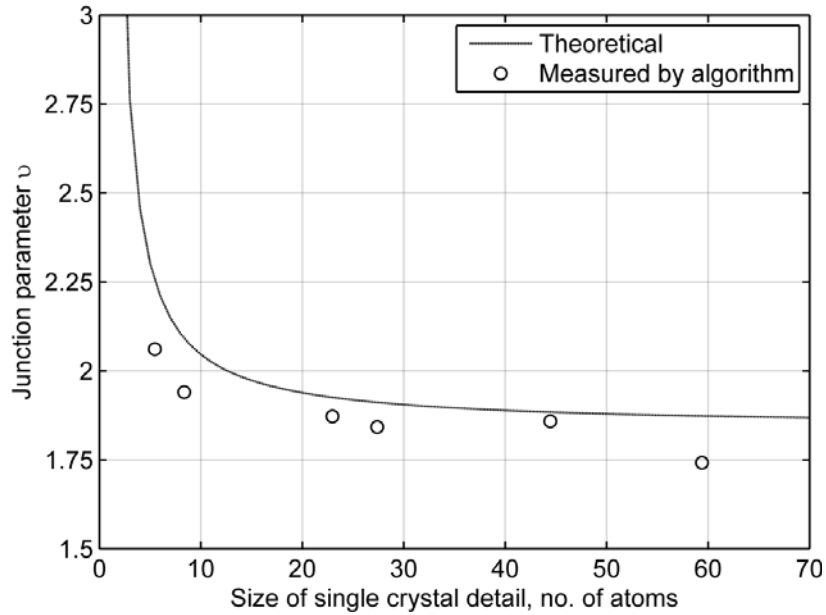


Figure 26. The verification of the junction-finding algorithm with Si 110 lattice images

### Methodology to predict OH\* & gas-phase species (H<sub>2</sub>, O<sub>2</sub>, CO, CO<sub>2</sub>)

Figure 27 represents a general overview of the methodology to predict the evolution of soot oxidizer species in the top burner. Experimental measurements of major gas-phase species (H<sub>2</sub>, CO, CO<sub>2</sub>, O<sub>2</sub>, N<sub>2</sub>) were taken within the top burner. The results of these measurements at the top burner surface as well as the mass flow rate and the temperature profile were used as inputs into CHEMKIN 4.1 to predict the evolution of major soot oxidizers (O<sub>2</sub>, OH\*) in the top burner. The CHEMKIN 4.1 modeling couples a 1D-premixed code to a detailed kinetic model defined by the user. The kinetic mechanism used in this project, developed by D'Anna et al. (2006), couples gas-phase chemistry with a sectional approach to follow the transition from gas-phase to nascent particles and soot oxidation. The details of the model have been reported previously (D'Anna et al., 2006, 2009). Although the model does not include reactions pathways that account for the fragmentation of particles, its gas-phase chemistry has been used in previous investigations to predict the concentration profiles of radicals such as H\*, O\*, OH\* etc. in premixed flames.

### Methodology to Obtain Soot oxidation Rates from Experimental Data

Soot oxidation rates ( $W$ ) were calculated from the experimental PSDs as a function of the height above the second burner from:

$$W \left( \frac{g}{cm^2 \text{ sec}} \right) = \frac{1}{A} \frac{dm}{dt} \quad (41)$$

where  $A$  was the surface area of soot particles per unit volume of gas,  $m$  was the total soot mass per unit volume of gas, and  $t$  was time. Area and mass were calculated directly from the SMPS diameter and number concentration assuming spherical particles. Allowance for the change of soot density with mobility diameter followed the procedures of Maricq et al. (2004). The time

interval was obtained from measurements of temperature, cross sectional area and volumetric flow rate.

These data were used to predict OH\* and O<sub>2</sub> concentrations which, in turn, were used in Equations (1) and (2).

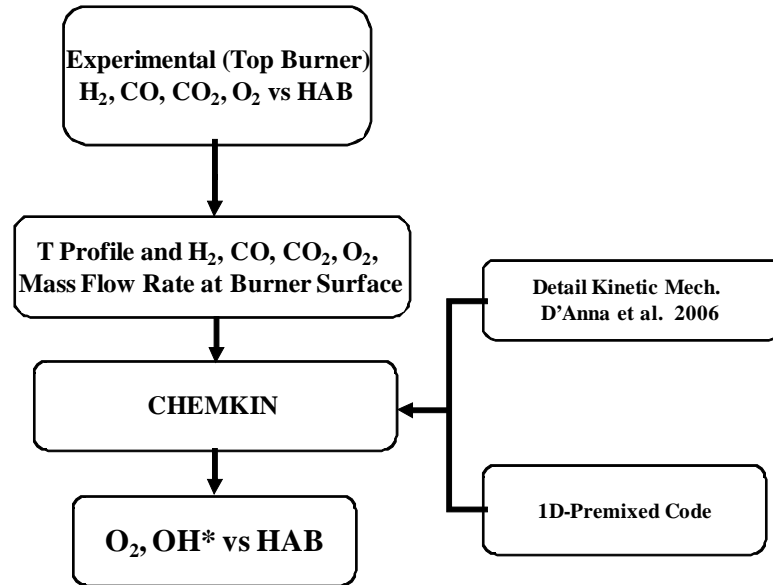


Figure 27. Schematic representation of the methodology used to predict the evolution of soot oxidizer species.

## RESULTS AND DISCUSSION

### Ethylene/air Flames

Temperature profiles were measured from the second burner surface up to 5 mm. Figure 28 illustrates the results for  $\Phi_{\text{overall}} = 0.8$  and 1.14. The difference in peak temperature is consistent with the evolution of the peak temperature in premixed flames as a function of the equivalence ratio. These temperature profiles were used as inputs into a detailed kinetic model to predict OH\* radical concentration profiles.

Soot size distributions were obtained as a function of the HAB for the lean and rich flames studied. Figure 29 presents the results of PSDs for  $\Phi_{\text{overall}} = 0.8$  (left) and  $\Phi_{\text{overall}} = 1.14$  (right) conditions in the locations where major changes took place. Data for the leanest flame ( $\Phi_{\text{overall}} = 0.8$ ) at HAB = 0 mm (Figure 29, left), showed that the initial distribution was mostly in the fine mode (particles diameter > 10 nm) with little contribution of particles less than 10 nm. This PSD did not change significantly up to 2.5 mm where particles in the ultrafine mode (particles diameter  $\leq 10$  nm) started to appear. In the range of HAB from 2.5 to 3 mm, particle mean diameter decreased from 36.7 nm to 3.7 nm, and at higher HAB, the particles started to burnout significantly, evidenced by a drop in number concentration. For  $\Phi_{\text{overall}} = 1.14$  (Figure

29, right), particles in the ultrafine mode almost disappeared when they reached HAB = 2 mm, and they are difficult to see at higher elevations. For the fine mode, the rate of oxidation increased significantly after HAB = 2 mm, and soot burnout dominated the oxidation process.

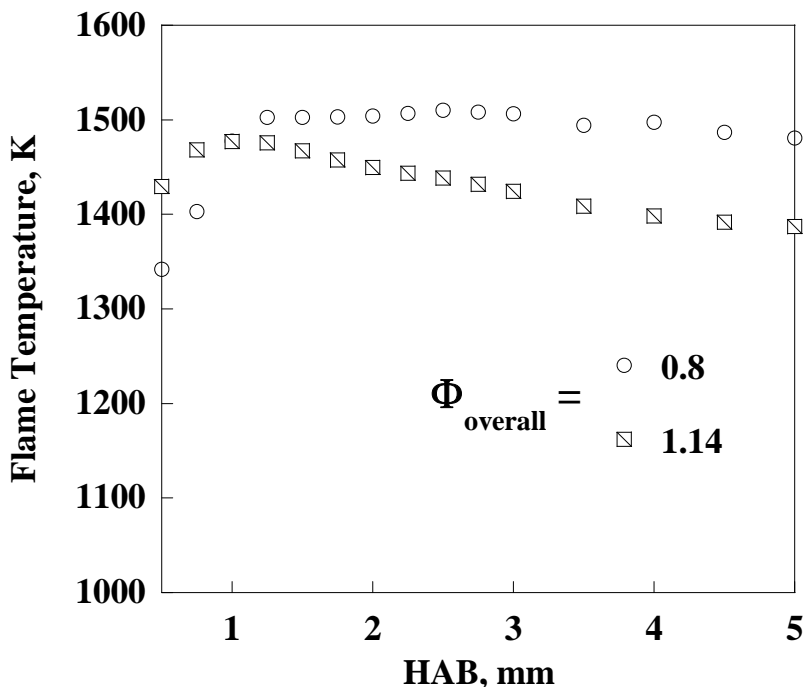


Figure 28. Top burner temperature profiles as a function of HAB for  $\Phi_{\text{overall}} = 0.8$  and 1.14. Thermocouple uncertainty  $\pm 50\text{K}$

Particles in size intervals of less than and greater than 10 nm (the detection limit of the SMPS was 3 nm) were integrated to provide measures of the number and mass concentration of the ultrafine and fine modes (Figure 30a and 30b, for the lean flame and Figure 30c and 30d for the rich flame). For the lean flame, the particle number (Figure 30a) and mass concentration (Figure 30b) in the ultrafine mode were observed to increase up to HAB = 3 mm. This behavior has been attributed to oxygen diffusion into the pores of the soot particles causing internal burning, which, in turn caused the soot aggregates to break apart (Neoh et al., 1981, 1985; Fenimore et al., 1967). It is also interesting to notice that this fragmentation took place for soot burnout less than 10%, which is considerably lower than the value observed by Neoh and coworkers (80% burnout). At HAB > 3 mm, particles in the ultrafine mode were almost completely combusted, as evidenced by the decrease in number and mass concentration. For the fine mode (Figure 30a and 30b), mass and number remained relatively constant up to 2.5 mm, and then started to decrease in the region between 2.5 to 3 mm; this can be attributed to the fragmentation and oxidation of the bigger particles. In the upper region of the flame, soot was almost completely burned out. For the richest flame (Figure 30c and 30d), both ultrafine and fine modes showed a decrease in number and mass concentration up to 3 mm. Higher in the burner, they leveled off with only minor changes in number or mass concentration. No evidence of fragmentation was observed for this flame in the range of HAB from 0 to 5 mm.

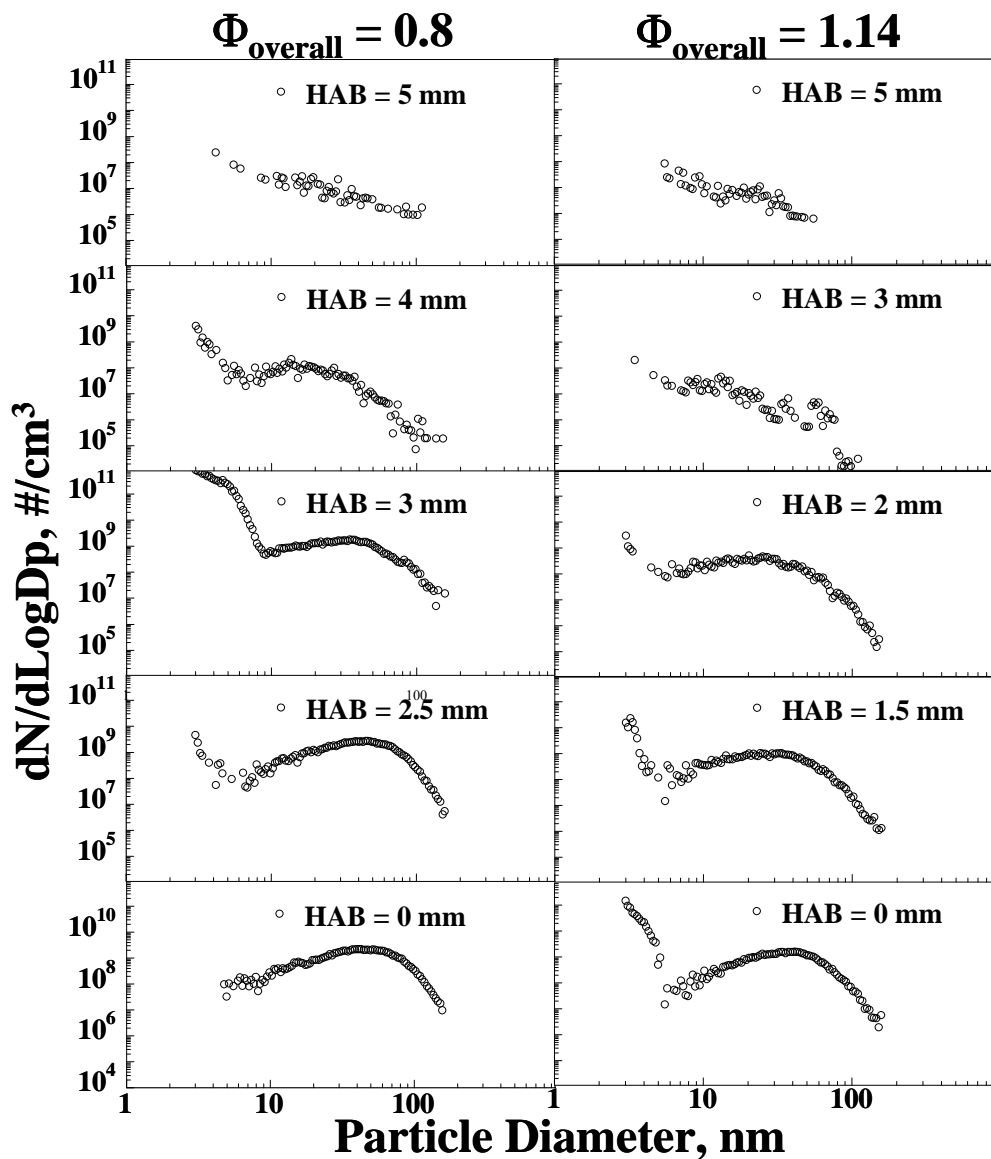


Figure 29. Experimental PSDs measured as a function of the height above the top burner for  $\Phi_{\text{overall}} = 0.8$  (left) and  $\Phi_{\text{overall}} = 1.14$  (right).

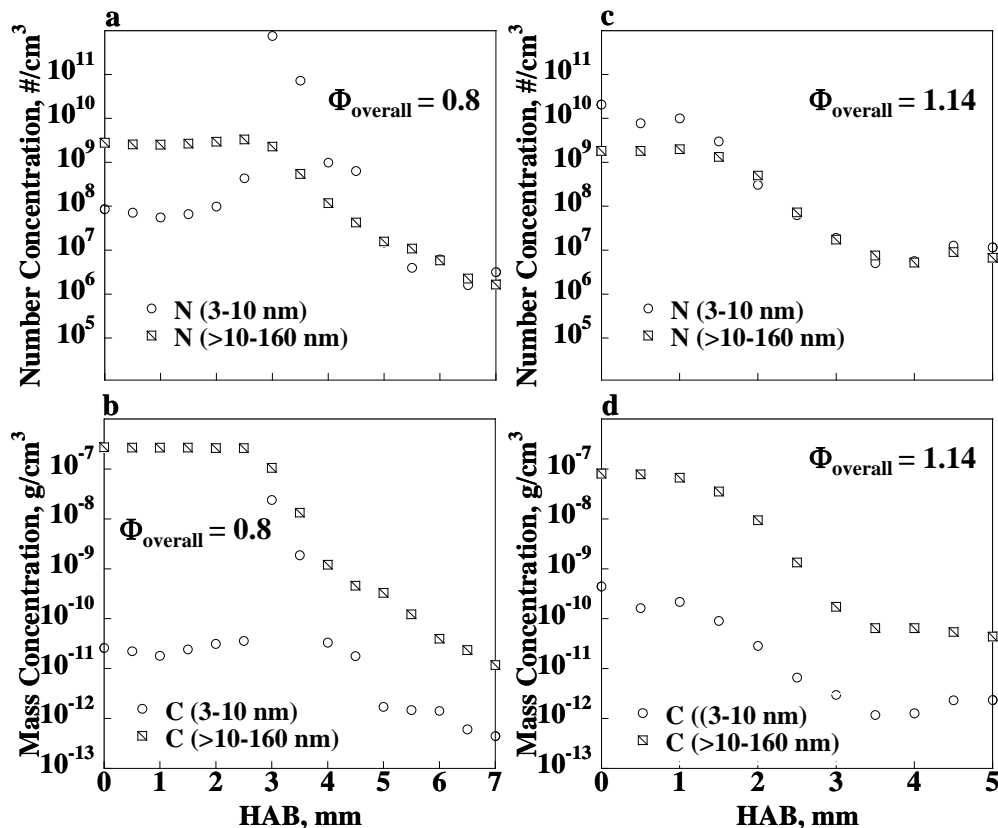


Figure 30. Integrated number and mass concentrations for fuel lean and fuel rich flames.

- a) Number concentration as a function of HAB for the ultrafine and fine modes ( $\Phi_{\text{overall}} = 0.8$ ).
- b) Mass concentration as a function of HAB for the ultrafine and fine modes ( $\Phi_{\text{overall}} = 0.8$ ).
- c) Number concentration as a function of HAB for the ultrafine and fine modes ( $\Phi_{\text{overall}} = 1.14$ ).
- d) Mass concentration as a function of HAB for the ultrafine and fine modes ( $\Phi_{\text{overall}} = 1.14$ ).

The concentration profiles of major gas species,  $\text{H}_2$ ,  $\text{O}_2$ ,  $\text{CO}$  and  $\text{CO}_2$ , were measured experimentally within the secondary flame using the isokinetic sampling system coupled to a gas-chromatograph described in the Materials and Methods section. Experimental temperature profiles (Figure 28), and experimental conditions measured at the surface of the top burner (mass flow rate,  $\text{H}_2$ ,  $\text{CO}$ ,  $\text{CO}_2$ ,  $\text{O}_2$  concentration, and PSDs) were used as inputs into the detailed kinetic model (D'Anna et al.) to predict the  $\text{OH}^*$  concentrations as a function of the HAB. Figure 31a and 31b compare the experimental measurements (open symbols) of  $\text{H}_2$ ,  $\text{O}_2$ ,  $\text{CO}$  and  $\text{CO}_2$  to model predictions (solid and dashed line) for  $\Phi_{\text{overall}}$  of 0.8 and 1.14 respectively. Predictions of  $\text{OH}^*$  are also presented and they are plotted with the right-side scale. Good agreement was obtained between the model results and the experimental data for these flames. Sampling effects due to the water-cooled probe were taken into account by shifting the model downstream as

supported in previous investigations (Echavarria et al., 2009; Zhao et al., 2003). As seen in these figures, at the burner surface (HAB = 0 mm), the main fuel components for the secondary, premixed flame were H<sub>2</sub> and CO. In the leanest flame, H<sub>2</sub> and CO were consumed in the upper region of the flame, oxygen dropped to about 6 %, and CO<sub>2</sub> concentrations increased and leveled. According to predictions, OH\* started to increase in the region where O<sub>2</sub> decreased and reached a maximum when the concentration of O<sub>2</sub> leveled off for HAB > 4 mm. The concentration of O<sub>2</sub>, CO and CO<sub>2</sub> started to show a significant change after an induction period up to 2.5 – 3 mm which is consistent with the trend of the PSDs obtained in the second burner, where major changes in number and mass concentration occurred. On the other hand, H<sub>2</sub>, CO, O<sub>2</sub>, CO<sub>2</sub> and OH\* were consumed and formed closer to the burner surface for the rich condition; the higher OH\* concentrations favor faster soot oxidation resulting in little or no fragmentation of the particles in this flame. The effect of other radicals and species, such as O\*, H<sub>2</sub>O, CO<sub>2</sub>, and CO, etc. on soot oxidation were not considered since previous studies (Neoh et al., 1981, 1985; Vierbaum et al., 2003) have shown that these species contributed negligibly to the oxidation under experimental conditions similar to those in the present experiments.

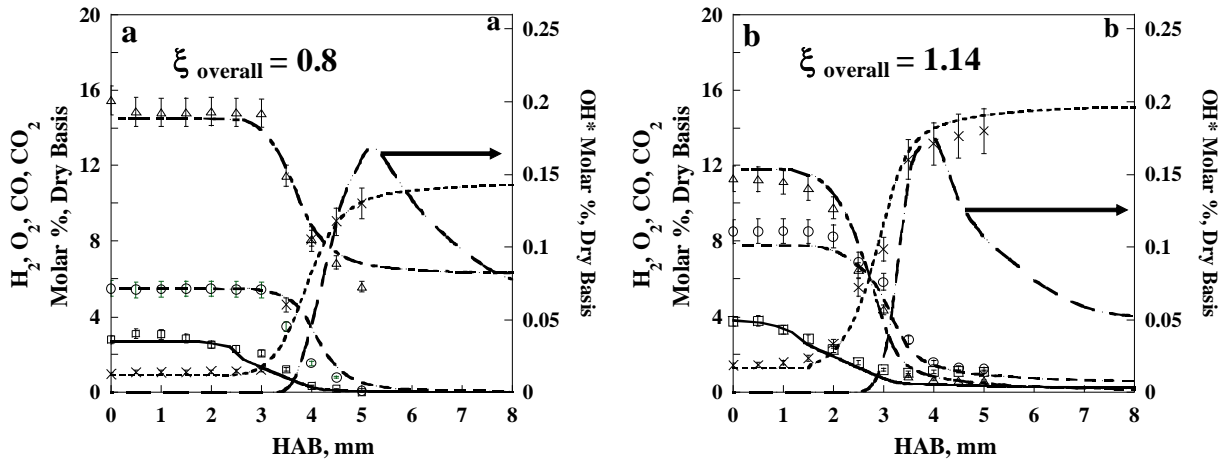


Figure 31. Experimental measurements versus model predictions of H<sub>2</sub> (□ data, — model), O<sub>2</sub> (△ data, - - - model), CO (○ data, - - - model), CO<sub>2</sub> (x data, ---- model) and OH\* (.- — model) for (a)  $\Phi_{\text{overall}} = 0.8$  and (b)  $\Phi_{\text{overall}} = 1.14$ . Error bars represent the experimental uncertainty.

The results for the experimental  $W$  calculated using Equation (41) are presented in Figure 32 for  $\Phi_{\text{overall}} = 0.8$  and 1.14. For  $\Phi_{\text{overall}} = 0.8$ , rates were found to be relatively low and constant close to the burner surface, increasing in the upper (HAB > 2.5 mm) region of the flame. For the rich flame ( $\Phi_{\text{overall}} = 1.14$ ), rates increased faster close to the burner surface and reached a maximum of  $7.8 \times 10^{-4}$  g/cm<sup>2</sup>-sec before starting to decrease. This behavior was consistent with the trend of the PSDs (Figure 29), and O<sub>2</sub> and OH\* (see Figure 31) concentrations profiles where small changes took place up to 1.5 -2 mm.

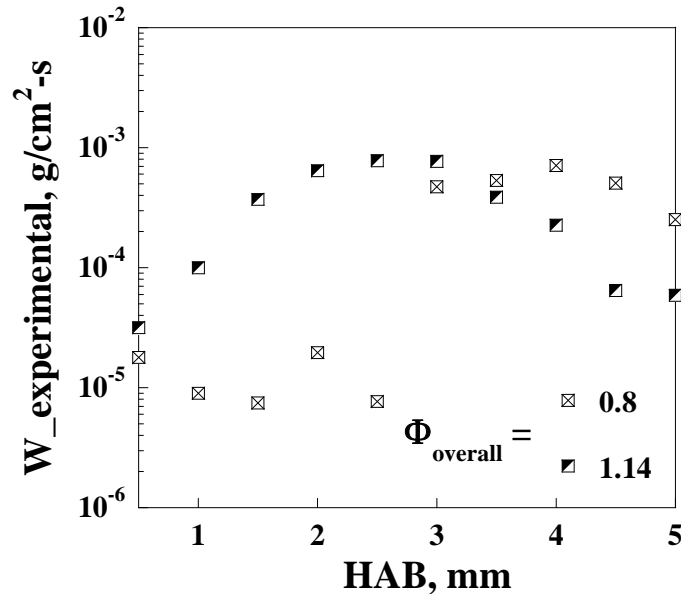


Figure 32. Experimental soot oxidation rates ( $W$ ) calculated from the evolution of PSD for  $\Phi_{\text{overall}} = 0.8$  and 1.14.

Soot generated in the first burner in a ethylene/air flame was oxidized not only for the conditions presented above ( $\Phi_{\text{overall}} = 0.8$  and 1.14) but for intermediate conditions that allowed further study of the effect of temperature and equivalence ratio on soot oxidation. Similarly to the previous data, temperature, PSDs, number and mass concentration, gas-phase compounds and soot oxidation rates were characterized in the two-stage burner as a function of the HAB for  $\Phi_{\text{overall}} = 0.87, 0.94,$  and 1.07.

Figure 33 illustrates the temperature profile for these experimental conditions measured within the second burner up to 5 mm. Temperature profiles showed a typical behavior of the evolution of peak temperature with equivalence ratio. Peak temperature for the lean flames increased from the leanest conditions 0.8 (see Figure 28) to 0.94 (Figure 33). On the other hand, temperature decreased in the rich side from  $\Phi_{\text{overall}} = 1.07$  to 1.14. Once again, these temperature profiles were used as inputs into the detailed kinetic model to obtain the concentration of  $\text{OH}^*$  as a function of the HAB.

Figures 34a, 34b and 34c present the results for the evolution of the soot size within the flame from 0 to 5 mm for  $\Phi_{\text{overall}} = 0.87, 0.94$  and 1.07 respectively. These PSDs were integrated in size intervals of less than and greater than 10 nm to characterize the number and mass concentrations in the ultrafine (3-10 nm) and fine (> 10 nm-160) modes (Figure 35a, b, c and d for  $\Phi_{\text{overall}} = 0.87, 0.94$  and Figure 35e and f for  $\Phi_{\text{overall}} = 1.07$ ). Fragmentation, to a smaller extent, was only observed to occur for the 0.87 flame. However, it seemed to disappear for the 0.94 and 1.07 flames where soot burnout dominated the oxidation process. These results were reflected in terms of number and mass concentration in both the ultrafine and fine modes (Figure 35). Number and mass concentration increased close to the burner surface (HAB < 1.5 mm) for  $\Phi_{\text{overall}} = 0.87$  in the ultrafine mode, while higher in the burner, both number and mass

concentration showed a continuous decrease, and started to level after 6 mm. In the fine mode, close to the burner surface (HAB < 1.5 mm), a slight decrease in mass was observed which was consistent with the increase in mass in the ultrafine mode. Higher in the burner, the soot burnout process dominated in both the ultrafine and fine modes. For equivalence ratios of 0.94 and 1.07 (Figure 35c, d, e and f), both the ultrafine and fine modes showed major changes in mass and number concentration after 1.5 mm where the rate of oxidation increased significantly (see Figure 35a), probably as a result of increased surface area with the smaller particles or other resulting structural changes.

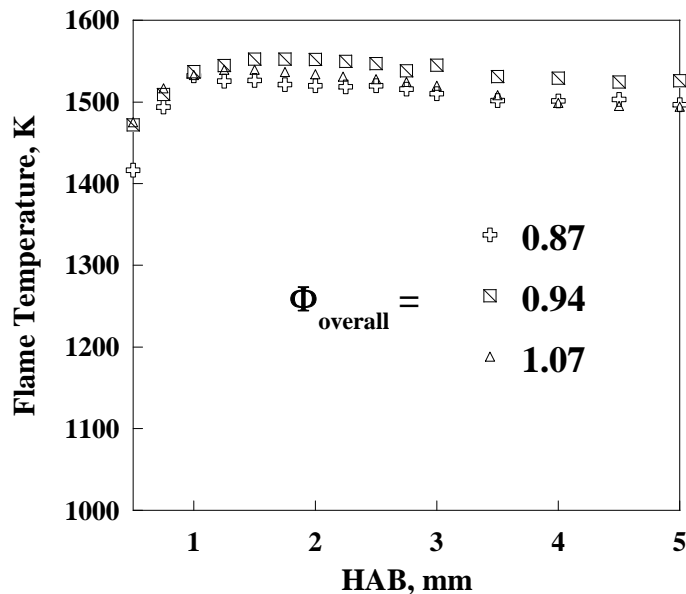


Figure 33. Top burner temperature profiles as a function of HAB for  $\Phi_{\text{overall}} = 0.87, 0.94$  and  $1.07$ . Thermocouple uncertainty  $\pm 50\text{K}$

In terms of the gas-phase compositions (Figure 36), the evolution of the species such as  $\text{H}_2$ ,  $\text{O}_2$ ,  $\text{CO}$ ,  $\text{CO}_2$  and  $\text{OH}^*$  was similar to the results presented for  $\Phi_{\text{overall}} = 0.8$ , and  $1.14$ . Once again, it should be highlighted the earlier formation of the  $\text{OH}^*$  in the rich flame ( $1.07$ ), which promoted the burnout process instead of fragmentation. Although fragmentation may be taking place close to the burner surface, the higher reactivity of the  $\text{OH}^*$  favors the faster consumption of the soot particles.

Soot oxidation rates ( $W$ ) (see Figure 37) were also calculated from the evolution of PSDs. For  $\Phi_{\text{overall}} = 0.87, 0.94$ , and  $1.07$  rates were higher closer to the burner surface relative to the  $W$ s estimated for the leanest flame ( $\Phi_{\text{overall}} = 0.8$ ) (see Figure 32). The little or no fragmentation found in the flames  $0.87, 0.94$  and  $1.07$  can be supported for the observed increase in soot oxidation rates and the relatively high concentration of  $\text{OH}^*$  higher in the burner. As mentioned before, the higher reactivity of the  $\text{OH}^*$  promoted the earlier consumption of particles which was reflected in terms of the evolution of PSDs, number and mass concentration within the flames.

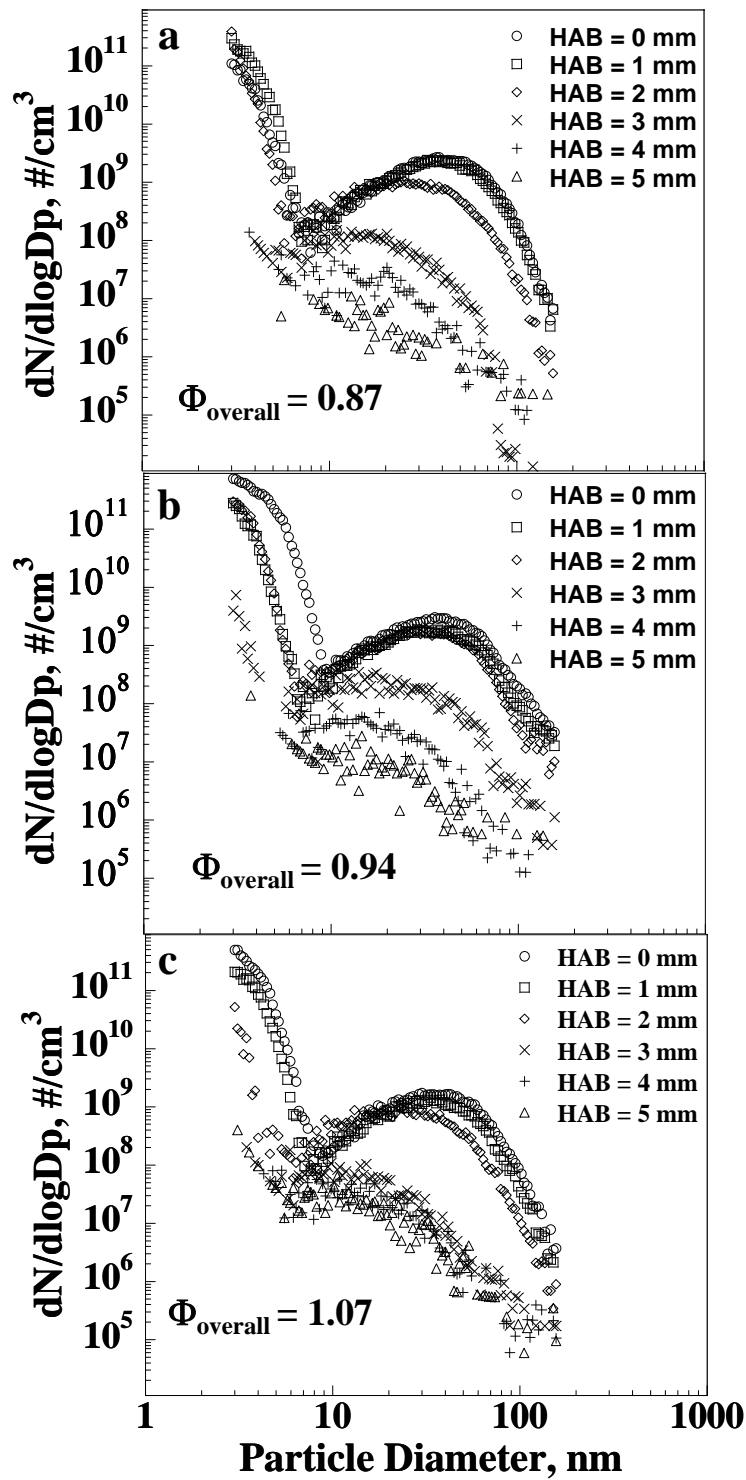


Figure 34. Experimental PSDs measured as a function of the height above the top burner for (a)  $\Phi_{\text{overall}} = 0.87$ , (b)  $\Phi_{\text{overall}} = 0.94$  and (c)  $\Phi_{\text{overall}} = 1.07$ .

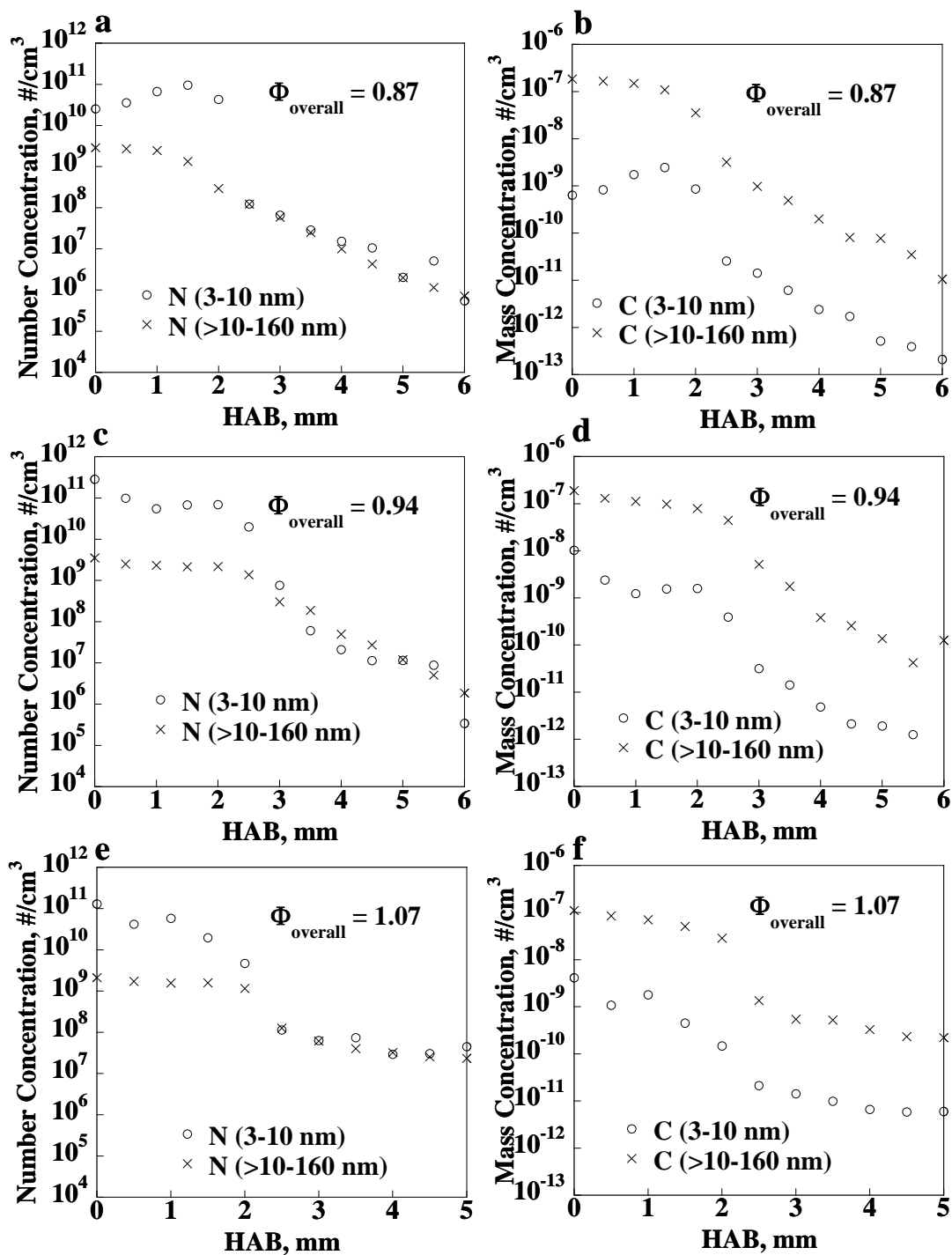


Figure 35. Integrated number and mass concentrations for fuel lean and fuel rich flames. (a) and (b) number and mass concentration for the ultrafine and fine modes ( $\Phi_{\text{overall}} = 0.87$ ). (c) and (d) number and mass concentration for the ultrafine and fine modes ( $\Phi_{\text{overall}} = 0.94$ ). (e) and (f) number and mass concentration for the ultrafine and fine modes ( $\Phi_{\text{overall}} = 1.07$ ).

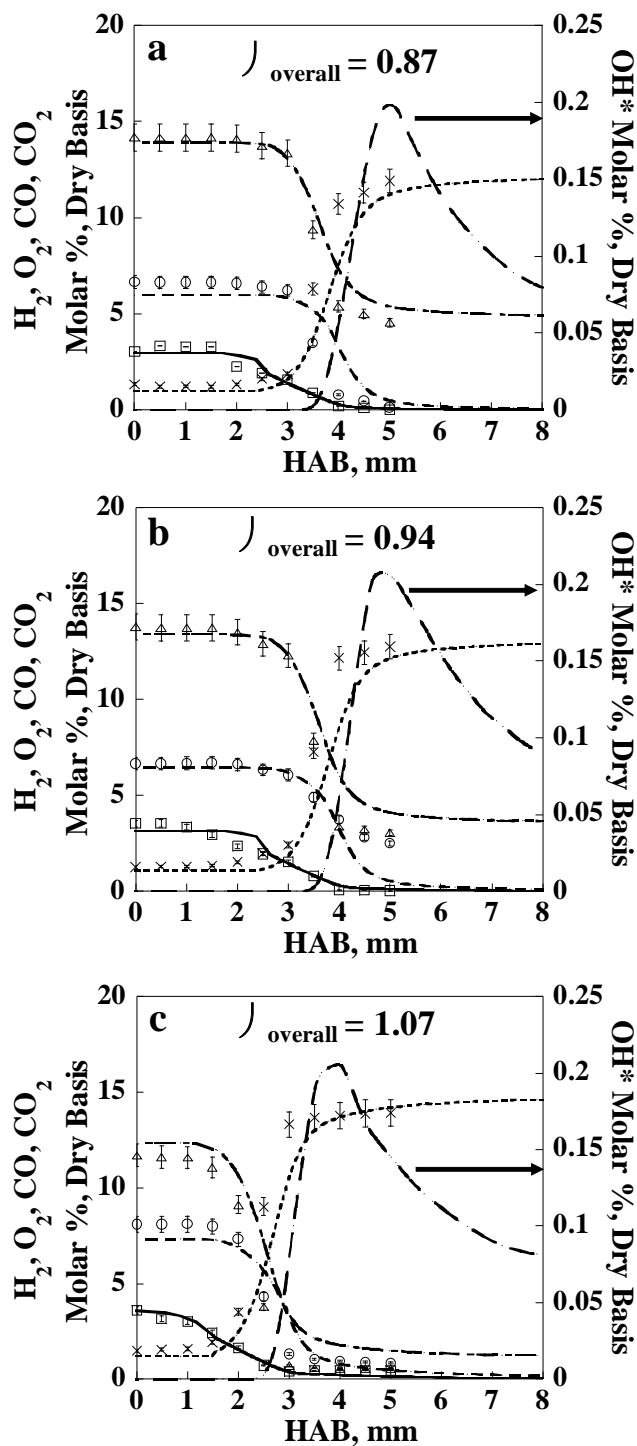


Figure 36. Experimental measurements (open symbols) versus model predictions of  $H_2$  ( $\square$ , data, — model),  $O_2$  ( $\Delta$  data, - - - model),  $CO$  ( $\circ$  data, - - - model),  $CO_2$  ( $\times$  data, ---- model) and  $OH^*$  (.- — model) for (a)  $\Phi_{\text{overall}} = 0.87$ , (b)  $\Phi_{\text{overall}} = 0.94$  and (c)  $\Phi_{\text{overall}} = 1.07$ . Error bars represent the experimental uncertainty.

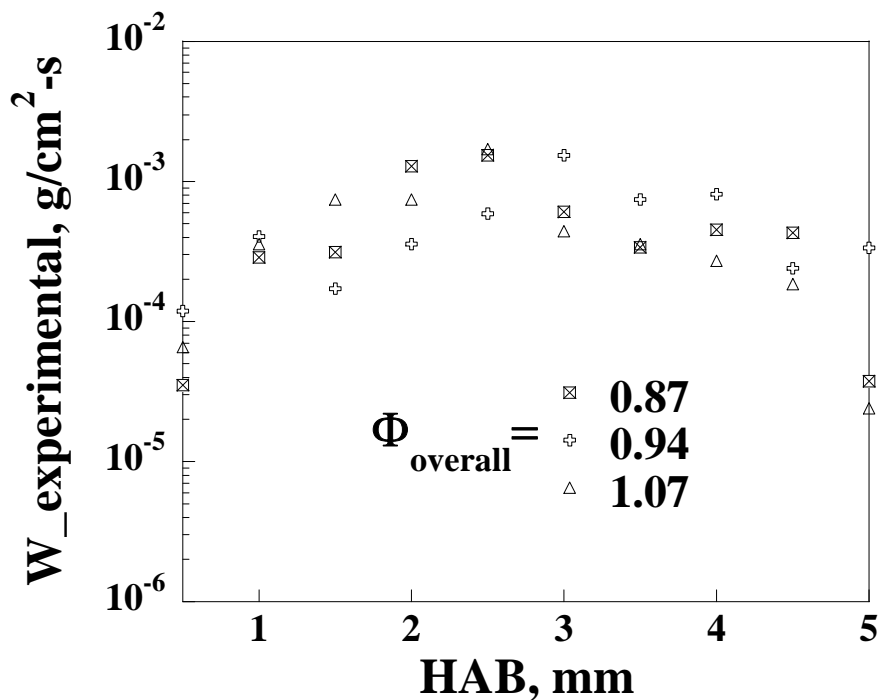


Figure 37. Experimental soot oxidation rates (W) calculated from the evolution of PSD as a function of the HAB for  $\Phi_{overall} = 0.87, 0.94$  and  $1.07$ .

### Surrogate/Air, m-Xylene/Air and n-Dodecane/Air Flames

The use of surrogate/air, m-xylene/air and n-dodecane/air flames constituted our transition from simple fuels, i.e., ethylene, to more practical liquid fuels. Preliminary studies with a mixture 23/77 vol. % were difficult to perform due to the high sooting tendency of the 23/77 mixture. Studies on soot oxidation were also carried out for the pure components of the surrogate mixture m-xylene and n-dodecane.

The oxidation burner was initially characterized in terms of temperature under lean ( $\Phi_{overall} = 0.8$ ) and rich ( $\Phi_{overall} = 1.14$ ) conditions. Flame temperature profiles measured in the top burner for conditions where soot was derived from m-xylene/air, surrogate/air, and n-dodecane/air flames are presented in Figures 38a,b and c, respectively. Temperature profiles for the six flames showed a similar behavior, increasing rapidly close to the burner surface until a peak temperature was reached. Downstream, they leveled off and remained relatively constant up to 7 mm, which is the maximum distance above the second burner surface where experimental measurements were taken. Temperature profiles and experimental conditions at the top burner surface were used as inputs into CHEMKIN 4.1 to model the evolution of major gas-phase species ( $H_2, O_2, CO, CO_2, OH^*$ ).

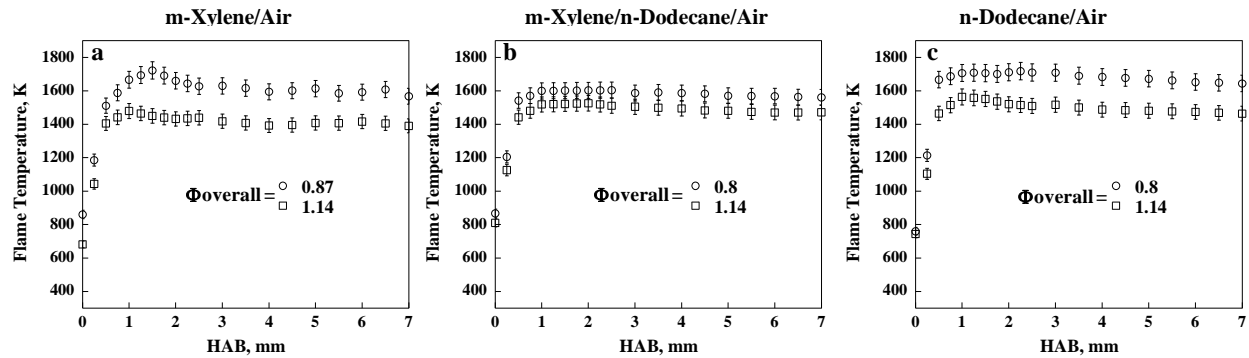


Figure 38. Top burner temperature profiles as a function of HAB under lean and rich conditions. Soot in the top burner was derived from: (a) m-xylene/air flame, (b) surrogate/air and (c) n-dodecane/air flames. Error bars represent thermocouple uncertainty ( $\pm 50\text{K}$ )

The oxidation process of soot particles formed in the bottom burner was mainly followed by measuring the evolution of particle size distribution (PSD) and number concentration as a function of the HAB. Figure 39a (0 to 3.5 mm) and Figure 39b (4 to 7 mm) illustrates the results for the lean ( $\Phi_{\text{overall}} = 0.8$ ) surrogate/air flame where the most significant changes in terms of PSD took place. At the top burner surface (HAB = 0 mm), the PSD was unimodal and most of the distribution was dominated by the fine mode (particle diameter  $> 10$  nm). In this flame, the PSD evolved from a unimodal to bimodal distribution with the smaller nanoparticles corresponding to the ultrafine mode (particle diameter  $< 10$  nm). The presence of these nanoparticles in the ultrafine mode was mainly associated with the fragmentation of the bigger particles at low burnout ( $\sim 15\%$ ). As mentioned before, previous studies (Neoh, 1981; Merrill, 2005; Lighty, 2008; Echavarria, 2011) have attributed this behavior to  $\text{O}_2$  penetrating the soot nanostructure, which in turn, caused internal burning and led to the fracture and breakup of the particles. In the upper regions of the flame (HAB  $> 3.5$  mm, Figure 39b), number concentration decreased in both the ultrafine and fine mode, and at 6.5 mm above burner surface most of the particles were burned out. On the other hand, the series of oxidation experiments performed on soot derived from the surrogate flame under rich ( $\Phi_{\text{overall}} = 1.14$ , Figures 39c and 39d) conditions also showed the presence of particle fragmentation, a characteristic that was not observed in previous studies when soot derived from methane/air (Neoh, 1981) or ethylene/air (Echavarria et al., 2011) flames was oxidized under slightly rich conditions.

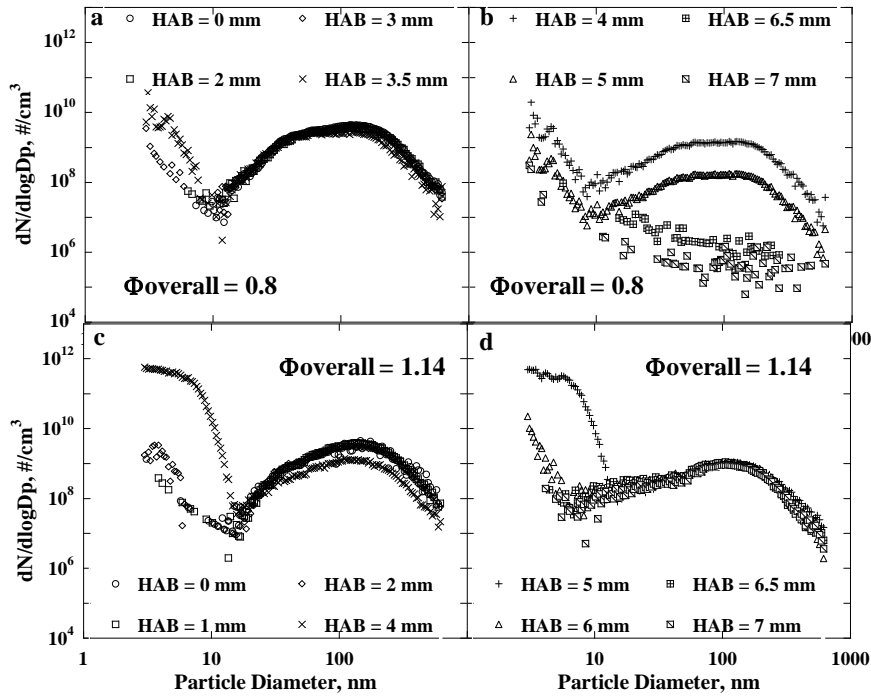


Figure 39. Evolution of PSD in the top burner in the surrogate/air flame for (a)  $\Phi_{\text{Overall}} = 0.8$  and HAB from 0 to 3.5 mm, (b)  $\Phi_{\text{Overall}} = 0.8$  and HAB from 4 to 7 mm, (c)  $\Phi_{\text{Overall}} = 1.14$  and HAB from 0 to 4 mm and (d)  $\Phi_{\text{Overall}} = 1.14$  and HAB from 5 to 7 mm

Results in terms of the evolution of soot size distribution in the top burner under lean and slightly rich conditions for soot derived from rich flames of the pure components of the surrogate mixture are presented in Figures 40a through 40g. Fragmentation occurred in all the cases as reflected for the presence of nanoparticles in the ultrafine mode after a characteristic initial induction period between 1 to 2 mm. Higher in the burner most of the particles were burnout under fuel lean conditions and the concentration of the fine sized particles remains relatively high for rich conditions.

These results were more clearly seen when the PSDs were integrated in size intervals of less than and greater than 10 nm to provide measures of the change in number concentration in the ultrafine and fine modes as a function of the HAB (Figures 41a and b, lean and rich ultrafine mode and 41c and d lean and rich fine mode). Figures 41a and b clearly shows the drastic increase of nanoparticles in the ultrafine mode close to the burner surface for lean and rich conditions, while higher in the burner, number concentration in both the ultrafine and fine modes (Figures 41c and d) showed a continuous decrease, particularly for the lean flames. For the rich flames (Figure 41b), it is clear that the extent of fragmentation, which is characterized by the increase of nanoparticles in the ultrafine mode, was higher relative to lean (Figure 41a) conditions, and it lasted over almost the entire range of HABs evaluated. The decrease of nanoparticles in the fine mode under the rich condition was also observed to be considerably lower relative to lean flame (Figure 41c and d). In addition, the figures show that the surrogate does not appear to burnout as quickly as the pure components, especially in the lean case.

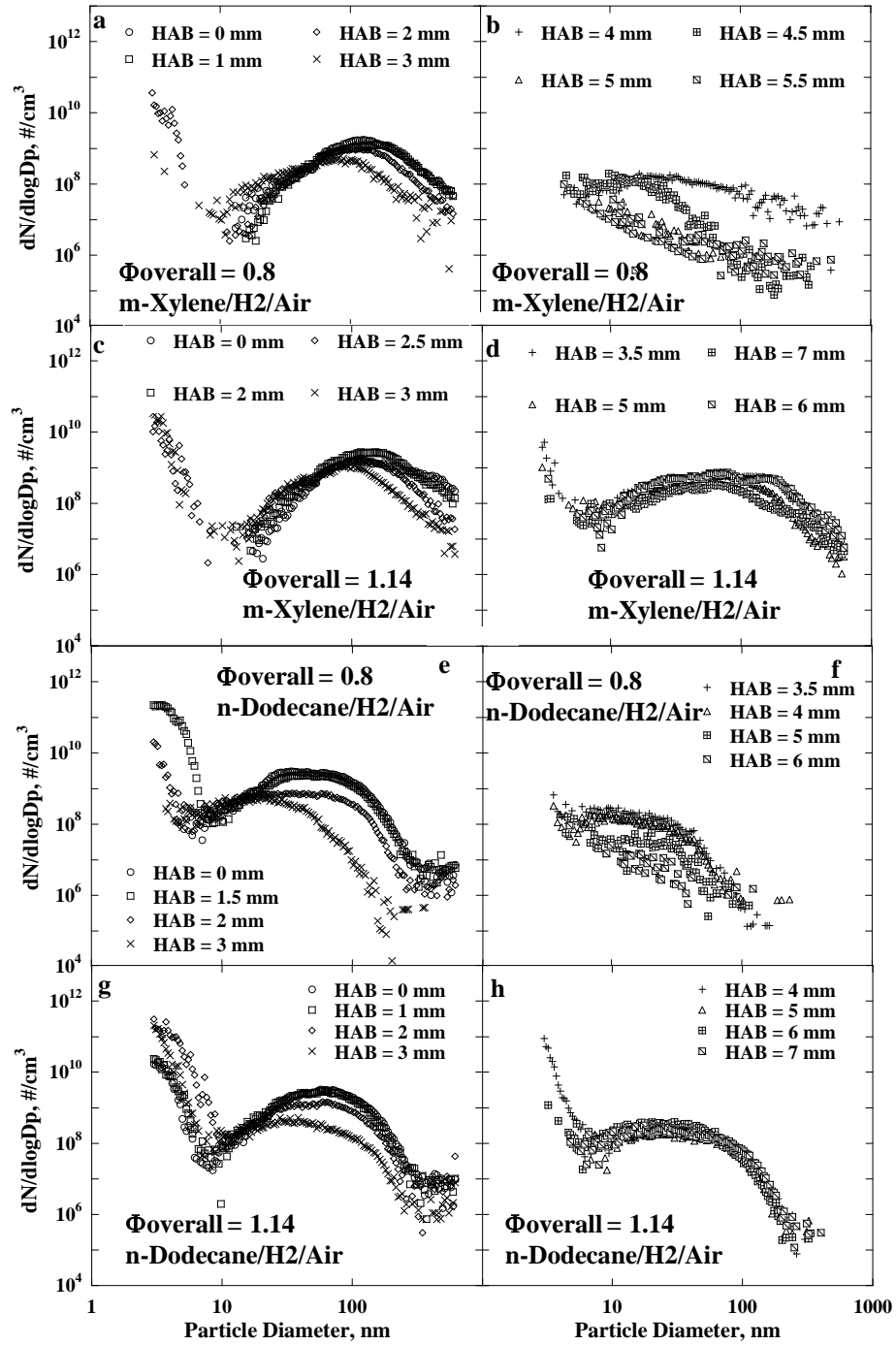


Figure 40. Evolution of PSD in the top burner in the systems m-xylene/H<sub>2</sub>/air and n-dodecane/H<sub>2</sub>/air for (a) m-x/H<sub>2</sub>/air,  $\Phi_{\text{Overall}} = 0.8$  and HAB from 0 to 3 mm, (b) m-x/H<sub>2</sub>/air,  $\Phi_{\text{Overall}} = 0.8$  and HAB from 4 to 5.5 mm, (c) m-x/H<sub>2</sub>/air,  $\Phi_{\text{Overall}} = 1.14$  and HAB from 0 to 3 mm, (d) m-x/H<sub>2</sub>/air,  $\Phi_{\text{Overall}} = 1.14$  and HAB from 3.5 to 6 mm, (e) n-d/H<sub>2</sub>/air,  $\Phi_{\text{Overall}} = 0.8$  and HAB from 0 to 3 mm, (f) n-d/H<sub>2</sub>/air,  $\Phi_{\text{Overall}} = 0.8$  and HAB from 3.5 to 6 mm, (g) n-d/H<sub>2</sub>/air,  $\Phi_{\text{Overall}} = 1.14$  and HAB from 0 to 3 mm, (h) n-d/H<sub>2</sub>/air,  $\Phi_{\text{Overall}} = 1.14$  and HAB from 4 to 7 mm.

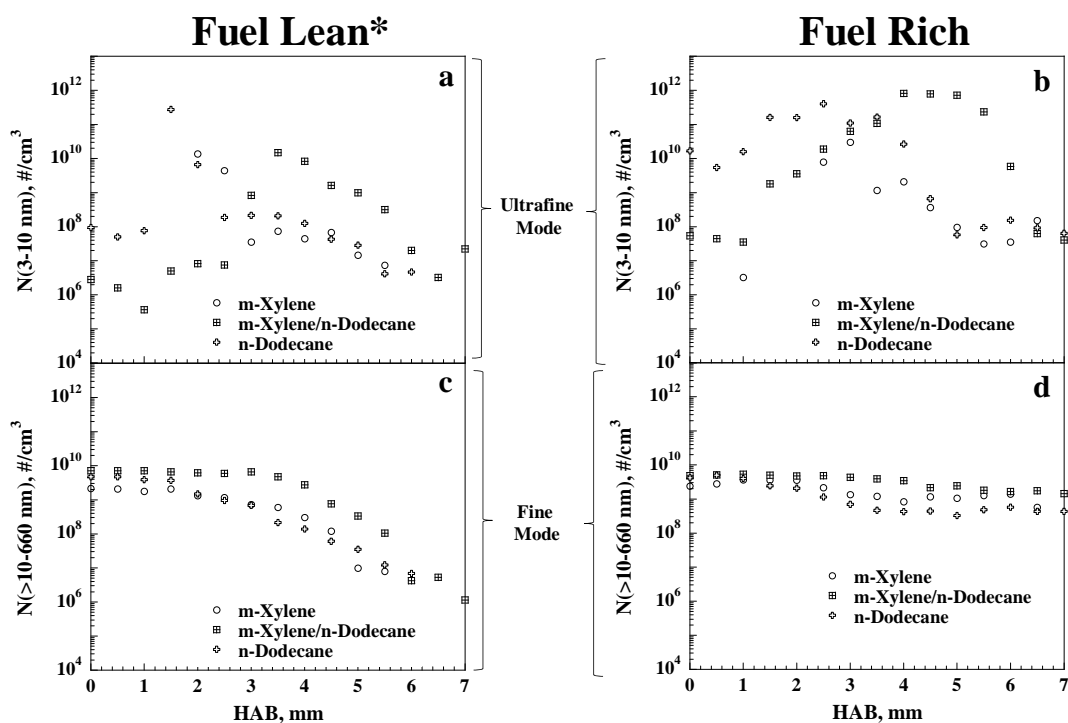


Figure 41. Number concentration measurements in the ultrafine (3-10nm) and fine (>10nm) modes calculated from the PSD for m-xylene, surrogate, and n-dodecane flames under fuel lean and fuel rich condition. (a)  $\Phi_{\text{Overall}} = 0.8$ , ultrafine mode, (b)  $\Phi_{\text{Overall}} = 1.14$ , ultrafine mode, (c)  $\Phi_{\text{Overall}} = 0.8$ , fine mode and (d)  $\Phi_{\text{Overall}} = 1.14$ , fine mode. \*  $\Phi_{\text{Overall}}$  under fuel lean conditions for the system with m-xylene/H<sub>2</sub>/air is equal to 0.87.

The mole fractions of gas-phase species were measured using online GC analysis. OH\* was calculated by CHEMKIN 4.1 software as previously discussed. However, in this case a validated JP-8 mechanism developed by Zhang et al. (2005) was used to predict the exit stream from the first burner. The results showed that the most important species that mixed with the secondary air were H<sub>2</sub>, CO, CO<sub>2</sub>, H<sub>2</sub>O, and soot. The second burner was modeled using a detailed kinetic model developed by D'Anna et al. (2006, 2008) that includes reaction paths for the oxidation of H<sub>2</sub>, CO and the formation/oxidation of soot in flames. Experimental measurements of gas flow rates, concentration of gas-phase species (H<sub>2</sub>, CO, CO<sub>2</sub>, H<sub>2</sub>O, O<sub>2</sub>, soot) at the burner surface and the temperature profile were used in the simulation of the top burner. Figures 42a through 42i present the measured and predicted profiles of H<sub>2</sub>, CO, CO<sub>2</sub>, O<sub>2</sub> and OH\* within the top burner for lean ( $\Phi_{\text{Overall}} = 0.8, 0.87$ ) and rich ( $\Phi_{\text{Overall}} = 1.14$ ) conditions in the surrogate/air (Figure 42a, b and c), m-xylene/air (Figure 42d, e and f) and n-dodecane/air (Figure 42g, h and i) systems. Model results were shifted downstream to account for sampling probe effects (Zhao et al., 2003, Echavarria et al., 2009). Among the main observations, in the surrogate mixture system (Figures 42a, lean and 42b, rich) the concentration profiles of H<sub>2</sub>, CO, CO<sub>2</sub> and particularly O<sub>2</sub> showed a major change after an induction period up to 3 mm and 4 mm for lean and rich flames respectively. This behavior was consistent with the regions where the most significant changes in terms of size and number concentration in both flames were observed.

The high temperature environment and the relatively high concentration of  $O_2$  in that region favored the fragmentation of soot particles for the lean flame. It is also important to note that for the rich condition, a more prolonged induction period took place, which in turn, favored the higher extent of fragmentation under this condition. Figure 42c shows the calculated concentration profiles of  $OH^*$  radicals within the top burner for the same system. The evolution of these species was similar for both lean and rich flames. The concentration of  $OH^*$  had a major impact in the upper regions of the flames where it contributed mostly to the burnout of particles, in particular for the lean condition where the concentration of  $OH^*$  was relatively higher. The major drop of particle concentration in the upper regions of the flames (see Figure 41) was attributed to the higher intrinsic reactivity of  $OH^*$  compared to  $O_2$  (Neoh, 1981). For the other two systems where soot was derived from m-xylene/air (Figures 42d through 42f) and n-dodecane/air (Figures 42g through i) flames, the evolution of major gas-phase species, particularly the changes in  $O_2$  and  $OH^*$  showed a similar behavior.  $O_2$  and  $OH^*$  changed in the region where the most significant changes in terms of PSD and number concentration took place.  $O_2$  was predominant on soot oxidation close to the burner surface and  $OH^*$  in the upper regions of the flames. In addition, the reduced amount of  $OH^*$  predicted in the upper regions of the flame could account for the reduced rate of fine particle decrease for the surrogate as compared to m-xylene and dodecane.

Soot oxidation rates ( $W$ ) were calculated from the evolution of PSDs using Equation 41(see Figure 43). For lean and rich conditions, the rates were relatively higher than the soot oxidation rates calculated for ethylene/air flames. However they are still lower closer to the burner surface and showed a continue increase with HAB. The higher soot oxidation rates obtained upper in the burner were associated to the higher reactivity of the  $OH^*$  Neoh et al. 1981) that promoted the consumption of particles higher in the burner for lean and rich conditions.

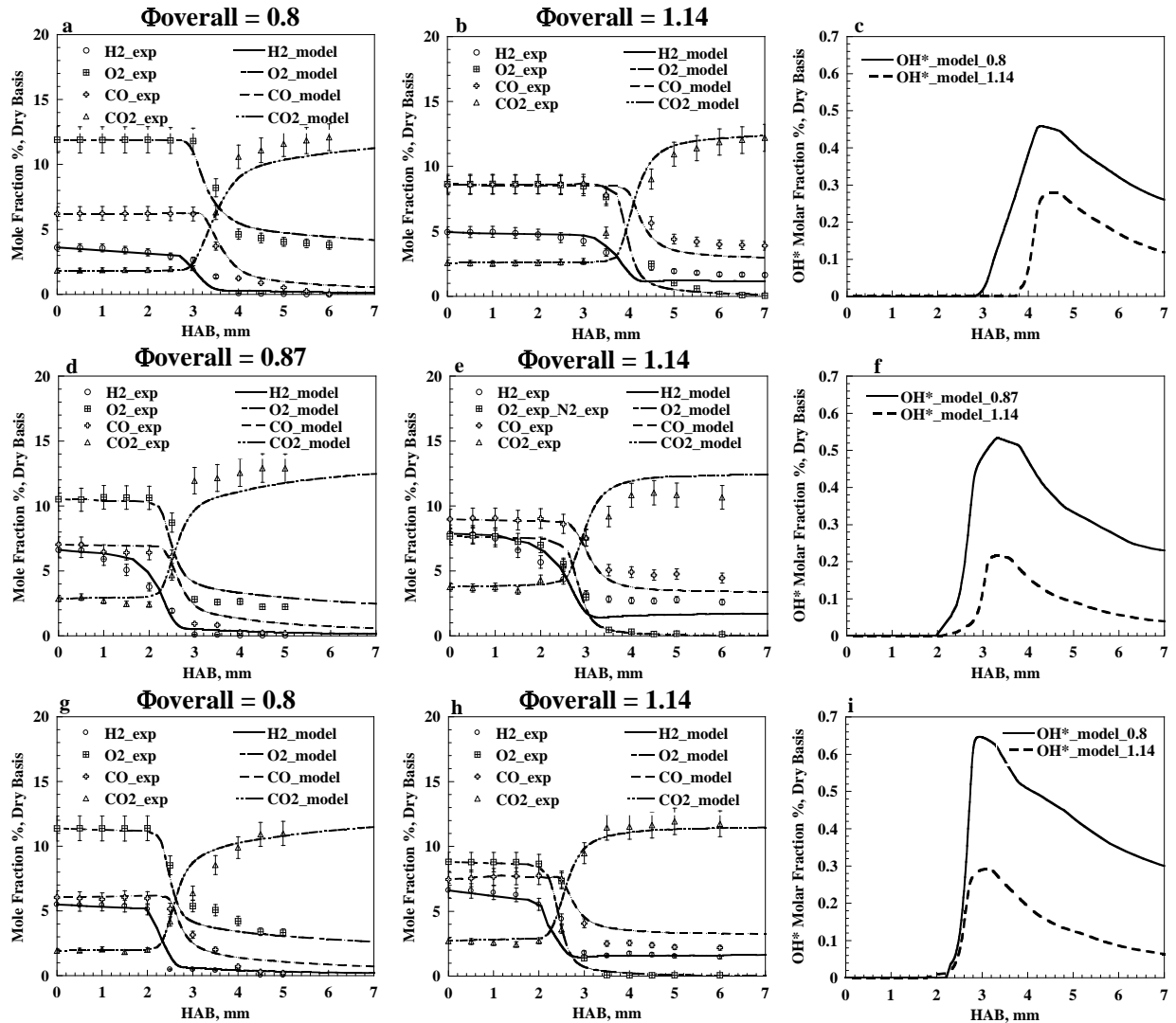


Figure 42. Evolution of major gas phase species for the surrogate mixture and the surrogate components within the second burner. Symbols correspond to experimental results and solid and dashed lines to model predictions (a) H<sub>2</sub>, O<sub>2</sub>, CO and CO<sub>2</sub> for surrogate, (b) H<sub>2</sub>, O<sub>2</sub>, CO and CO<sub>2</sub> for surrogate, (c) OH\* predictions, surrogate,  $\Phi_{\text{Overall}} = 0.8$  and 1.14; (d) H<sub>2</sub>, O<sub>2</sub>, CO and CO<sub>2</sub> for m-xylene, (e) H<sub>2</sub>, O<sub>2</sub>, CO and CO<sub>2</sub> for m-xylene, (f) OH\* predictions, m-xylene,  $\Phi_{\text{Overall}} = 0.87$  and 1.14; (g) H<sub>2</sub>, O<sub>2</sub>, CO and CO<sub>2</sub> for n-dodecane, (h) H<sub>2</sub>, O<sub>2</sub>, CO and CO<sub>2</sub> for n-dodecane, (i) OH\* predictions, n-dodecane,  $\Phi_{\text{Overall}} = 0.8$  and 1.14. Error bars represent experimental uncertainty

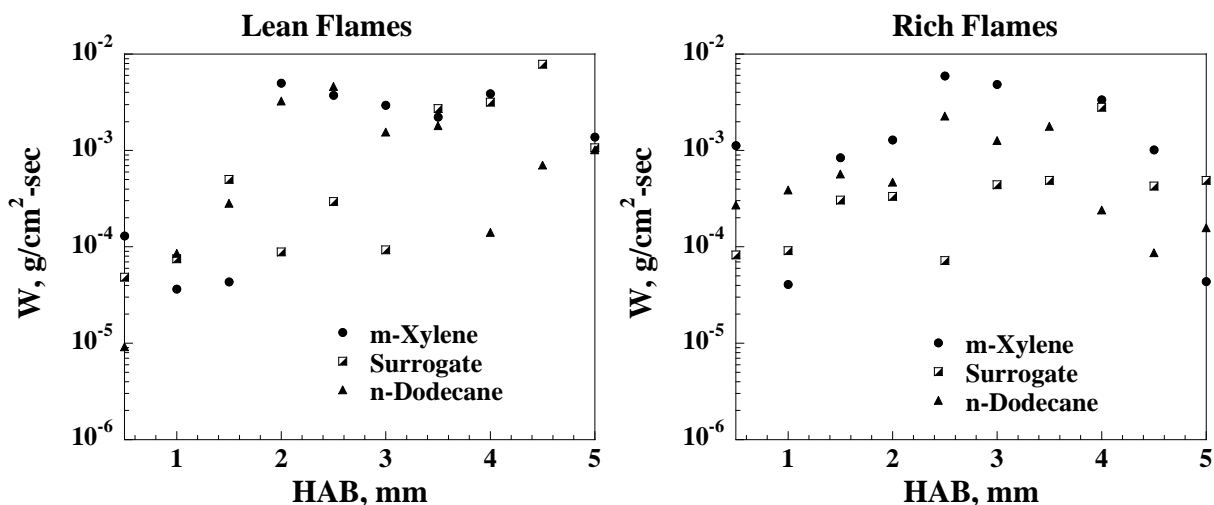


Figure 43. Experimental soot oxidation rates ( $W$ ) calculated from the evolution of PSD as a function of the HAB under lean ( $\phi=0.8$ ) and rich ( $\phi=1.14$ ) conditions.

#### Development of kinetics for soot oxidation and comparisons

Experimental soot oxidation rates estimated from SMPS measurements and presented in Figures 32, 37 (for ethylene/air) and 43 (for the surrogate mixture and its pure components) were compared to previously-mentioned models used in the literature to account for soot oxidation via  $O_2$  (NSC, Equation 2) and soot oxidation via  $OH^*$  (Neoh, Equation 1). The data are presented with the temperature profiles corrected for probe effects and  $O_2$  and  $OH^*$  concentrations corresponding to these temperatures. Each is shown separately but the entire oxidation is the addition of the two effects. The results under lean and rich overall conditions are presented in Figures 44a through 44h for the combustion systems where soot was derived from ethylene/air (Figures 44a and 44b), surrogate/air (Figures 44c and 44d), m-xylene/air (44e and 44f) and n-dodecane/air (Figures 44g and 44h) premixed flames.

Figure 44 shows that under the experimental conditions used in this work, the NSC equation under-predicted the set of experimental data in the region where soot oxidation via  $O_2$  became predominant as evidenced by the gas-phase analysis (see Figures 31 and 42) for the lean cases. In the fuel-rich cases, the predictions were much lower. Neoh's kinetic equation to account for soot oxidation via  $OH^*$  produced a relatively good fit higher in the burner, which confirmed that the most significant contribution of  $OH^*$  radical to soot burnout was in that region. It should be noted that the error in temperature is likely the highest uncertainty and HAB could be  $\pm 1$  mm. Under lean conditions, oxidation via  $O_2$  is also occurring in the upper regions of the flame; however, as expected, because of the higher intrinsic reactivity of  $OH^*$  with soot (Neoh, 1981), oxidation via  $O_2$  had a minimum impact in the upper regions of the flame. Soot oxidation via  $O_2$  contributed mainly to soot fragmentation in the regions close to the burner surface and higher in the top burner for the lean oxidation flames.

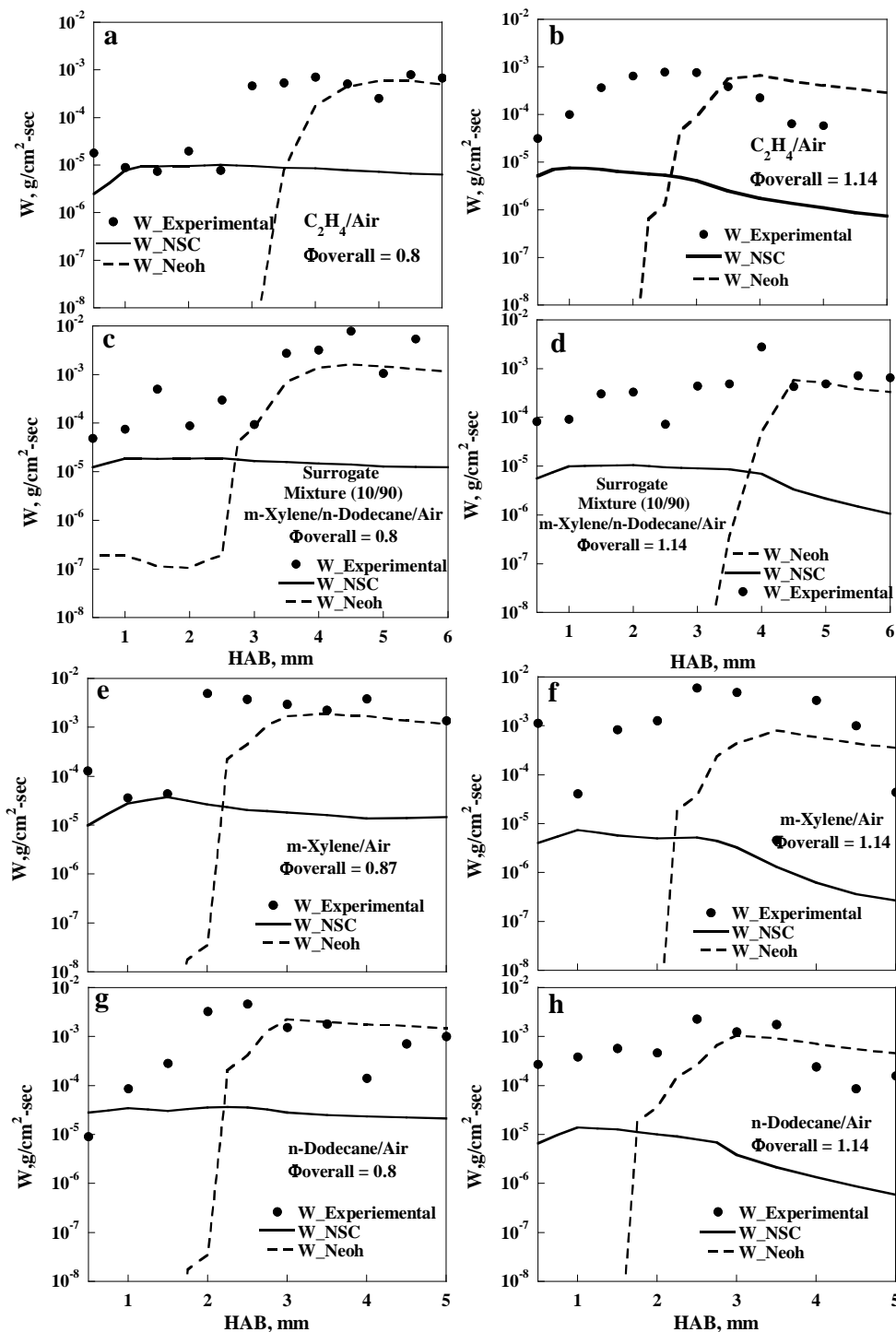


Figure 44. Experimental versus models prediction using NSC and Neoh's kinetic oxidation equation for the set of flames ran under lean and slightly rich conditions. (a) and (b) ethylene/air; (c) and (d) surrogate/air; (e) and (f) m-xylene/air and (g) and (h) n-dodecane/air.

### Comprehensive Soot Oxidation Expression

Neoh's (1981) kinetic expression to account for soot oxidation via OH\* has been used extensively in the literature and in this work as well. The results presented in the previous section showed that this expression was suitable to account for the oxidation of particles derived from different sources under fuel lean and slightly rich conditions when oxidation via OH\* was dominant. A kinetic expression that includes the effect of temperature, O<sub>2</sub> and OH\* concentration to calculate the oxidation rate of soot particles derived from ethylene/air, surrogate/air, m-xylene/air, and n-dodecane/air flames is proposed in this work where:

$$W_{total} (g / cm^2 - sec) = 1.29 \times 10^2 \frac{\Gamma_{OH}}{\sqrt{T}} P_{OH^*} + W_{O_2} \quad (42)$$

$$W_{O_2} = k_{O_2} * P_{O_2}^n \quad (43)$$

$k_{O_2}$  is the intrinsic reaction rate and  $P_{O_2}$  is the partial pressure in atm.  $k_{O_2}$  can be expressed as:

$$k_{O_2} = A * T^{0.5} \exp\left[-\frac{Ea}{RT}\right] \quad (44)$$

where  $A$  is the pre-exponential factor,  $Ea$  is the activation energy,  $R$  is the gas constant, and  $T$  is the reaction temperature. Equations 43 and 44 were solved numerically in Polymath for conditions where oxidation via O<sub>2</sub> dominated close to the burner surface (ethylene/air,  $\Phi_{overall}=0.8$ ; surrogate/air,  $\Phi_{overall} = 0.8, 1.14$ ; m-xylene/air,  $\Phi_{overall} = 0.87, 1.14$ ; n-dodecane/air,  $\Phi_{overall} = 0.8, 1.14$ ). The parameters  $A$ ,  $n$  and  $Ea$  that best fitted the experimental  $W_s$  for each condition are presented in Table 5.

Table 5. Kinetic parameters that produced best fitting for the experimental data.

System	A	Ea, kJ/mol	n
Ethy_0.8	0.985	161.50	0.75
Surrogate_0.8	1.101	140.37	0.73
Surrogate_1.14	1.101	126.61	0.70
m_Xylene_0.87	1.101	158.38	0.77
m_Xylene_1.14	1.101	105.43	0.74
n-Dodecane_0.8	1.101	126.96	0.76
n-Dodecane_1.14	1.200	100.40	0.76
<u>Average</u>	<u>1.099</u>	<u>131.38</u>	<u>0.74</u>

The averaged values presented in Table 5 were used to express the overall soot oxidation rate as follows:

$$W_{total} (g / cm^2 - sec) = 1.29 \times 10^2 \frac{\Gamma_{OH}}{\sqrt{T}} P_{OH^*} + 1.099 * T^{0.5} \exp\left[-\frac{131.4(kJ/mol)}{R * T}\right] * (P_{O_2})^{0.74} \quad (45)$$

This expression applies for equivalence ratios ranging from 0.8 to 1.14,  $O_2$  partial pressures from 0.065 to 0.123 atm, and peak temperatures from 1450-1750 K for soot oxidation from ethylene/air, surrogate/air, m-xylene/air, and n-dodecane/air flames. Comparisons of predictions using Equation 45 with experimental data are presented in Figures 45a through 45g for ethylene/air (Figures 45a), surrogate/air (Figures 45b and 45c), m-xylene/air (45d and 45e) and n-dodecane/air (Figures 45f and 45g) premixed flames. Once again, the effect of the sampling probe was accounted for. It is also interesting to note that the activation energy is approximately that for the NSC equation's A sites (see Table 2) which is 30 kcal/mole or approximately 125 kJ/mole. The rate is still low as a result of different in the pre-exponential factor, although the pre-exponential is a function of surface area. As previously discussed, an increase in surface area might account for these differences. These results also suggest that the studies were in the regime of temperatures and lower reactivity sites.

Results in Figure 45 showed a good agreement between experimental soot oxidation rates determined from SMPS measurements and predictions using the proposed Equation 45 which accounted simultaneously for the effect of temperature,  $O_2$  and  $OH^*$  concentration on the soot oxidation derived from different sources in premixed combustion systems. The proposed equation is able to capture the major features of the experimental results, particularly the major contribution of  $O_2$  to soot oxidation in the region close to the burner surface and  $OH^*$  higher in the burner. In comparison with the literature (i.e. Nienow, et al. 2005), the activation energy is within the range of others as is the order in oxygen. Literature values tend toward 100-150 kcal/mol with an order of approximately 0.7 in oxygen.

### **Changes in Soot Morphology and Nanostructure During Soot Oxidation**

Preliminary TEM and HR-TEM analysis of soot samples collected thermophoretically in the top burner as a function of the height above the burner for ethylene/air flame under a lean condition were carried out to compare with the SMPS data and obtain insights into the changes on soot morphology and nanostructure during soot oxidation and soot fragmentation. Figure 46 shows the results for the ethylene/air flame ( $\Phi_{\text{overall}} = 0.87$ ). Representative soot samples at different HAB were collected using a more heavily sooting flame in the first burner (ethylene/air,  $\Phi_1 = 2.8$ ), but the overall equivalence ratio was kept constant at 0.87. PSDs (see Figures 34a and 35a) for this condition showed the presence of soot fragmentation close to the burner surface and soot burnout mainly higher in the burner.

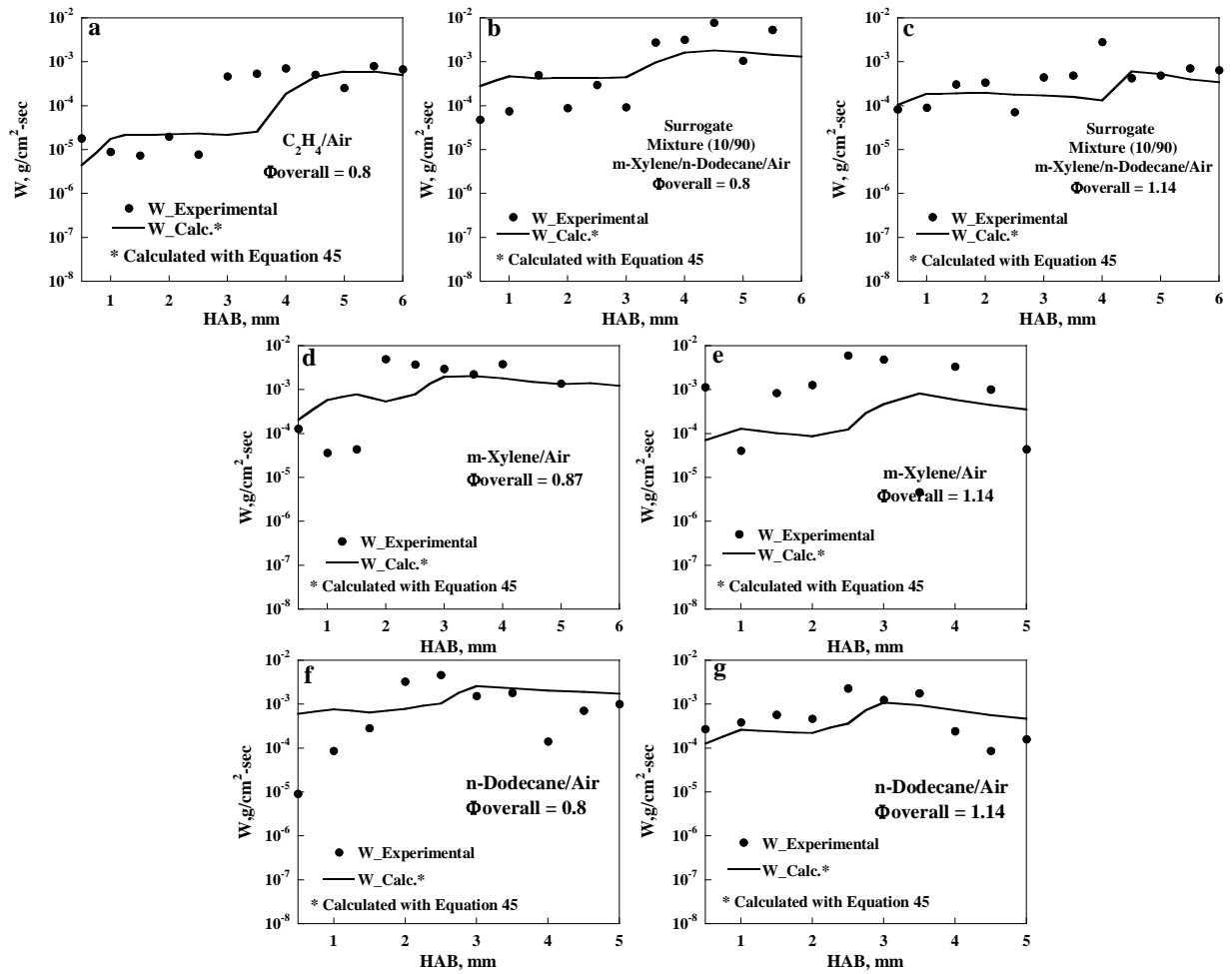


Figure 45. Predictions of soot oxidation rates using Equation 24 for: (a) ethylene/air;  $\Phi_{Overall} = 0.8$  (b) and (c) surrogate/air,  $\Phi_{Overall} = 0.8, 1.14$ ; (d) and (e) m-xylene/air,  $\Phi_{Overall} = 0.87, 1.14$  and (f) and (g) n-dodecane/air,  $\Phi_{Overall} = 0.8, 1.14$ .

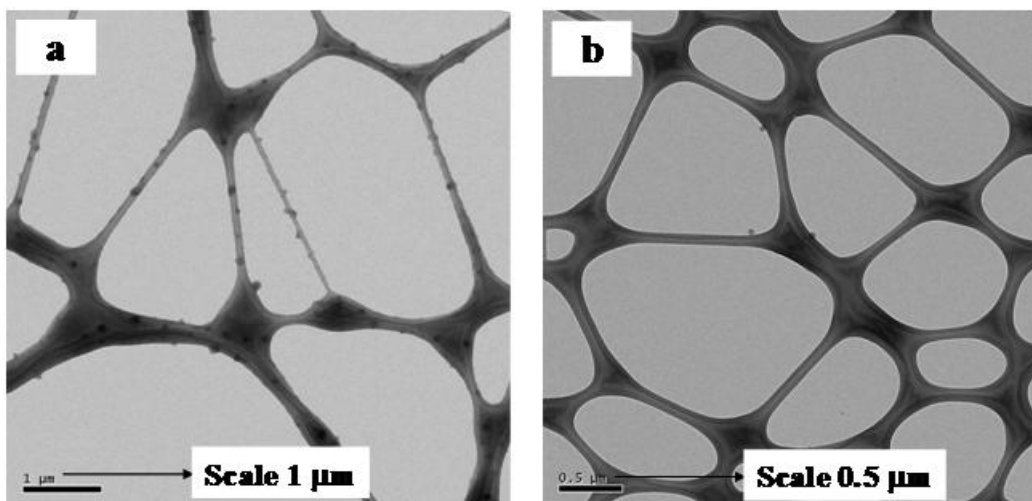


Figure 46. TEM pictures for ethylene/air flame with  $\Phi_{\text{overall}} = 0.87$ . (a) At HAB = 2 mm and (b) At HAB = 4 mm.

Figure 47 (left) presents the results for the evolution of the oxidation process as a function of the HAB (<0.5 mm, 2 and 4mm for this condition). As seen in the TEM images, close to the burner surface, most of the particles were present as agglomerates. As HAB increases a drop in the number of particles is shown as they were burned out. This behavior followed the trend of the SMPS data in terms of particle number and mass concentration decrease. TEMs of collected samples were also taken during the oxidation of soot derived from the surrogate mixture in air. TEM images (see Figure 47, right) revealed a similar behavior as compared to ethylene/air flames. Agglomerates of particles dominated close to the burner surface. As the oxidation process continued, particle diameter and number concentration dropped. These results were mainly consistent with the evolution of PSDs as a function of the HAB in terms of the burnout of particles.

HR-TEM picture were processed and analyzed using the methodology previously described (Toth et al. 2010). The nanostructural evolution from our samples collected in the two-stage burner along with other samples collected from fuel rich ethylene/air and benzene/air (Echavarria et al. 2009, 2011) with different residence times and the extents of oxidation is shown by monitoring changes in distance deviation parameter,  $\Omega$ , and junction parameter,  $\nu$ . Table 6 is a summary of the various samples and their names.

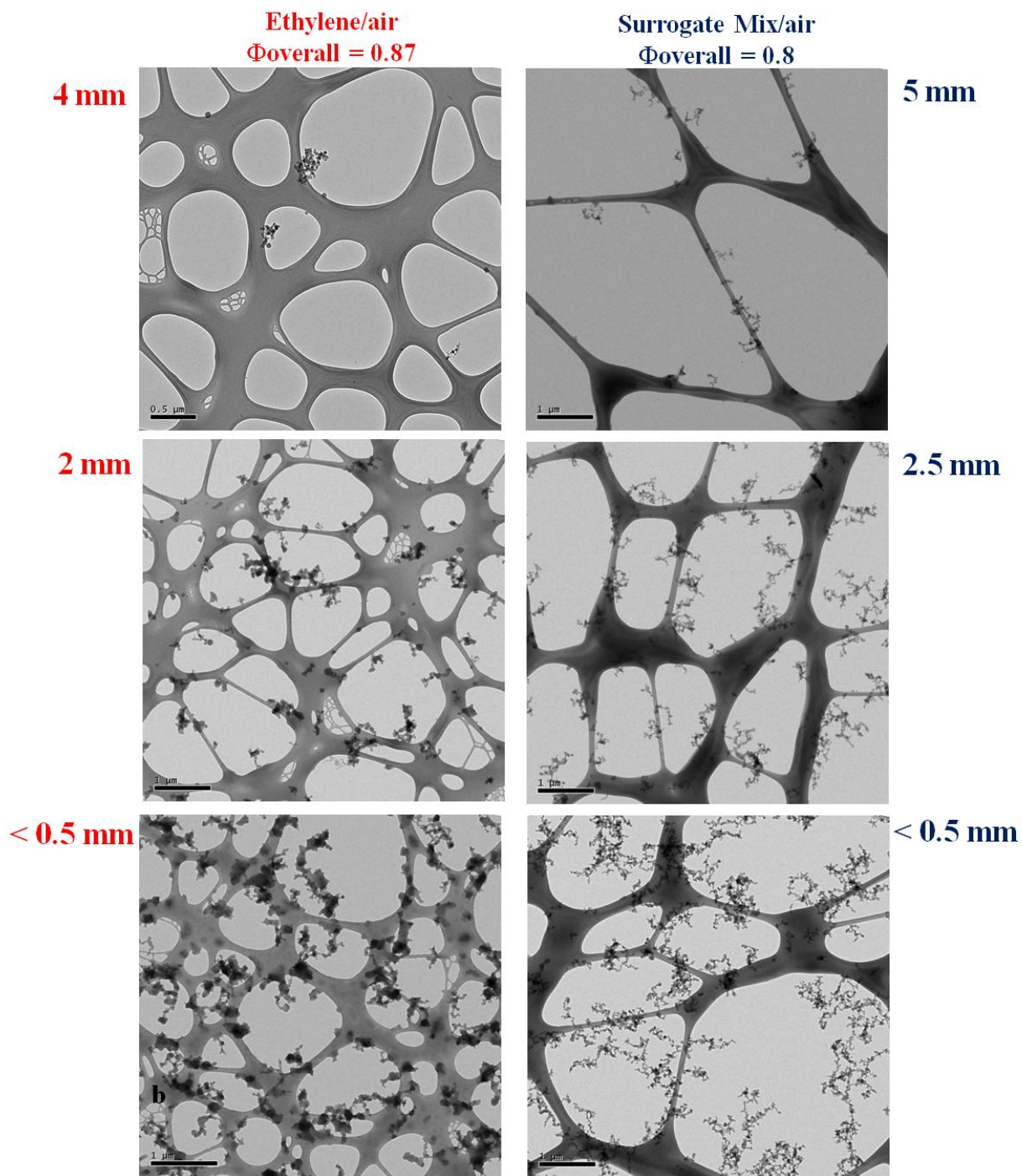


Figure 47. TEM pictures for ethylene/air (left) and surrogate (right) at HAB = 0.5 mm, 2 mm, and 4 mm. Note, the scale of the top image is different.

Table 6. Summary of samples collected

Sample name	Fuel type	Burner setup	Heights above burner, mm
Benzene flame	Benzene/air	Premixed, fuel rich	5, 10, 15
Ethylene flame 1	Ethylene/air	Two stage premixed, fuel rich/fuel lean	0.5, 2, 4
Ethylene flame 2	Ethylene/air	Premixed, fuel rich	10, 15
Surrogate flame	N-dodecane-m-xylene mixture/air	Two stage premixed, fuel rich/fuel lean	1, 3, 5

The parameters,  $\Omega$  and  $\nu$  were calculated for four fuels, each one sampled at different heights above burner (HAB). As HAB increases and the soot gets more mature, an increase in orderliness can be expected as the conventional analysis of Alfe et al. (2010) demonstrated for methane soots. A few examples of the analyzed images can be seen in Figure 48. It can be generally stated, that among the soots collected, ethylene flames produced the most unordered structures, while surrogate flames produced the most ordered structures, exhibiting high concentric symmetry at higher HABs. The HR-TEM micrographs were analyzed by both algorithms. In the case of the determination of  $\Omega$ , the Euclidean distance set of each image was extracted, and added to datasets representing each sample. These datasets were then evaluated, to determine  $\Omega$ . The average number of distances extracted from one 512 x 512 image is  $\approx 50,000$ , and several micrographs were analyzed for each sample.  $\nu$  was calculated for each micrograph and average values were produced for different samples.

First, a conventional analysis of these images was conducted for the sake of comparison, using a methodology based on the technique published by Palotas et al. (1996). The measured parameters of the fringe images were the fringe lengths, [nm] – measured as proposed by VanderWal et al. (2010), i.e. the length of the skeleton of the fringe - and interlayer distances, [nm], measured as proposed by Palotas et al. (1996). The results of this statistical analysis are presented in Figure 49. As shown in Figure 49, conventional statistical analysis produces results based on which the reliable differentiation of similar structures is difficult. The values of the interlayer distances show insignificant differences between samples and there is no apparent trend in the evolution of fringe lengths. Apart from this, the inherently high standard deviation of the results provided by this low-level image analysis algorithm makes the differentiation impossible, based on mean values alone.

The results for  $\Omega$  and  $\nu$  are presented in Figure 50. The trends of the two parameters are quite obvious as both decreased with increasing HABs for all four samples, meaning that an increasing magnitude of order could be detected in the soot structures. Interestingly enough, an even stronger correlation was found between  $\Omega$  and  $\nu$ . The highest degree of structural evolution happened in the soots from the ethylene flames, especially at low HABs. The rather small change in  $\Omega$  measured in surrogate soots can be explained by the fact that these soots were found to be fairly well ordered even at low HABs, however a huge drop in  $\nu$  indicates some extent of simplification in the texture (notice the highly developed concentric rings in Figure 48 D).

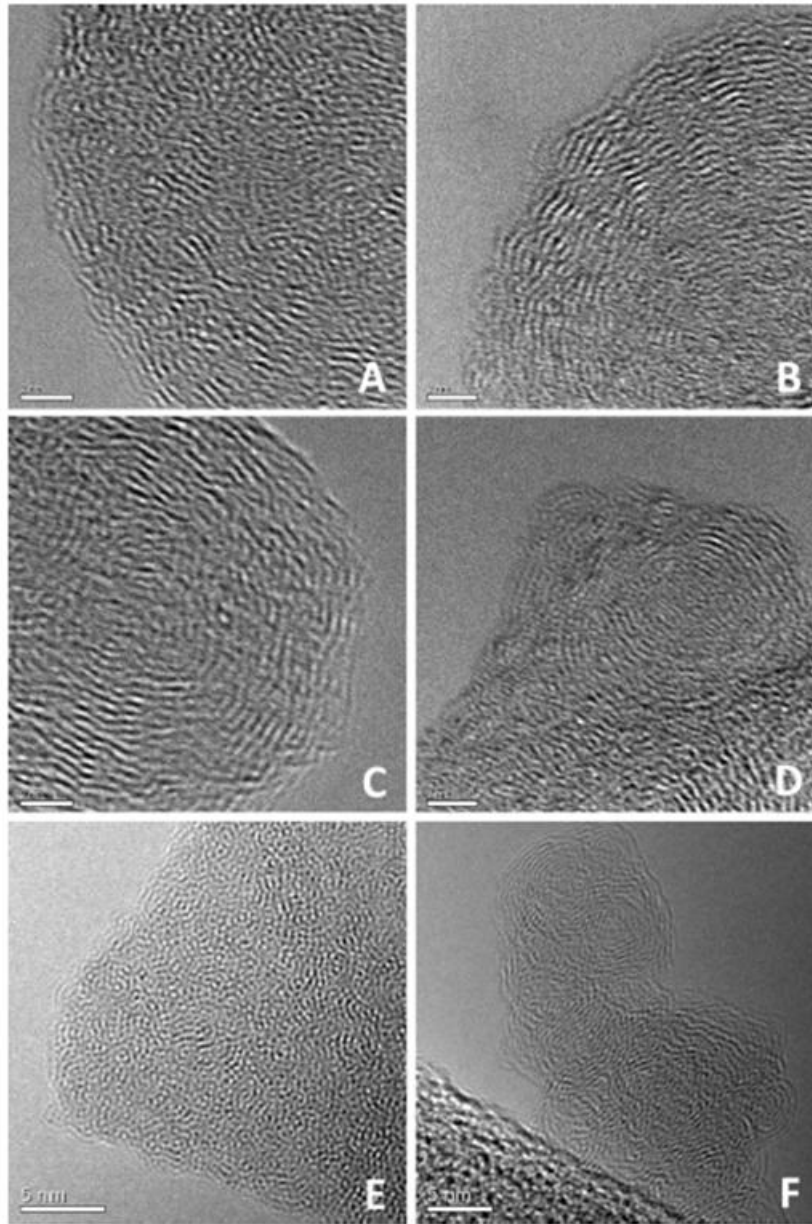


Figure 48. Some examples of the analyzed images. A, Ethylene flame 1, HAB=0.5 mm. B, Ethylene flame 1, HAB=4 mm. C, Surrogate flame, HAB=1 mm. D, Surrogate flame, HAB=5 mm. E, Benzene flame, HAB=5 mm. F, Benzene flame, HAB=15 mm.

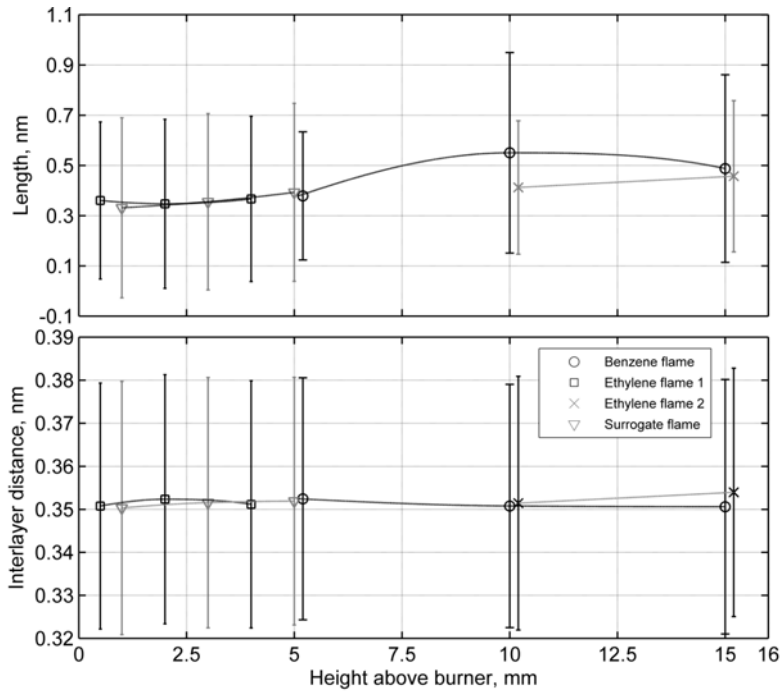


Figure 49. Results of a conventional statistical image analysis method applied to our samples. Some HAB values were shifted to improve visibility. For exact values see Table 6.

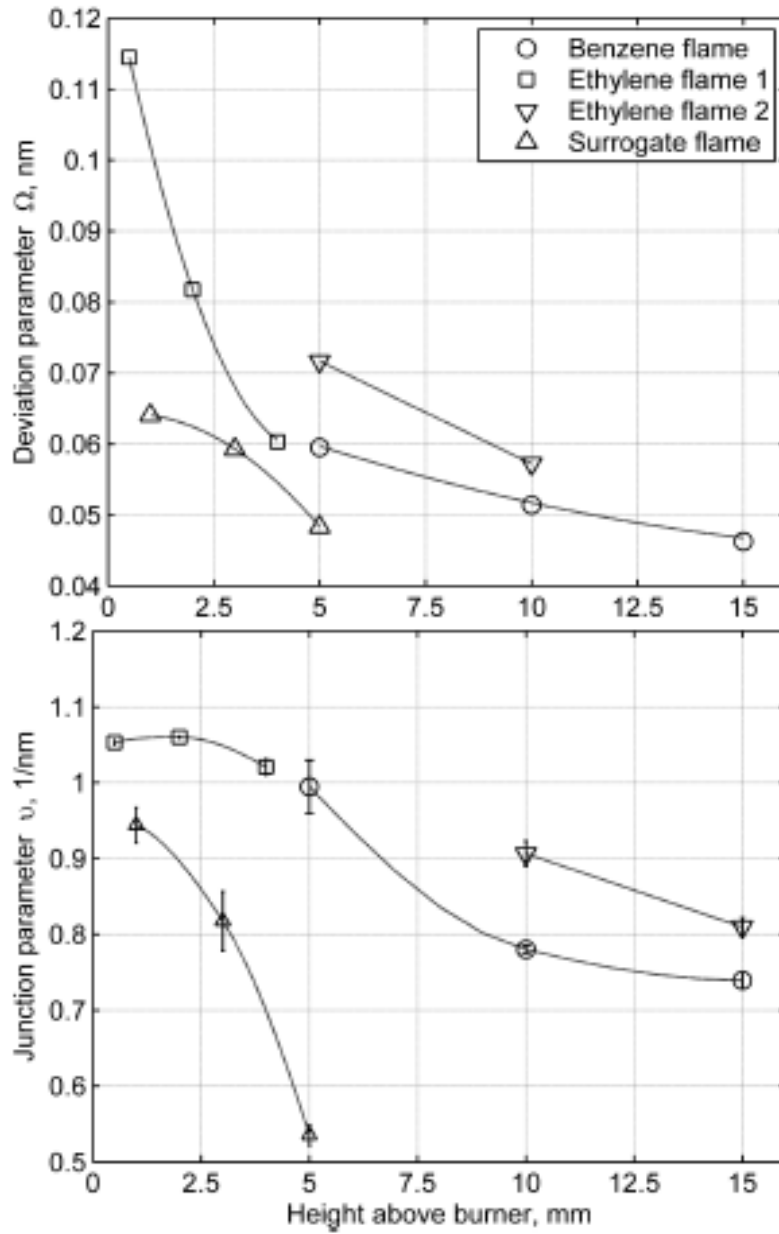
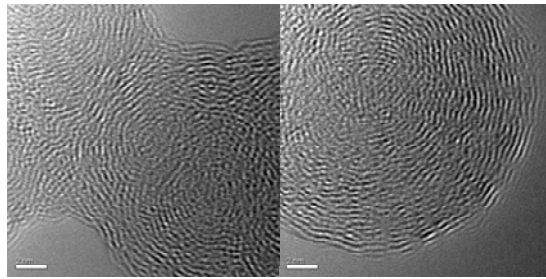
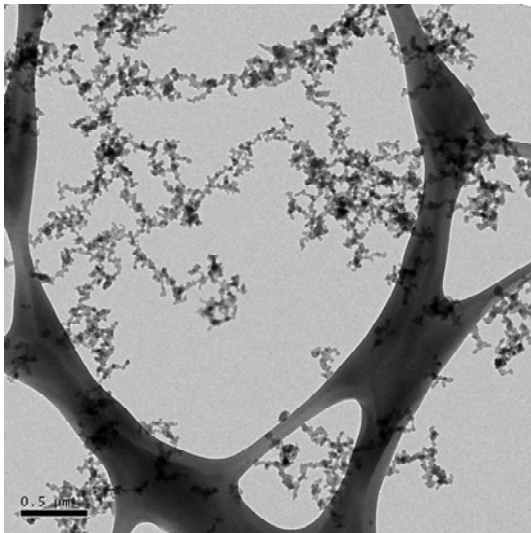
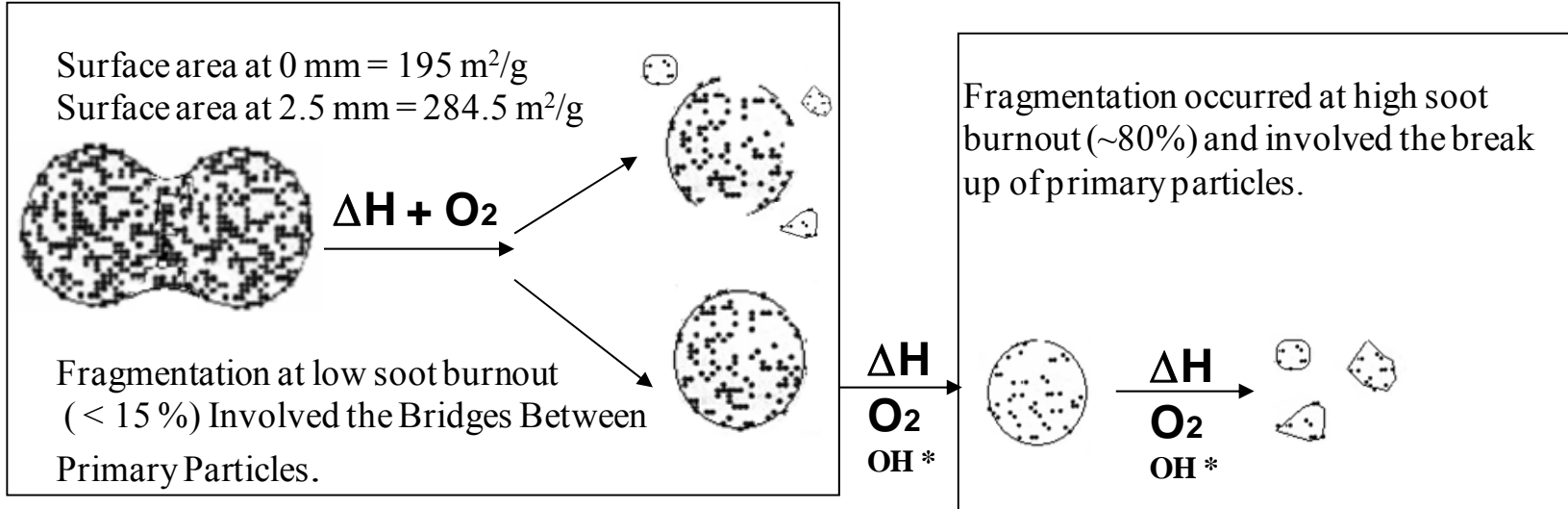


Figure 50. The measured values of  $\Omega$  and  $\nu$  for the fuel samples. Lines are guides to the eye.

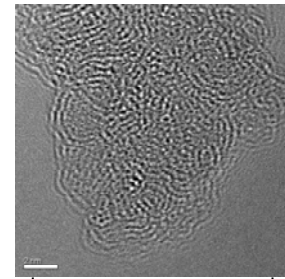
**Feasibility of Soot Fragmentation due to Internal Burning**

The process of soot oxidation, as evaluated from detailed and spatially resolved measurements of soot size distribution, flame temperature, gas-phase composition ( $O_2$  and  $OH^*$ ), and soot morphology and nanostructure has provided critical information on the kinetics of soot oxidation via  $O_2$  and  $OH^*$ . A phenomenon where particle concentration in the ultrafine ( $D_p < 10\text{nm}$ ) mode (see Figures 31 and 40) increases with HAB during oxidation has been associated to the break up or fragmentation of the particles which exist as agglomerates rather than individual particles (see Figure 47). A major difference between the results in this work and that of Neoh et al. (1981) was that the observable increase of nanoparticles in the ultrafine mode occurred mainly at low soot burnouts for this work and at high conversions for Neoh et al. At high burnout percentages, this behavior is believed to be consistent with percolation theory which predicts fragmentation with varying pore structure (Kerstein et al., 1985). For the present work, it appears as though the fragmentation involved the bridges between primary particles and occurred at low overall soot burnout ( $< 15\%$ ).

Figure 51 shows a schematic representation of the fragmentation process at low and high burnout percentages, particularly under overall lean conditions where  $O_2$  can also contribute to soot oxidation higher in the burner. According to Neoh and coworkers, fragmentation can be observed at high burnout percentages (see Figure 51, right side) when high internal surface area or high porosity has been developed in the particle surface. Neoh et al. (1981) attributed this phenomena to  $O_2$  penetrating the soot nanostructure, which, in turn, caused internal burning and loss of the connectivity between the carbonaceous phases inside the particle. This situation resulted in the fragmentation or break up of primary particles. We have attributed the fragmentation at low burnout to both the breakup of bridges (or necks) between primary particles and the removal of small fragments from the edges of the primary particles surface as illustrated in Figure 51, left side.



**Close to Burner Surface**  
 (0 – 2.5 mm)



**Higher in the burner (5mm)**

Figure 51. Hypothesis regarding the role of fragmentation during soot oxidation at low soot burnout (left) and higher soot burnout (right).

Conditions that favor this mechanism can be identified from calculations of the effectiveness factor ( $\eta$ ) for O<sub>2</sub> and OH\*. The effectiveness factor is the ratio between the actual oxidation rate and the oxidation rate assuming that the whole internal surface was exposed to the reactant and that the concentration of the oxidizer species and temperature are uniform throughout the particle, an idea of the importance of internal burning. If the effectiveness factor is close to 1, it is an indication of penetration into the soot nanostructure. In contrast, if the effectiveness factor is close to zero it is an indication of little gas penetration (Neoh, 1981).

The effectiveness factor can be expressed as (Neoh, 1981):

$$\eta = \frac{1}{\phi_s} \left( \frac{1}{\tanh 3\phi_s} - \frac{1}{3\phi_s} \right) \quad (46)$$

$$\phi_s = \text{Thiele Modulus} = \frac{R}{3} \sqrt{(k_{s,i} s_v) / D_{eff}} \quad (47)$$

The reaction constant  $k_{s,i}$  was calculated using both Equation 45, which calculated the rate of oxidation, and assuming a first order reaction rate (Neoh, 1981). Results were similar for both conditions. In this equation,  $s_v$  is the pore surface (cm<sup>2</sup>/cm<sup>3</sup>) and equivalent to the porosity divided by the pore radius. The effective diffusion coefficient,  $D_{eff}$  (cm<sup>2</sup>/s), is calculated from:

$$D_{eff} = (\gamma/\tau) \cdot (1/D_g + 1/D_k)^{-1} \quad (48)$$

where the tortuosity factor,  $\tau$ , was assumed to be 2. The Knudsen diffusion coefficient,  $D_k$  is:

$$D_k = 9700r_e \sqrt{T / Mw} \text{ cm}^2 / s \quad (49)$$

Values for the tortuosity and pore radius represented average values typically found in the literature for different types of soot and also extracted from our transmission electron microscopy images. A pore radius in the range from 5 Å to 20 Å can be taken to represent actual pores in individual particles and the spacing between individual particles in the agglomerates.

Tables 7 and 8 show the results of  $\eta$  obtained at temperature and mean particle size (averaged in the region close to the burner surface) conditions representing the region below the tube bundle and close to the top burner surface before fragmentation. The objective was to evaluate the extent of O<sub>2</sub> and/or OH\* penetration into the soot porous network which was expected to contribute to internal burning. For the ethylene/air flames with  $\Phi_{overall} = 0.8$  (Table 7),  $\eta_{O_2}$  was 1 or close to 1 relative to the smaller values obtained for  $\eta_{OH^*}$ . This was an indication that the O<sub>2</sub> molecule would be able to penetrate into the porous network to a higher extent than OH\*. Therefore, internal burning might occur mainly by the action of O<sub>2</sub>. Similar results were obtained for the surrogate mixture (see Table 8). At higher burnout percentages, the degree of penetration by OH\* becomes significant (Neoh, 1981); however, internal burning due to OH\* is not expected to have a major impact due to its higher intrinsic reactivity, and oxidation via OH\* would be expected to take place mainly in the particle surface.

Table 7. Effectiveness factor calculation for the ethylene/air system with  $\Phi_{\text{overall}} = 0.8$

Effectiveness factor(h), O <sub>2</sub>				
	373 K	600 K	1403 K	1510, K
re = 5 Å	1.00000	1.00000	1.00000	1.00000
re = 10 Å	0.99998	0.99998	0.99995	0.99991
re = 15 Å	0.99999	0.99999	0.99998	0.99996
re = 25 Å	1.00000	1.00000	0.99999	0.99998

Effectiveness factor(h), OH*				
	373 K	600 K	1403 K	1510, K
re = 5 Å	0.1056	0.1056	0.1056	0.1056
re = 10 Å	0.2032	0.2032	0.2032	0.2032
re = 15 Å	0.2927	0.2927	0.2927	0.2927
re = 20 Å	0.3743	0.3743	0.3743	0.3743

Mean Particle Diameter (0-2.5 mm) = 43 nm

Table 8. Effectiveness factor calculation for the surrogate mixture/air system with  $\Phi_{\text{overall}} = 0.8$

Effectiveness factor(h), O <sub>2</sub>				
	373 K	600 K	927K	1500K
re = 5 Å	1.000	1.000	1.000	1.000
re = 10 Å	0.999	0.998	0.998	0.997
re = 15 Å	0.999	0.999	0.999	0.999
re = 25 Å	1.000	1.000	0.999	0.999

Effectiveness factor(h), OH*				
	373 K	600 K	927K	1500K
re = 5 Å	0.038	0.038	0.038	0.038
re = 10 Å	0.076	0.076	0.076	0.076
re = 15 Å	0.112	0.112	0.112	0.112
re = 20 Å	0.1476	0.1476	0.1476	0.1476

Mean Particle Diameter (0-2.5 mm) = 120 nm

Another indication of internal burning was extracted from experimental measurements of the specific soot surface area of samples collected isokinetically using the methodology described in the materials and methods section. As mentioned previously, soot surface area was determined using CO<sub>2</sub> adsorption at 298 K in a thermogravimetric analyzer (TGA). Samples collected at the second burner surface (HAB = 0 mm) and at 2.5 mm above second burner surface showed a

small increase in soot surface area for both, soot derived from ethylene/air ( $\Phi_{\text{overall}} = 0.8$ ) and from the surrogate/air ( $\Phi_{\text{overall}} = 0.8$ ) flames. For ethylene air, soot surface area increased from  $282 \pm 35$  (0mm) to  $494 \pm 27$  (2.5 mm)  $\text{m}^2/\text{g}_{\text{soot}}$ . For the surrogate/air system, the surface area increased from  $\sim 196 \pm 18$  to  $\sim 285 \pm 31$   $\text{m}^2/\text{g}_{\text{soot}}$  in the region between 0 to 2.5 mm respectively. Even though these changes are relatively small in both flames, the increase in surface area was an indication of internal burning that would be expected to favor the removal of fragments from edges of primary particles as illustrated in Figure 51 (left side).

TEM and HR-TEM analysis provided evidence of the presence of the type of structures that might favor the mechanisms described above. For example, the presence of chain like agglomerates, bridges or necks cementing primary particles, and the spherical characteristics of the primary particles close to the second burner surface (0-2.5 mm). Higher in the burner (HAB = 5 mm), the presence of fragments without a well defined form was also observed, and their presence was associated to the breakup of primary particles. Additional HR-TEM analysis allowed establishing a correlation between the change in the diameter of the necks between primary particles and HAB. Although a more deep statistical analysis of the HR-TEM picture was difficult to perform higher in the burner because of limited sample, Figure 52 shows that the diameter of the necks decreased with increasing HAB, and it would be expected to favor the breakup of the necks cementing primary particles. This mechanism and the removal of fragments from the edges of primary particles in the region close to the burner surface seem to be an initial support for the observable increase of nanoparticles in the ultrafine mode from SMPS measurements.

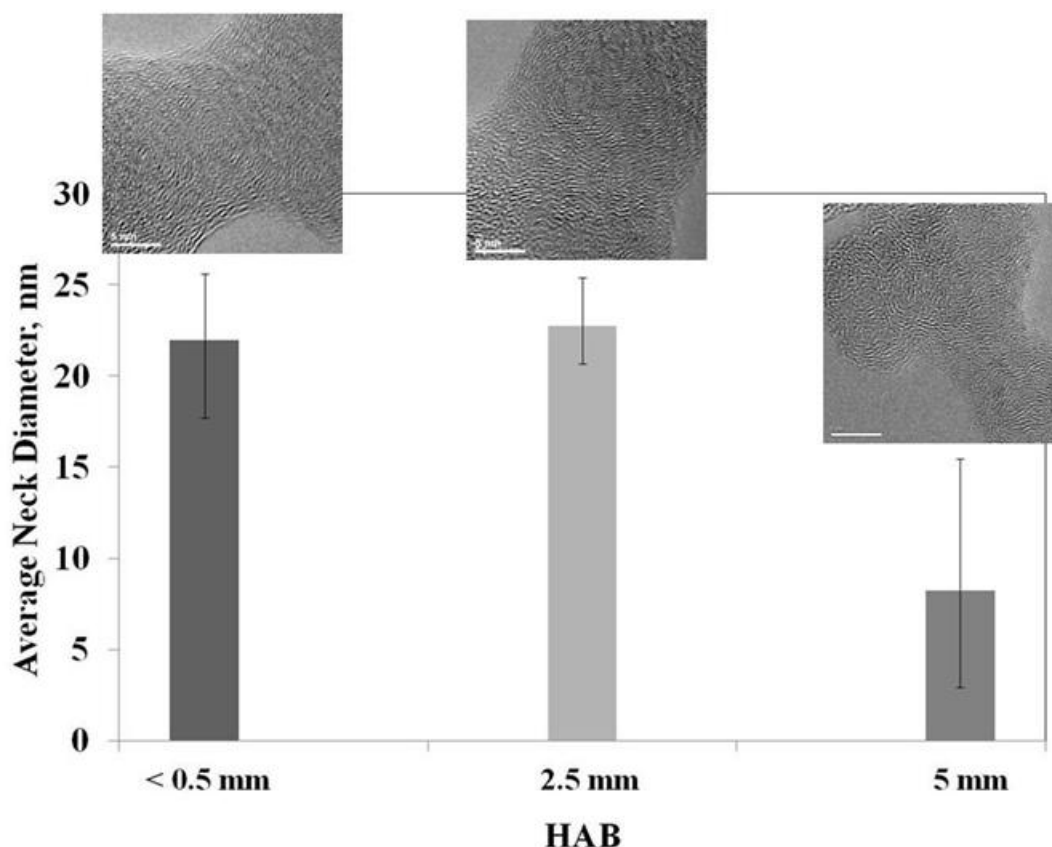


Figure 52. Change of the diameter in the necks or bridges cementing primary particles with HAB. Analysis was performed for 20 pictures for each height.

## CONCLUSIONS AND IMPLICATIONS

This project focused on the mechanisms of soot oxidation by oxygen for jet fuels used in military engines. The reactions with oxygen are particularly important for gas turbines, which operate at high excess-air rates. The examination of the role of fuel components and internal surface on soot oxidation rates was emphasized since the allowance for these effects on the oxidation rate are not currently well characterized. Examination of this additional aspect of oxidation kinetics enhanced fundamental combustion science and over the long term will enable military gas-turbine engines to continue to meet their performance and operating requirements with reduced PM emissions.

Soot oxidation was studied by following the evolution of particle size, particle number concentration, flame temperature, gas-phase composition, particle surface area, and particle nanostructure and morphology during the oxidation of soot derived from ethylene/air, surrogate/air, m-xylene/air, and n-dodecane/air premixed flames in a two-stage burner where soot formation mechanisms were isolated from the oxidation steps. Soot was burned under fuel-lean and slightly fuel-rich conditions. In ethylene/air flames, the analysis of the results in terms

of PSDs and number concentration measurements showed the possibility of break up or fragmentation of the bigger particles, as evidenced by a significant increase of particles in the ultrafine mode ( $D_p < 10\text{nm}$ ) and decrease in particle mean diameter. The extent of the fragmentation decreased with increasing the overall equivalence ratio from 0.8 to 0.94, and it did not take place for rich flames ( $\Phi_{\text{Overall}} = 1.07$  and 1.14). Analysis of the results for ethylene/air flames in terms of the evolution of major gas-phase species, particularly soot oxidizer species in flames like  $\text{O}_2$  and  $\text{OH}^*$  provided information about the contributions of  $\text{O}_2$  and  $\text{OH}^*$  on soot fragmentation and soot burnout. For lean conditions ( $\Phi_{\text{Overall}} = 0.8$  and 0.87),  $\text{O}_2$  oxidation was predominant close to burner surface, and appeared to favor the fragmentation of particles. Downstream,  $\text{OH}^*$  had a major impact, and soot oxidation rates increased. For the rich flames ( $\Phi_{\text{Overall}} 1.07$  and 1.14), soot oxidation rates were higher close to burner surface which was attributed to the faster consumption of  $\text{O}_2$  and earlier formation of  $\text{OH}^*$ .

Results during the oxidation of soot particles derived from the JP-8 surrogate mixture and its pure components (m-xylene and n-dodecane) showed a similar behavior under lean conditions ( $\Phi_{\text{Overall}} = 0.8, 0.87$ ) relative to ethylene/air flames. However the fragmentation phenomenon was also observed to occur under slightly rich conditions ( $\Phi_{\text{Overall}} = 1.14$ ), and the extent of fragmentation was as high as or even higher than the one observed under lean conditions. This behavior was correlated with the evolution of gas-phase species that showed significant changes in the evolution of soot oxidizer species after a prolonged induction period where high concentrations of  $\text{O}_2$  and a high temperature environment favored the fragmentation process.

A major difference between the results in this work and those of Neoh et al. (1981) was that the fragmentation occurred mainly at low soot burnouts for this study and at high conversions for Neoh et al. (1981). For the present work, it appears as though the fragmentation involved the bridges between primary particles and occurred at low overall soot burnout.

The fragmentation process was associated to  $\text{O}_2$  penetration into the soot porous network, which may have caused internal burning and resulted in the breakup of both the bridges (necks) between primary particles and the rupture of primary particles that might occur close to the top burner surface and/or higher elevations. The feasibility of these types of mechanisms was supported by calculations of the effectiveness factor and experimental measurements of soot surface area and morphology. The effectiveness factor calculations in ethylene/air and surrogate/air flames suggested that the  $\text{O}_2$  molecule would be able to effectively penetrate the soot nanostructure in the region close to the burner surface. Internal burning was confirmed by the increase in soot surface area in that region (0 to 2.5 mm). TEM and HR-TEM analysis revealed the morphological and nanostructural characteristics of soot particles that can support the breakup of the bridges cementing primary particles and the removal of fragments from the particles edges due to internal burning.

TEM and HR-TEM micrographs also showed insights into the changes in soot morphology and nanostructure that occur during soot oxidation and fragmentation. TEM pictures supported the burnout of particles, while analysis of HR-TEM pictures showed difference of soot derived from ethylene/air and the surrogate/air flames. A sensitive image analysis technique has been developed for the representative quantification of soot nanostructure orderliness utilizing image processing techniques. The technique is robust, since the evaluated number of elements in the

measured datasets is large, and produces consistently reproducible parameters with a resolution high enough to show differences in soot structure. The method has been applied to soot samples of various fuels, collected from different burner setups at different HAB in order to monitor their nanostructural evolution. In all cases, decreasing tendencies were found in the values of the distance deviation and junction parameters as the HAB increased suggesting increasing orderliness in soot structure with its age. Based on the observation of  $\Omega$ , the highest degree of structural evolution happened in the soots from the ethylene flames, especially at low HABs. The rather small change in  $\Omega$  measured in surrogate soots can be explained by the fact that these soots were found to be fairly well ordered even at low HABs. However, a huge drop in  $\nu$  indicates some extent of simplification in the texture as reflected in the highly developed concentric rings in soot derived from the surrogate flame.

The experimental data were compared to typical models used in the literature and they produced a good agreement with the experimental results. A kinetic expression that accounted for changes in the temperature, and  $O_2$  and  $OH^*$  concentration during the oxidation of soot produced from different sources was proposed. The proposed equation was able to reproduce the major features of the experimental results and cover wide range of conditions typical of practical combustion systems. In addition the activation energy and oxygen partial pressure order agreed within the range presented in the literature. The pre-exponential was different, but this is likely a result of changes in the surface area. Even though the nanostructure changed with HAB for the ethylene and surrogate, it was not apparent that this change in nanostructure affected the rate of oxidation or that our data accounted for such changes.

The design of the experimental and modeling methodologies on soot oxidation in premixed flames allowed for identifying the conditions where soot fragmentation and soot burnout can be favored. New insights into the process of soot fragmentation were recognized by showing that fragmentation, depending upon the experimental conditions, can occur at lower soot burnout percentages and under fuel-rich conditions. These results are expected to contribute to the current knowledge on the oxidation of soot particles. This study also opens new paths to evaluate different strategies to reduce the emissions of soot into the atmosphere.

## LITERATURE CITED

- Abid, A.D., Heinz, N., Tolmachoff, E.D., Phares, D.J., Campbell, C.S., Wang, H. *Combustion and Flame* 154 (2008) 775-788.
- Abid, A.D., Tolmachoff, E.D., Phares, D.J., Wang, H., Liu, Y., Laskin, A. *Proceedings of the Combustion Institute* 32 (2009) 681-688.
- Alfe, M., Apicella, B., Rouzaud, J.N., Tregrossi, A., Ciajolo, A. *Combustion and Flame* (2010).
- Aso, H., Matsuoka, K., Sharma, A., Tomita, A. *Carbon* 42 (2004) 2963– 2973.
- Blevins L.G. Particulate Matter Emitted from Aircraft Engines, *Proc. AIAA/ICAS International Air and Space Symposium and Exposition: the Next 100 Years*, Dayton, OH, July 14-17, 2003.
- Bradley, D. G. Dixon-Lewis, S. E. Habik, E. M. J. Mushi. *Proceedings of the Combustion Institute* 20 (1984) 931-940.
- Campbell, P.A. Investigation of the Roles of Surface Oxide Complexes and their Distributions in the Carbon-Oxygen Heterogeneous Reaction Mechanism, PhD thesis, Stanford University, 2005.
- Champange, D.L. (1971) Standard Measurement of Aircraft Gas Turbine Engine Exhaust Smoke. New York, Society of Automotive Engineers.
- Chen, D.R., Pui, D. Y. H. D. Hummes, H., Fissan, F. R., Quant, G. J. Sem, *Journal of Aerosol Science* 29 (1998) 497.
- Cooke, J.A., M. Bellucci, M.D. Smooke, A. Gomez, A. Violi, T. Faravelli, E. Ranzi, *Proceedings of the Combustion Institute* 30 (2005) 439-446.
- D'Anna, A., Kent, J.H. *Combustion and Flame* 144 (2006) 249-260.
- D'Anna, A. *Energy & Fuels* 22 (2008) 1610-1619.
- D'Anna, A., D'Alessio, A. *Environmental Science & Technology* 42 (2008) 859-863.
- D'Anna, A. *Proceedings of the Combustion Institute* 32 (2009) 593-613.
- Dai, Z., A.M. El-Leathy, C.H. Kim, S.S. Krishnan, K-C. Lin, F. Xu, G.M. Faeth, Fourth International Microgravity Combustion Workshop, NASA Conference Publication 10194, (1997) 199-204.
- Dobbins, R.A., Megaridis, C.M. *Langmuir* 3 (1987) 254-259.
- Dockery, D. W. et al. *New England Journal of Medicine* 329 (1993) 1753-1758.
- Du, Z., A.F. Sarofim, J.P. Longwell, *Energy & Fuels*, 4(3) (1990) 296-302.
- Du, Z. Kinetic modeling of carbon oxidation. PhD thesis, MIT, 1990.
- Echavarria, C.A., Sarofim, A.F., Lighty, J.S., D'Anna, A. *Proceedings of the Combustion Institute* 32 (2009) 705-711.
- Echavarria C. A., Jaramillo I.C., Sarofim A. F., Lighty J. S. *Proceedings of the Combustion Institute* 33 (2011) 659-666.
- EPA (Environmental Protection Agency) (1991) *Nonroad Engine and Vehicle Emission Study Report*, EPA 460/3-91-02, EPA Office of Air and Radiation.
- EPA (Environmental Protection Agency) (1997) *Regulatory Support Document, Control of Air Pollution from Aircraft and Aircraft Engines*, EPA Office of Air and Radiation.

- EPA (Environmental Protection Agency) (2006) *2002 National Emission Inventory*. EPA Office of Air and Radiation. <http://www.epa.gov/ttn/chief/net/2002inventory.html>
- Edwards, T., *Jet Fuel Surrogate Research: A White Paper*, Defense Energy Support Center, “Petroleum Quality Information System” (PQIS), <http://www.desc.dla.mil/DCM/DCMPage.asp?pageid=99>), December 23, 2005.
- El-Leathy, A.M, F. Xu, G.M. Faeth. *AIAA Aerospace Sciences Meeting and Exhibit*, 40th, Reno, NV, Jan. 14-17 (2002).
- El-Leathy A.M., C. H. Kim, G.M. Faeth, F.Xu. *AIAA Journal* 42, 5 (2004) 988-996.
- Faeth, G., C. Kim, A. El-Leathy. *41st Aerospace Sciences Meeting and Exhibit*, Reno, Nevada, Jan. 6-9, 2003.
- Fenimore C. P, G.W. Jones, *J. Physical Chem* 71 (1967) 593-597.
- Garo, A., G. Prado, J. Lahaye, *Combustion and Flame*. 79, (1990) 226-233.
- Gatos, B., Pratikakis, I., Perantonis, S. *Pattern Recognition* 39 (2006) 317– 327.
- Hagen D. P. Whitefield, J. Paladino, M. Trueblood, H. Lilienfeld *Geophy. Res. Lett.* 25, 10 (1998) 1681-1684.
- Haynes, B. S, T.G. Newbury, *Proceedings of the Combustion Institute* 28 (2000) 2197-2204.
- Higgins, K. J., K. Jung, D. B. Kittelson, J. T. Roberts, M.R. Zachariah, *J. Physical Chem.* 106 (2002), 96-103.
- Hinds, W.C. in: *Aerosol technology: properties, behavior, and measurement of airborne particles*, J. Wiley, New York, 1982.
- Hurt R. H., B.S. Haynes, *Proceedings of the Combustion Institute* 30 (2005) 2161-2168.
- Kandas, A.W. *Structural evolution of carbon during oxidation*, PhD Thesis in Chemical Engineering, MIT, Cambridge MA (1997).
- Kasper, M., Siegmann, K., Sattler, K. *Journal of Aerosol Science* 28 (1997) 1569- 1578.
- Kerstein, A.R., Niksa, S. *Proceedings of the Combustion Institute*, 20 (1985) 941- 949.
- Kim, C.H., A.M. El-Leathy, F. Xu, G.M. Faeth, *Combustion and Flame*. 136, 1-2 (2004) 191-207.
- Lanzuolo; P. Minutolo, *Proceedings of the Combustion Institute* 32 (2009) 689- 696.
- Lee, K. B., M. W. Thring, et al. *Combustion and Flame* 6 (1962) 137-145.
- Leung K.M., R.P. Lindsedt, W.P. Jones WP. *Combustion and Flame* 87 (1991) 289-305.
- Lighty, J.S., A.F. Sarofim, J.M. Veranth, *J Air & Waste Mgt. Assoc.* 50 (2000) 1565-1618.
- Lighty. J.S., Romano, V., Sarofim, A.F in: *Proceedings of the International Workshop on Combustion Generated Fine Carbon Particles*, Anacapri, Italy, 2008; H. Bockhorn; A. D'Anna; H. Wang; A. Sarofim, (Eds.) Anacapri, Italy, (2008).
- Luther, F.M., J.S. Change, W.H. Diewere, J.E. Penner, R.L. Tarp, D.J. Wuebbles, *Potential Environmental Effects of Aircraft Emissions*, Lawrence Livermore National Laboratory, UCRL-52861, Livermore, CA. 1979.
- Manzello, S.L., Lenhart, D.B., Yozgatligil, A., Donovan, M.T., Mulholland, G.W., Zachariah, M.R., Tsang, W. *Proceedings of the Combustion Institute* 31 (2007) 675-683.
- Maricq, M.M., Podsiadlik, D.H., Chase, R.E. *Aerosol Science and Technology* 33 (2000) 239-260.

- Maricq, M.M., Chase, R.E., Xu, N. Abstracts of Papers of the American Chemical Society 222 (2001) U478-U478.
- Maricq, M.M., Ning, X. *Journal of Aerosol Science* 35 (2004) 1251-1274.
- Maricq, M.M. *Combustion and Flame* 141 (2005) 406-416.
- McEnally, C.S., Koylu, U.O., Pfefferle, L.D., Rosner, D.E. *Combustion and Flame* 109 (1997) 701-720.
- Merrill, C. J., *The oxidation and fragmentation of soot in a two-stage burner system*, University of Utah, Salt Lake City, UT, 2005.
- Minutolo, P., D'Anna, A., D'Alessio, A. *Combustion and Flame* 152 (2008) 287- 292.
- Nagle, J., R.F. Strickland-Constable. *Proceedings of the Fifth Carbon Conference*; Pergamon Press: Oxford, 1 (1962) 154-164.
- Neeft J.P.A, T.X. Nijhuis., E. Smakman, M. Makkee, *Fuel* (1997) 76(12) 1129-1136.
- Neoh, K.G., *Soot burnout in Flames*, MIT, Cambridge, MA, 1981.
- Neoh, K.G., J.B. Howard, A.F. Sarofim, in: D. C. Siegla, G. W. Smith (Eds.), *Soot oxidation in flames*. Plenum Press: New York, 1981; pp 261-277.
- Neoh, K.G., Howard, J.B., Sarofim, A.F. in: *Particulate Carbon: Formation during Combustion*, G. W. S. D. C. Siegla, (Ed.) Plenum: New York, 1981; pp 261-277.
- Neoh, K.G., Howard, J.B., Sarofim, A.F. *Proceedings of the Combustion Institute* 20 (1985) 951-957.
- Netti, P., D'Anna, A. *Environmental Science & Technology* 43 (2009) 2608-2613.
- Nienow, A. M., J. T Roberts, and M. R. Zachariah, *J. Phys Chem. B*, 109 (2005), 5561-5568.
- O'mara, W.C. *Handbook of Semiconductor Silicon Technology*, William Andrew Publishing, 1990.
- Page, F. Ates. *Advances in Chemistry Series* 166 (1978) 190-197.
- Palotas, A.B., L.C. Rainey, C.J. Felderman, A.F. Sarofim, J.B. Vander Sande, 33 (1996) 266-278.
- Park, C., J. P. Appleton., *Combustion and Flame* 20 (1973), 369-379.
- Penner J.E., D.H. Lister, D.J. Griggs, D.J. Dokken, M. McFarland, *Aviation and the Global Atmosphere: A Special Report of the Intergovernmental Panel on Climate Change (IPCC) Working Groups I and II*, Cambridge University Press, Cambridge, UK (1999).
- Peters, A., D. W. Dockery, et al. *Circulation* 103 (2001) 2810-2815.
- Petzold A., F. Schröder *Aerosol Sci. Technol.* 8 (1998) 62-76.
- Petzold, A., A. Doppelheuer, C.A. Brock, F. Schröder *J. Geophys. Res.- Atmos.*, 104, D18 (1999) 22171-22181.
- Pueschel R.F., S. Verma, G.V. Ferry, *Geophys. Res. Lett.* 25, 10 (1998) 1685-1688.
- Puri, R, R.J. Santoro, K.C. Smyth. *Combustion and Flame*, 97, 2, (1994) 125-144.
- Radian (1988) *1997 Air Emission Inventory Report*, Tyndall Air Force Base, Florida.
- Rogers F., P. Arnott, B. Zielinska, J. Sagebiel, K. Kelly, D. Wagner, J.S. Lighty, A.F. Sarofim *J. Air & Waste Manage. Assoc.* 55 (2005) 583-593.
- Roth, P. O., Brandt, S. Vongersum. *Proceedings of the Combustion Institute* 23 (1990) 1485-1491.
- Sauvola, J., Pietikainen, M. *Pattern Recognition* 33 (2000) 225-236.

- Sharma, A., Kyotani, T., Tomita, A., *Fuel* 78 (1999) 1203–1212.
- Sgro, L.A. et al. *Environmental Science & Technology* 42 (3) (2008) 859-863.
- Sgro, L.A., et al. *Proceedings of the Combustion Institute* 32 (2009) 689-696.
- Shaddix, C.R. in: Correcting thermocouple measurements for radiation loss: A critical review, *Proceedings of 33rd National Heat and Mass Transfer Conference*, Albuquerque, New Mexico, 1999.
- Shim, H-S, Hurt, R. H., *Energy & Fuels*, 14 (2000) 340-348.
- Shim, H.S., Hurta, R.H., Yang, N.Y. *Carbon* 38 (2000) 29–45.
- Smith I.W. *Fuel* 57 (1978) 409.
- Stanmore B, J-F Brillhac, P. Gilot (1999) SAE paper 1999-01-0115.
- Tolbert P.E., M. Klein, K.B. Metzger, J. Peel, W.D. Flanders, K. Todd, J.A. Mulholland, P.B. Ryan, H. Frumkin *J. Exposure Analy. and Env. Epid.* 10 (2000) 446-460.
- Toth, P., A. B. Palotas, J. Lighty, C. A. Echavarria, *Fuel*, submitted, 2010.
- TSI, Inc: Technical report, TSI Incorporated. (2006).
- Vander Wal, R.L., Bryg, V.M., Hays, M.D. *Aerosol Science* 41 (2010) 108–117.
- Vierbaum, R., P. Roth, *Proceedings of the Combustion Institute* 29 (2003) 2423-2429.
- Xu, F.A. M. El-Leathy, C. H. Kim, G. M. Faeth. *Combustion and Flame*, 132 (2003) 43-57.
- Yang, J., S. Cheng, X. Wang, Z. Zhang, X. Liu, G. Tang, *Trans. Nonferrous Met. Soc. China* 16 (2006) 796–803.
- Zhang, T.Y, Suen, C.Y. *Image Processing and Computer Vision* 27 (1984) 236–239.
- Zhang, H. *Numerical Combustion of Commercial Fuels and Soot Formation. PhD Thesis, University of Utah*, May, 2005.
- Zhao, B., Yang, Z.W., Johnston, M.V., Wang, H., Wexler, A.S., Balthasar, M., Kraft, M. *Combustion and Flame* 133 (2003) 173-188.
- Zhao, B., Yang, Z.W., Wang, J.J., Johnston, M.V., Wang, H. *Aerosol Science and Technology* 37 (2003) 611-620.

## LIST OF PUBLICATIONS AND PRESENTATIONS

### Peer-Reviewed Publications and Proceedings

1. P. Toth, A. B. Palotas, **J. Lighty**, C. A. Echavarria, “Quantitative differentiation of poorly ordered soot nanostructures: a semi-empirical approach,” *Fuel*, submitted, 2010.
2. C. A. Echavarria, I. C. Jaramillo, A F. Sarofim, **J. S. Lighty**, “Studies of Soot Oxidation and Fragmentation in a Two-Stage Burner under Fuel-Lean and Fuel-Rich Conditions,” *Proceedings of the Combustion Institute* 33 (2011), pp. 659-666, <http://dx.doi.org/10.1016/j.proci.2010.06.149>.
3. C. A. Echavarria, I. C. Jaramillo, A F. Sarofim, **J. S. Lighty**, “Burnout of Soot Particles Derived from JP-8 Surrogate Flames in a Two-Stage Burner, *Combustion and Flame*, In Preparation, 2011.

4. C. A. Echavarria, I. C. Jaramillo, J. Levinthal, A. F. Sarofim, **J. S. Lighty**, “Kinetic Studies of the Oxidation of Soot via O<sub>2</sub> in a Two-Stage Burner and a High-Pressure TGA, *Proceedings of the Combustion Institute*, In Preparation, 2012.

### **Book Chapters and Document Contributions**

1. **J. S. Lighty**, V. Romano, A. F. Sarofim, “Soot Oxidation,,” in *Combustion Generated Fine Carbonaceous Particles*, editors: H. Bockhorn, A. D’Anna, A. F. Sarofim, H Wang, KIT Scientific Publishing (2009). Invited poster, Ana Capri, Italy, 2007.

### **Conference Presentations, Papers and Proceedings**

1. C. A. Echavarria, C. Jaramillo, A. F. Sarofim, and **J. S. Lighty**, “Oxidation and Fragmentation of Soot Particles Derived from JP-8 Surrogate Flames in a Two-Stage Burner”, presentation at the 7<sup>th</sup> US National Meeting to be held March 20-23, 2011, Atlanta GA.
2. C. A. Echavarria, C. Jaramillo, A. F. Sarofim, and **J. S. Lighty**, “Burnout of Soot Particles Derived From a JP-8 Surrogate in a Two- Stage Premixed Burner,” presented at 2010 AIChE Annual Meeting, Salt Lake City, UT, November (2010).
3. C. A. Echavarria, I. C. Jaramillo, A. F. Sarofim, **J. S. Lighty**, “Studies of Soot Oxidation and Fragmentation in a Two-Stage Burner under Fuel-Lean and Fuel-Rich Conditions,” Presented at the 31<sup>st</sup> Symposium (International) on Combustion and accepted in the *Proceedings of the Combustion Institute*, Beijing, China (2010).
4. C. A. Echavarria, B. Brewster, **J. S. Lighty**, A. Sarofim, “Studies of Soot Oxidation in a Two-Stage Premixed Burner; Effects of temperature and fuel composition on the evolution of PSD,” presented at 2009 AIChE Annual Meeting, Nashville, TN, November (2009).
5. C. A. Echavarria , **J. S. Lighty**, A. Sarofim, “Studies of soot oxidation in a two stage burner under fuel lean conditions,” presented at the Western States Section of the Combustion Institute Meeting, Irvine CA, October 2009.
6. V. Romano, A. F. Sarofim, **J. S. Lighty**, “Soot fragmentation in laminar pre-mixed ethylene-air flames,” presented at the 2007 Fall Technical Meeting, Western States Section/Combustion Institute, Livermore, CA October 16-17 (2007).

